2

Analysis and control of small isolated molecular systems

Albrecht Lindinger[1], Vlasta Bonačić-Koutecký[2], Roland Mitrić[2],
David Tannor[3], Christiane P. Koch[4], Volker Engel[5],
Thorsten M. Bernhardt[6], Joshua Jortner[7], Aldo Mirabal[1], and
Ludger Wöste[1]

[1] Institut für Experimentalphysik, Freie Universität Berlin, Germany
[2] Institut für Chemie, Humboldt-Universität zu Berlin, Germany
[3] Department of Chemical Physics, Weizmann Institute of Science, Israel
[4] Institut für Theoretische Physik, Freie Universität Berlin, Germany
[5] Institut für Physikalische Chemie, Universität Würzburg, Germany
[6] Institut für Oberflächenchemie und Katalyse, Universität Ulm, Germany
[7] School of Chemistry, Tel Aviv University, Israel

Coordinated by: Albrecht Lindinger

2.1 Motivation and outline

Elementary dynamical processes in molecules like bond shaking, breaking or making commonly occur on the femtosecond time scale. With the advent of ultrafast laser sources, such as Ti:sapphire, adequately short light pulses of just a few optical cycles can be delivered. This allows the direct, time-resolved observation of dynamical molecular processes, as convincingly shown by Zewail et al. [1–5].

A powerful tool in this regard is pump-probe spectroscopy. It employs a first ultrafast laser pulse to excite the molecular system to a transient intermediate state (pump). This broadband excitation creates a coherent superposition of vibrational eigenstates; the resulting nonequilibrium configuration causes the propagation of a vibrational wave packet on the potential energy surface of the corresponding electronic state. The evolution of the induced wave packet motion is subsequently interrogated with a second, time-delayed ultrashort laser pulse (probe), which induces easily observable processes, such as fluorescence, photoelectron emission or multiphoton ionization. Oscillatory features in the observed signal reflect vibrating wave packet motions, which correspond to the vibrational structure of the photoexcited system. Nonoscillatory signal structures may arise from radiative and nonradiative decay channels; or they reflect photoinduced chemical reactions like dissociations, fragmentation cascades or the formation of new bonds. Such reaction processes can be distinguished by observing the individual signal channels of all involved molecules. This is achieved by employing photoionizing pump-probe schemes, which permit the interrogated particles being monitored size-selectively by means of mass spectrometry.

Time-dependent dynamics calculations allow to simulate the observed dynamical behavior. When performed on sufficiently small and isolated molecules, this interplay of theory and experiment yields the pathways and transition mechanisms of the photon-induced processes enabling their detailed analysis [6, 7]. For larger molecules the task becomes significantly more difficult; this is due to the rapidly growing amount of internal vibrational degrees of freedom that can couple with each other, leading to internal vibrational energy redistribution (IVR). Dephasing and loss of coherence occurs and finally the system is thermalized. If the system is embedded in a liquid or a solid, or if it is deposited on a surface, the thermalization process commonly occurs still much faster. In order to avoid this complication while entering into the subject, the book follows this growing degree of complexity and focuses in the beginning of Chap. 2 on the ultrafast reaction dynamics of small isolated molecular systems. The following chapter will treat larger molecules; then later systems coupled to a condensed environment will be treated.

Pump-probe analysis leads conveniently across an electronically excited transition state, which is easily prepared by a pump pulse. The approach is described in detail in the next Sect. 2.2. However, for understanding the dynamical behavior of the entire system, the comprehension of its electronic ground state, especially when vibrationally excited, is crucial. Such systems can be prepared by using the pump pulse for vertical photodetachment of a stable negative ion (Ne), which commonly leads it to the vibrationally hot electronic ground state of its corresponding neutral (Ne). The resulting wave packet dynamics is then probed by a time-delayed probe pulse, which reionizes the system to a positive ion (Po). As described in Sect. 2.3, this charge reversal pump-probe spectroscopy (NeNePo) allows, when combined with time-dependent quantum calculations, to understand the occurring isomerization dynamics and reactivity of the system, and the onset of IVR-processes, which progressively gain importance at growing particle sizes [8, 9]. Small clusters are well suited systems to probe the evolution of dynamical processes in a range, where each atom counts.

The successful analysis of a dynamical system raises hope, that also control of the photoinduced processes can be achieved on a real time basis. Long before an experimental realization far-reaching theoretical concepts [10–21] were developed that use tailor-made pulse sequences or coherent superpositions of states to influence the dynamical pathway of a molecular system. The main goal of these control schemes is to guide the system into a distinct reaction channel. So, guided by theory new techniques were developed to shape the employed femtosecond laser pulses such, that successful control experiments could be performed. Experimentally this requires the synthesis of optimally composed pulse shapes; they can be found by using adaptive feedback loops, as suggested by Judson and Rabitz [22]. Theoretically this is accomplished by employing optimal control theory [11, 16, 20, 21, 23, 24]. As presented in Sect. 2.4, a much deeper insight into the reaction and relaxation dynamics of ultrafast photoinduced processes can be gained from this beautiful convergence between theory and experiment.

Photoassociation experiments of ultra-cold atoms in magneto optical traps (MOT) and in Bose-Einstein condensates (BEC) have raised the question, whether the formed molecules, which are vibrationally still extremely hot, can internally be cooled down. Here again, coherent control scenarios offer exciting perspectives to prepare ultracold molecules and to gain insight into their chemistry. Section 2.5 presents new concepts, which employ shaped ultrafast laser pulses to optimize photoassociation yields followed by radiative cooling cycles to pump the photo-associated molecules in their ultracold environment down to the lowest vibrational state.

2.2 Probing the dynamics of electronically excited states

V. Bonačić-Koutecký, R. Mitrić, A. Lindinger, L. Wöste

The principle of a pump-probe observation scheme via an electronically excited state is presented in Fig. 2.1. The originally rather cold molecules are excited from a low vibrational level of the electronic ground state. Due to the spectral width of the employed fs-pump pulse, a coherent superposition of several vibrational states is then created in the electronically excited state, which leads to the formation of a vibrational wave packet. If a bound electronic state is excited (Fig. 2.1a), this wave packet will oscillate between the inner and outer turning point of the potential energy curve (or surface), reflecting the vibrational motion of the excited molecule. The temporal evolution of this wave packet can be monitored by the probe pulse, which - at a variable delay - excites the particle into a size-selectively detectable ion state. Ionization can either be achieved directly by one photon or it is accomplished by a multiphotonic sequence, which preferably leads across higher excited electronic states. Since the efficiency of the ionization step depends critically upon the position of the wave packet along the reaction coordinate, the obtained ionization efficiency (time dependent Franck-Condon factor) changes significantly as a function of the delay between excitation (pump) and ionization (probe). By tuning this delay time, the temporal evolution of the oscillating wave packet appears as an intensity modulation on the corresponding ion channel, as shown later, for example, in Fig. 2.3.

If, however, a bound-free transition into a dissociative electronic state is excited (see Fig. 2.1b), no oscillatory behavior occurs, but the ion signal will

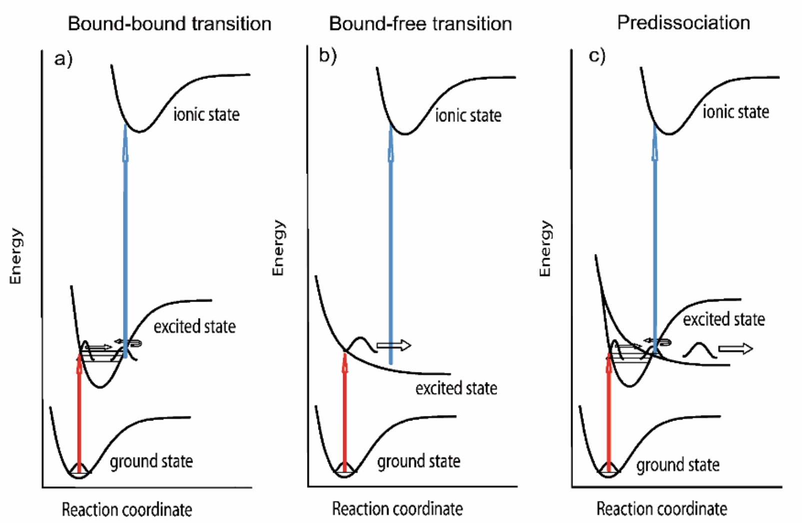

Fig. 2.1. The principle of pump-probe spectroscopy by means of transient two-photon ionization: A first fs-laser pulse electronically excites the particle into an ensemble of vibrational states creating a wave packet. Its temporal evolution is probed by a second probe pulse, which ionizes the excited particle as a function of the time-dependent Franck-Condon window; a) shows the principle for a bound-bound transition, where the oscillatory behavior of the wave packet will appear; b) shows a bound-free transition exhibiting the decay of the fragmenting particle, and c) shows the process across a predissociated state, where the oscillating particle progressively leads into a fragmentation channel.

show the temporal behavior of an exponential decay of the photofragmenting system. In parallel, correlating signals of the produced photofragments will emerge on the corresponding ion channels. In case of fragmentation cascades, multi exponential decay curves become observable, as shown later in Fig. 2.5. Predissociation occurs, when bound and dissociative electronic states are connected by curve crossings or conical intersections. Pump-probe signals taken from their excitation will, therefore, show both: wave packet oscillations of the vibrating molecule superposed by the exponential decay curve of the progressively dissociating system (see Fig. 2.6). The case is most interesting with regard to coherent control scenarios of photoinduced unimolecular dissociation processes. In Sect. 2.2 these three cases will be discussed and experimental examples be given. Then, two examples will be treated theoretically and compared with the experiment: The nonadiabatic fragmentation dynamics of electronically excited Na_2K and the geometrical rearrangement of electronically excited Na_2F.

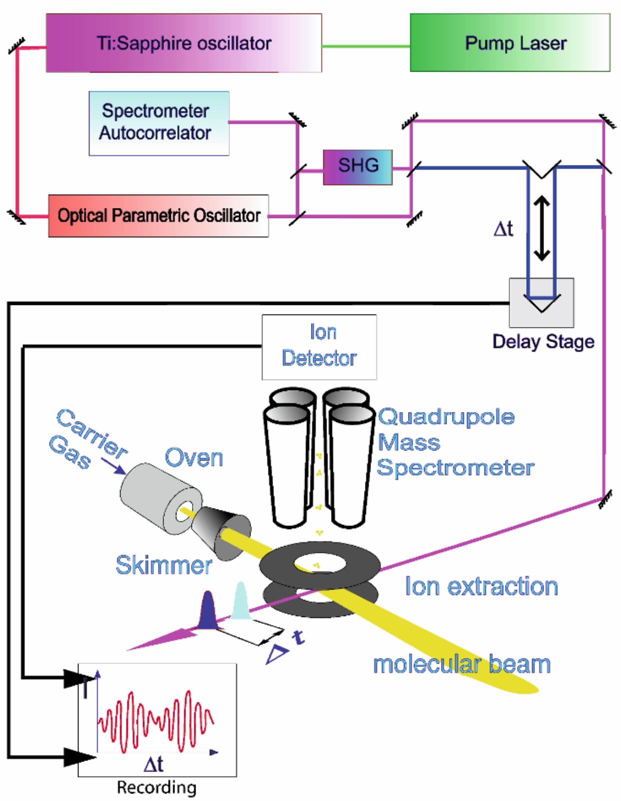

Fig. 2.2. Experimental setup of the pump-probe experiment showing the molecular beam irradiated by laser pulse sequences coming from a Ti:sapphire fs-laser system. The resulting photo-ions are detected across a quadrupole mass spectrometer.

2.2.1 Experimental set-up of the pump-probe experiment

Supersonic molecular beams are an ideal environment to prepare high densities of cold and isolated molecules or clusters and to allow their size-selective observation by means of photoionization mass spectrometry, where pump-probe concepts are easily integrated. The experiments presented here mainly focus on molecules and clusters containing metal atoms. This is due to their pronounced dynamical properties, their highly chromophoric character, and their rather low ionization energies, which are easily reached with the available laser sources. Such metal particle beams are commonly formed by expanding a metal vapor together with an inert or a reactive carrier gas from an oven cartridge across a small nozzle of some microns in diameter into the vacuum. As a result, a collision zone is created in front of the nozzle, in which the molecules and clusters are formed by adiabatic cooling and subsequent nucleation. The typical realization of such an experimental setup is shown in Fig. 2.2. The supersonic molecular beam is extracted from the expansion zone by a skimmer, which leads into a differentially pumped detection chamber. There, an ion extraction system injects the created photo-ions into a quadrupole mass spectrometer (QMS), which is placed perpendicular to the particle beam. Window ports at the detection chamber allow to irradiate the interaction zone perpendicular to both, the neutral particle beam and the extracted ion beam.

For the experiments presented here a commercial Ti:sapphire laser oscillator was used; it was pumped by a frequency-doubled Nd:YLF-, or by an argon-ion laser. The laser operates at a repetition rate of 80 MHz; it is tunable in a wavelength range between 730 and 850 nm producing pulses of 80 fs duration at a total power of 1.6 W. These conditions allow to operate the experiment at a duty cycle of 100%, since each molecule of the continuous molecular beam is irradiated several times by the pulsed laser. Furthermore, the correspondingly low laser peak power prevents undesired multiphotonic transitions, which would camouflage the sought information. The wavelength range of the laser can significantly be extended by using a second harmonic generator (SHG) and/or an optical parametric oscillator (OPO). The employed laser pulses are analyzed by a spectrometer, autocorrelator, and spectrally-resolved cross-correlation (XFROG) . For performing the pump-probe experiment, the laser pulses were split up and recombined in a Michelson interferometer system, allowing to generate pump-probe sequences of a variable delay.

2.2.2 Pump-probe spectra of bound electronically excited states

The result of a pump-probe measurement obtained from $^{39,39}K_2$ is shown in Fig. 2.3. The spectrum was recorded at a pump wavelength of about 834 nm; so the electronic K_2 $A^1\Sigma_u^+$-state is excited. The probe step was achieved by a delayed two-photon transition of the same wavelength (one-color experiment). The signal exhibits a quite distinct oscillatory behavior with vibrational periods of 250 fs, which correspond well to the eigenfrequencies of the photoexcited K_2 A-state. These vibrations, however, are almost harmonically modulated every 10 ps. An explanation for this can be extracted from the corresponding Fourier-transform (FFT) of the recorded signal, which is presented in the insert of Fig. 2.3: Expected is a curve presenting the anharmonic progression of those vibrational states, which were coherently excited within the bandwidth of the pump pulse. The obtained FFT-curve shows spectral resonances around 65 cm^{-1}; this corresponds well to the known vibrational spacing of the A-state of K_2. The obtained intensity distribution, however, shows quite a surprising behavior: Two largely spaced peaks at the wings of the progression dominate the spectrum; they obviously cause the 10 ps large-amplitude modulation of the distinct beat structure. The progression is perturbed [25]. This is caused by a spectrally coinciding spin-orbit coupled “dark” $b^3\Pi_u$-state of $^{39,39}K_2$, which significantly alters the lifetimes and Franck-Condon factors

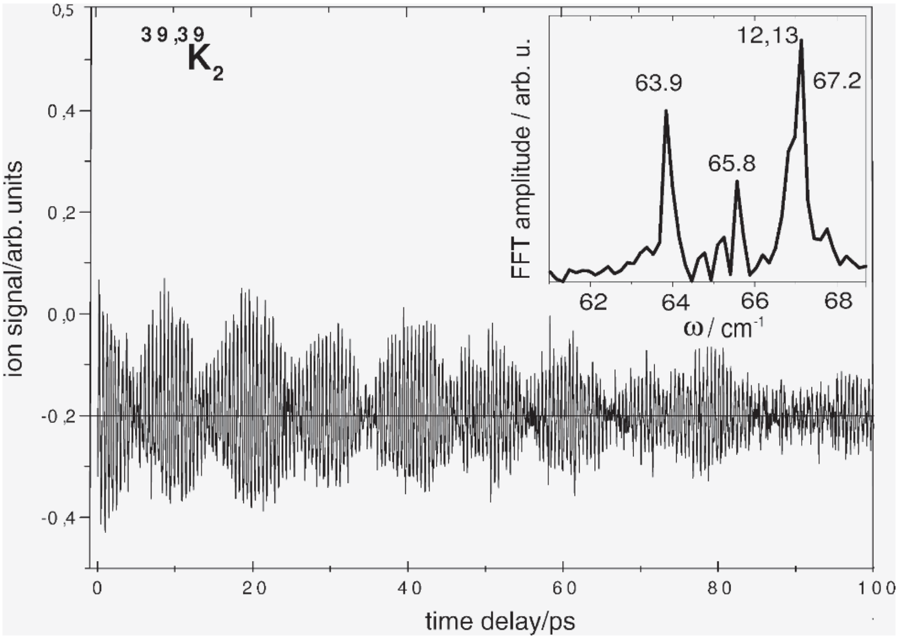

Fig. 2.3. Pump-probe spectrum of electronically excited $^{39,39}K_2$. The insert in the Figure gives the corresponding Fourier-transform of the signal (FFT), which shows the spectral positions of the anharmonic vibrational progression of the excited electronic state. The relative intensities indicate that the sequence is perturbed (see text) [25].

of the observed spectral transition. The phenomenon does not occur for the $^{39,41}K_2$ isotopomer. More details about the differently perturbed systems are given in Sect. 2.2.4.

Transient two-photon ionization experiments on trimer systems were motivated by the need for a time-resolved verification of the pseudo-rotation motion, which can be considered as a superposition of the asymmetric stretch (Q_x) and the bending vibration (Q_y) [26]. In this respect the situation of a triatomic molecule with its three modes is quite different from an isolated oscillating dimer, which vibrates in its single mode until it eventually radiates back to the electronic ground state or predissociates. The coupling of vibrational modes in a trimer system can, therefore, be considered as the onset of internal vibrational redistribution (IVR) [8]. The aspect will be treated later in Sect. 2.2.3 for the example Ag_2Au in great detail.

A typical result for a bound-bound transition in trimers, which was obtained for the electronic Na_3 (B←X)-transition with transform-limited pulses of about 100 fs duration, is shown in Fig. 2.4. The progression shows a pronounced molecular vibration, indicating only one vibrational mode of 320 fs

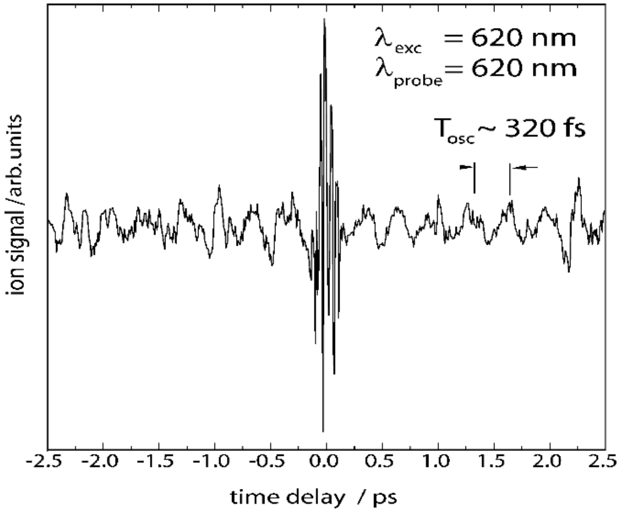

Fig. 2.4. One-color pump-probe spectrum of Na_3 recorded with transform-limited 80 fs pulses at a wavelength of 620 nm. The progression exhibits the symmetric stretch mode of the electronically excited B-state. The dense peak structure in the center is caused by the temporal overlap of the pump and probe pulse, hence it provides an autocorrelation of the employed laser pulse. In the negatively counted time range “pump” becomes “probe”, and “probe” becomes “pump”, so an almost symmetrical spectrum appears [27].

duration, which corresponds to the symmetric stretch (Q_s) mode of Na_3 in the B-state.

2.2.3 Pump-probe spectroscopy of dissociated and predissociated electronic states

Fragmentation becomes more important as the number of internal degrees of freedom inside the molecule or cluster increases. Here again, the fs-pump-probe observation scheme provides a deep insight into the dynamics of photoinduced cluster fragmentation. The principle of such an experiment is indicated in Fig. 2.1b and c. The particles are electronically excited with fs-laser pulses (pump) into a dissociated or predissociated electronic state. There they dissociate, or they oscillate a few times and then dissociate. The temporal behavior of the sequence is monitored with the probe pulse, which interrogates the system by ionizing the excited particles after a variable time delay Δt.

Typical results of time-resolved pump-probe photodissociation experiments across a bound-free transition are presented for sodium clusters of different sizes in Fig. 2.5. The result reveals the rapidly growing number of different dissociation channels for larger aggregates. The two-color pump-probe

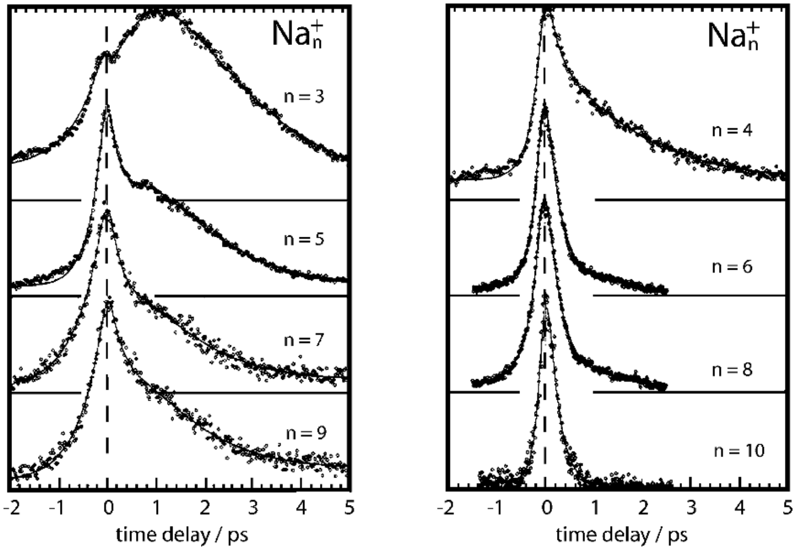

Fig. 2.5. Pump-probe spectra of a two-color experiment probing the bound-free transitions in Na_n $(3 \leq n \leq 10)$. For $\Delta t > 0$: $E_{pump} = 1.47$ eV and $E_{probe} = 2.94$ eV. For $\Delta t < 0$: $E_{pump} = 2.94$ eV and $E_{probe} = 1.47$ eV. [28]

experiments are performed on Na_n with $3 \leq n \leq 10$. For $\Delta t > 0$, the energy E_{pump} was 1.47 eV, whereas E_{probe}, the energy of the probe pulse, was 2.94 eV. Time decays with $\Delta t < 0$ inverted this sequence to $E_{pump} = 2.94$ eV and $E_{probe} = 1.47$ eV. The general trend shows a faster decay with growing cluster sizes. In addition, there is a strong dependence on the excitation wavelength [29]. The size-related increase of fragmentation speed can qualitatively be explained by the growing amount of internal degrees of freedom, which allow -via increasing IVR- to populate more dissociative channels. In order to describe the features, which appear in Fig. 2.5, in more detail, several processes -besides IVR- must be taken into account, as there are the direct fragmentation of the examined cluster size by the pump pulse, and those fragmentation processes that occur to particles, which have populated the observation channel temporarily with fragments of larger clusters, before they fragment again [28].

This fragmentation behavior could be explained in a simple energy level model of the different Na_n cluster sizes [28]. As shown in Fig. 2.5, the temporal evolution of the ion signals exhibits an interesting odd-even alternation as a function of the cluster size, which is associated with two different dissociation channels. Na_n clusters with even n dissociate preferably into an odd numbered cluster and one Na-atom, while odd-numbered clusters dissociate into an odd-numbered cluster and one dimer. However, the cluster size-dependence of the underlying differing decay times is yet not fully understood.

In the case of predissociation one observes both: a wave packet oscillation and an overlaid exponential decay. The result of such an experiment performed on K_3 is shown in Fig. 2.6a. Around $\Delta t = 0$ the signal is at maximum; the occurring signal modulation represents the cross-correlation between the pump and probe pulse. For the following delay time, first a pronounced oscillation occurs, which reflects the wave packet oscillation in the excited state. A magnified segment of this oscillation is shown in Fig. 2.6b, whereas its Fourier-transform is presented in Fig. 2.6c. Three vibrational modes appear; they correspond to the K_3 normal vibrations with $Q_s = 109\ \mathrm{cm}^{-1}$, $Q_x = 82\ \mathrm{cm}^{-1}$, and $Q_y = 66\ \mathrm{cm}^{-1}$. Superposed to these oscillations is an ultrafast unimolecular decay with a lifetime of about 6 ps, which indicates that the observed state is predissociative [30]. This fast fragmentation prevented so far the observation of this excited state by means of stationary resonant multiphoton ionization.

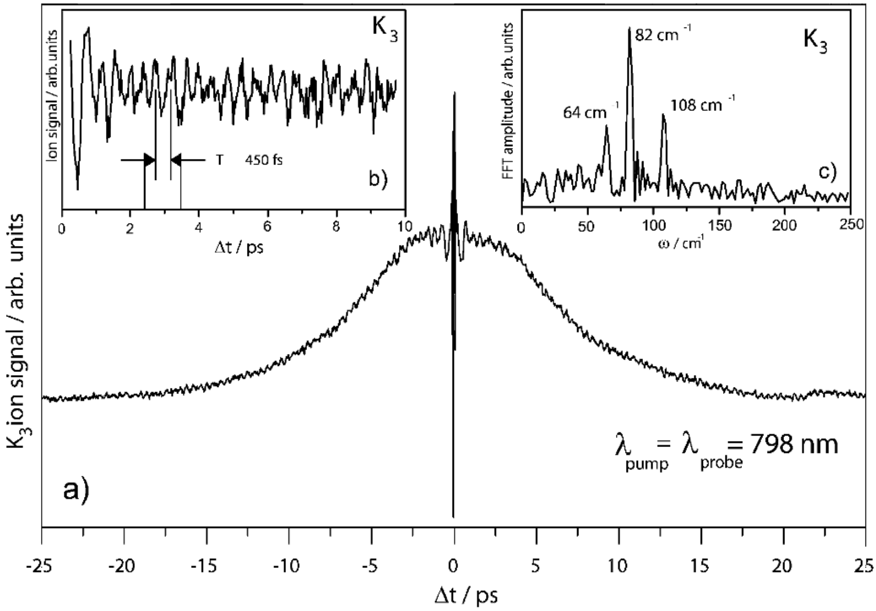

Fig. 2.6. (a) Transient two-photon ionization spectrum of K_3. The spectrum is superposed by a fast unimolecular decay of approx. 5 ps. The progression shows a pronounced oscillation (b). The corresponding Fourier-transform indicates the three normal modes (c). [30]

2.2.4 Experimental and theoretical treatment of the nonadiabatic fragmentation of Na_2K

Trimers are usually considered as simple systems from the theoretical point of view because their potential energy surfaces can be precalculated at a high level of accuracy using different quantum chemical methods. Nevertheless, metallic trimers can have complex electronic structure with a manifold of low lying electronic states violating Born-Oppenheimer approximation as in the case of Na_2K. Here, the Wigner–Moyal representation of the vibronic density matrix for the simulation of pump–probe spectra based on ensembles of classical trajectories is used [31]. According to the experimental conditions, the analytical expression for the signals has been derived under the assumption of weak fields and short pulses, as will be briefly outlined below. The signals are simulated by an ensemble of independent classical trajectories which can be propagated either at precalculated energy surfaces or combined with molecular dynamics (MD) "on the fly". In the case of Na_2K precalculated energy surfaces will be used.

First i) the electronic structure and then ii) the semiclassical dynamics and signals are treated.

i) As already indicated, the mixed alkali trimer Na_2K is characterized by a manifold of electronically excited states. This can be seen from Fig. 2.7, which represents the one dimensional cut along the fragmentation coordinate R_2 for NaK+Na at fixed bond length R_1 (NaK)=3.658 Å and bond angle α=63.79^o. The illustration shows that for the pump–excitation of 1.61 eV, the fragmentation channel NaK (1 $^3\Pi$) and Na (1 ^2S) is not accessible. Therefore, after one photon excitation the fragmentation channel NaK (1 $^3\Sigma^+$) + Na (1 ^2S) can be reached over adiabatic and nonadiabatic transitions involving an avoided crossing between the 5 $^2A'$ and the 6 $^2A'$ states in the former case and the crossings among 5 $^2A'$, 1 $^2A''$ and 4 $^2A'$ states in the latter case. Notice that the bending angle α is an important coordinate for the crossings and therefore all possible transitions cannot be clearly seen from Fig. 2.7.

ii) Semiclassical methods for nuclear dynamics, which make use of classical trajectories with quantized initial conditions, are particularly suitable for exploring ultrafast processes in complex systems. Moreover, the ability to include all degrees of freedom opens a perspective to large systems, where the separation into the chromophore unit and bath is not possible. This approach has theoretically been extended to include quantum effects such as coherence and tunneling in the framework of semiclassical methods [32–35]. It is particularly suitable to use classical trajectories for simple systems, since it allows the comparison with a full quantum dynamical treatment. Therefore, the conceptual aspects are briefly outlined:

Classical MD in different forms, including ab initio MD "on the fly", are now applicable to relatively large systems, and classical trajectories can be used as inputs in semiclassical approaches for simulations of observables. The approach here bases on classical ab initio molecular dynamics (AIMD).

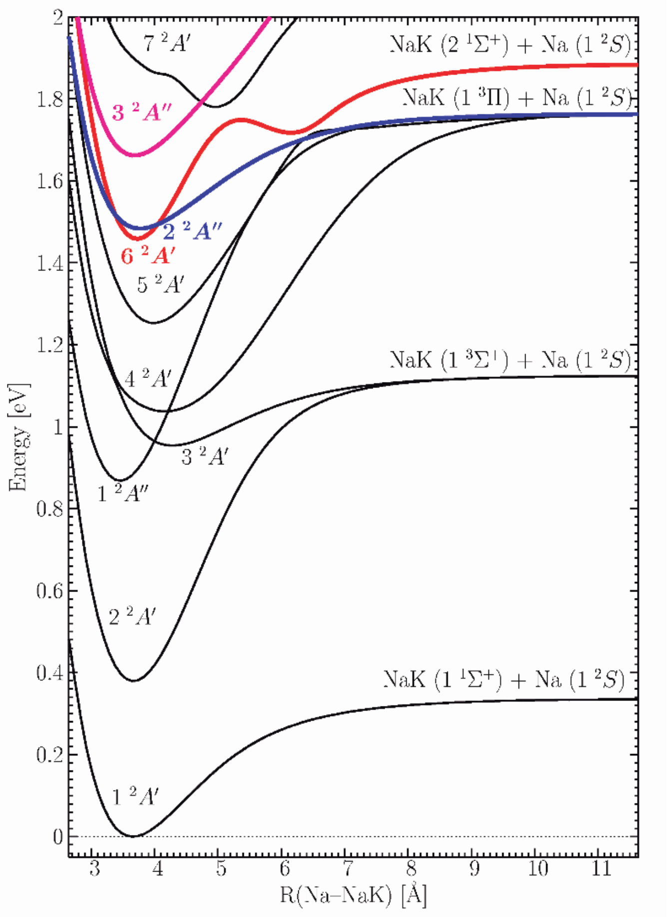

Fig. 2.7. One–dimensional cut of the ground and of nine excited states of Na_2K taken along the coordinate $R_2 = R$(Na2–K) for fixed bond length $R_1 = R$(Na1–K) = 3.658 Å and a bond angle α(Na1–K–Na2) = 63.79°.

The time evolution of the density operator $\hat{\varrho}(t)$ is described by the quantum mechanical Liouville equation

$$i\hbar\frac{\partial\hat{\varrho}}{\partial t} = \left[\hat{H}, \hat{\varrho}\right] \tag{2.1}$$

where $\hat{H}$ is the Hamiltonian of a molecular system involving several electronic states which are coupled with electromagnetic field $\varepsilon(t)$,

$$\hat{H} = \hat{H}_{mol} + \hat{H}_{int} \equiv \sum_a |a\rangle \hat{h}_a(\mathbf{Q})\langle a| - E(t)(\sum_{a,b} |a\rangle \hat{\mu}_{ab}(\mathbf{Q})\langle b| + h.c.), \tag{2.2}$$

with the vibrational Hamiltonian $\hat{h}_a(\mathbf{Q})$ of the adiabatic electronic state a, the collection of vibrational coordinates $\mathbf{Q}$, and the dipole approximation for interaction with the electromagnetic field.

The density matrix formulation offers an appropriate starting point for establishing semiclassical approaches, because the quantum Liouville equation has a well defined classical limit in the Wigner representation, which is given by the classical Liouville equation of nonequilibrium statistical mechanics:

$$\frac{\partial \varrho}{\partial t} = \{H, \varrho\} \tag{2.3}$$

Here $\varrho = \varrho(\mathbf{q}, \mathbf{p}, t)$ and $H = H(\mathbf{q}, \mathbf{p}, t)$ are functions of classical phase space variables $(\mathbf{q}, \mathbf{p})$, and

$$\{H, \varrho\} = \frac{\partial H}{\partial \mathbf{q}} \frac{\partial \varrho}{\partial \mathbf{p}} - \frac{\partial \varrho}{\partial \mathbf{q}} \frac{\partial H}{\partial \mathbf{p}} \tag{2.4}$$

is the classical Poisson bracket. This classical limit can be derived from (2.1) by performing a Wigner transformation [36–38] and expansion in terms of $\hbar$. If this expansion is terminated at the lowest order of $\hbar$ the commutator can be replaced by the classical Poisson bracket:

$$\left[\hat{A}, \hat{B}\right] \rightarrow i\hbar\{A, B\} + O(\hbar^3) \tag{2.5}$$

This leads to the classical equation (2.3). Higher order terms in $\hbar$, are responsible for the introduction of quantum effects in the dynamics. This semiclassical limit of the density matrix formulation of quantum mechanics, based on the Wigner-Moyal representation of the vibronic density matrix offers a methodological approach, which is suited for an accurate treatment of ultrafast multistate molecular dynamics and pump-probe spectroscopy using classical trajectory simulations [31, 39–42].

Keeping the conceptual simplicity of classical mechanics this approach allows an approximate description of quantum phenomena such as optical transitions by averaging over the ensemble of classical trajectories. Moreover, the introduction of quantum corrections can be made in a systematic manner. The method requires drastically less computational effort than full quantum mechanical calculations, and it provides a physical insight into ultrafast processes in complex systems. Additionally, it can directly be combined with quantum chemistry methods for electronic structure. So, the multistate dynamics can be carried out at different levels of accuracy including precalculated energy surfaces as well as the direct ab initio MD "on the fly", in which the forces are calculated, when they are needed in the course of the simulation. The approach is related to the Liouville space theory of nonlinear spectroscopy in the density matrix representation developed by Mukamel et al. (cf. [43]). Following the proposal by Li et al. [39] and formulation given by the authors [31, 40–42], the method is briefly outlined in connection with its application to simulations of the time resolved pump-probe signals, involving both adiabatic and nonadiabatic dynamics.

Assuming that the pump and probe process are both first order in the fields (weak field limit), and assuming that interference and non-Condon effects are negligible, an analytic expression for the pump-probe signal can be derived in the framework of the Wigner distribution approach [31, 40–42, 44]:

$$\begin{aligned} S[t_d] &= \lim_{t\to\infty} P_{22}^{(2)}(t) \\ &\approx \int d\mathbf{q}_0 d\mathbf{p}_0 \int_0^\infty d\tau_1 \exp\left\{-\frac{(\tau_1 - t_d)^2}{\sigma_{pu}^2 + \sigma_{pr}^2}\right\} \times \\ &\quad \exp\left\{-\frac{\sigma_{pr}^2}{\hbar^2}[\hbar\omega_{pr} - V_{21}(\mathbf{q}_1(\tau_1; \mathbf{q}_0, \mathbf{p}_0))]^2\right\} \times \\ &\quad \exp\left\{-\frac{\sigma_{pu}^2}{\hbar^2}[\hbar\omega_{pu} - V_{10}(\mathbf{q}_0, \mathbf{p}_0)]^2\right\} P_{00}(\mathbf{q}_0, \mathbf{p}_0). \end{aligned} \tag{2.6}$$

This expression is valid for adiabatic dynamics and can be interpreted in the following way: At the beginning, the system is prepared in the electronic ground state (0) where the corresponding Wigner distribution $P_{00}(\mathbf{q_0}, \mathbf{p_0})$ is assumed to be known (initial condition). This initial phase space density is spectrally filtered during the pump process to a state 1 by the third Gaussian of (2.6). Subsequently, the filtered ensemble propagates on state 1 and is spectrally filtered again during the delayed probe pulse into state 2. This is expressed by the second Gaussian in (2.6). It is important to notice that the Gaussian form of spectra during the pump and probe process is a direct consequence of both, the classical approximation and the short time limit (cf. [44]). The final time resolution of the signal is determined by the pump-probe autocorrelation function given by the first Gaussian in (2.6).

As can be seen from (2.6) the simulation of pump–probe signals involves averaging over an ensemble of initial conditions. It can naturally be determined from the initial vibronic Wigner distribution $P_{00}^{(0)}$ in the electronic ground state. For this purpose the Wigner distribution of a canonical ensemble in each of the normal modes is computed according to (2.7):

$$P(q,p) = \frac{\alpha}{\pi\hbar} exp\left[-\frac{2\alpha}{\hbar\omega}(p^2 + \omega^2 p^2)\right], \tag{2.7}$$

with $\alpha = tanh(\hbar\omega/2k_bT)$ and the normal-mode frequency ω, corresponding to the full quantum mechanical density distributions. The ensemble of initial conditions needed for the MD on the neutral ground state energies emerges from sampling the phase space distribution given by expression (2.7). This allows one to include temperature effects corresponding with the experimental situations. It permits also to take into account the quantum effects of the initial ensemble at low temperatures.

Expression (2.6) can be generalized to include nonadiabatic effects [42] and simultaneous excitation of several electronic states, which gives the following general analytic expression for the pump–probe signal:

$$S[t_d] \sim \sum_n |\langle \psi_n(0)|\boldsymbol{\mu}|\psi_g(0)\rangle|^2 \cdot \int d\boldsymbol{q}_0 d\boldsymbol{p}_0 \int\limits_0^\infty d\tau_1 \exp\left\{ -\frac{(\tau_1 - t_d)^2}{\sigma_{pu}^2 + \sigma_{pr}^2} \right\}$$
$$\times \frac{1}{N_{Rand}} \sum_\nu \int\limits_{E_{min}}^{E_{max}} dE \exp\left\{ -\frac{\sigma_{pr}^2}{\hbar^2}[E - V_{cat,n(\tau_1)}\{\boldsymbol{q}_{n,\nu}(\tau_1;\boldsymbol{q}_0)\}]^2 \right\}$$
$$\times \exp\left\{ -\frac{\sigma_{pu}^2}{\hbar^2}[E_{pu} - V_{n(0),g}(\boldsymbol{q}_0)]^2 \right\} P_{00}(\boldsymbol{q}_0, \boldsymbol{p}_0) \tag{2.8}$$

which is a modification of (2.6). Equation (2.8) includes:

1. Initial thermal distribution $P_{00}(\boldsymbol{q}_0, \boldsymbol{p}_0)$ for the electronic ground state with the initial coordinates $\boldsymbol{q}_0$ and momenta $\boldsymbol{p}_0$. In the simulations an initial state Wigner distribution is used. The temperature is T=50 K with 1000 starting points for the trajectories running over at least 5 ps. The average over trajectories, which were obtained from different randomizations ν due to the hopping algorithm is expressed by the normalization factor N_{Rand} and by a corresponding summation over ν.
2. Pump pulse window (third exponential in (2.8)) with a pump pulse duration σ_{pu} and a difference between the excitation energy for the pump step E_{pu} and the energy gap $V_{n(0),g}$ between the ground state g and the excited state n of the neutral molecule at the time $\tau_0 = 0$.
3. Probe pulse window (exponential in the second row of (2.8)) with a probe pulse duration σ_{pr}, an energy gap $V_{cat,n(\tau_1)}$ between the current propagating state $n(\tau_1)$ at the time τ_1 and the cationic state at the coordinate $\boldsymbol{q}_{n,\nu}(\tau_1)$. An inclusion of the continuum of the kinetic energy of the detached electron eKE is expressed by the integration over
$$E = E_{pr} - eKE \tag{2.9}$$
for the energy interval $[E_{min}, E_{max}]$.
4. Time window (exponential in the first row of (2.8)) with the pump–probe correlation function located around the time delay t_d, which determines the time resolution of the signal.
5. Weighting factor of the electronic states which is introduced by the square of the norm of the transition dipole moment $\boldsymbol{\mu}$ between the electronic ground state $|\psi_g\rangle$ and the desired excited electronic state $|\psi_n\rangle$ for the ground state equilibrium geometry.

In order to avoid quantitative calculations of the nonadiabatic couplings among the states involved and to use Tully's fewest switches surface hopping procedure [45] for treating the nonadiabaticity, the approach was drastically simplified. The generalization of the Landau-Zener formula has been introduced for the surface hopping probability $p_{n\to i}$ from the current surface labeled by n to the other surface $i \neq n$:

$$p_{n\to i} = \exp\left(\frac{-2\pi(E_i - E_n)^2}{|\boldsymbol{v}\cdot\boldsymbol{\nabla}(E_i - E_n)|}\right) , \tag{2.10}$$

with the energy E_n of the n^{th} surface, the gradient of the energy difference $\boldsymbol{\nabla}(E_i - E_n)$ between the n^{th} and i^{th} surface, and the velocity $\boldsymbol{v}$ at the time τ (note that the atomic units ($\hbar$=1) are used). The probability to remain on the n–th surface is given by:

$$p_{n\to n} = 1 - \sum_{i\neq n} p_{n\to i} . \tag{2.11}$$

A uniform random number between zero and one is used to decide, to which surface to hop. If there is not enough kinetic energy, a hop is rejected.

Simulated and recorded pump–probe spectra

In order to start the simulation of signals the histograms of the corresponding energy gaps between the ground state and the excited states $V_{n(0),g}$ have been calculated, corresponding to Franck–Condon profiles. The results are given in Fig. 2.8. They show that the experimental laser bandwidth covers the upper edge of the energy gap to the 6 $^2A'$ state, although the contribution of the 3

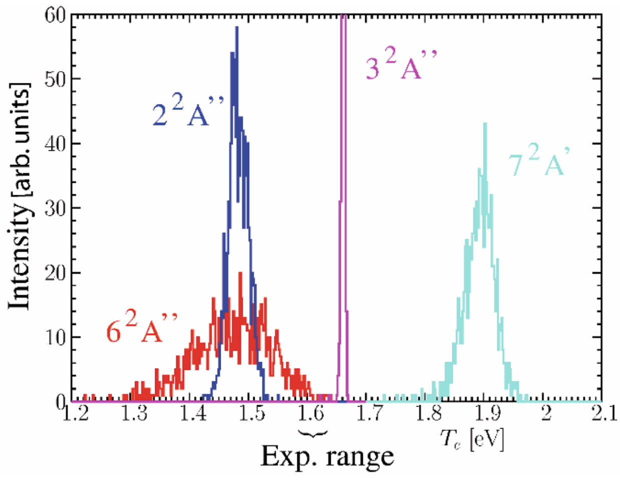

Fig. 2.8. Histograms of energy gaps (transition energies) T_e between the ground and excited states of Na_2K for a 50 K initial ensemble obtained from 1000 sampled phase points of a canonical Wigner distribution.

$^2A''$ state, which is separated by 0.026 eV from the experimental range cannot be excluded. Also the 2 ^{2}A" state is close enough and must be considered. In contrast, the mean value of the energy gap for the 7 ^{2}A' state is more than 0.2 eV separated from the experimental range. It is, therefore, excluded from further considerations.

First the energy gaps between the cationic ground state and excited electronic states of the neutral Na_2K are presented in Fig. 2.9; they reveal dynamical processes, which will be mirrored in the pump–probe signals. The energy interval of the energy gaps differs drastically for the different excited states. Due to the similarity between the electronic ground state and the 3 $^2A''$ state, the energy difference is nearly constant over a wide range, which results in a small energy interval. In contrast, the substantial change in the energy difference between the 6 $^2A'$ state and the electronic ground state around the equilibrium geometry of the latter induces the broad energy interval of the energy gap. The 2 $^2A''$ state is located in between. Therefore, it gives rise to a medium size energy interval. So, by choosing different probe pulse energies, the dynamical features, which correspond to different electronic states, can selectively be probed.

The horizontal lines in Fig. 2.9 indicate important energies: E_{gap}=3.22 eV corresponds to the zero kinetic energy of the detached electron (ZEKE) in a two photon ionization process. E_{gap}=2.62 eV and E_{gap}=2.12 eV represent the restricted and the full continuum, respectively. In Fig. 2.9a the bunch of trajectories shows an oscillation period of 290 fs, which is slightly more than half of the oscillation period of the bending vibration of the 3 $^2A''$ state. No hopping to other excited states occurs with the exception of one trajectory.

If the molecular dynamics is started in the 2 $^2A''$ state (Fig. 2.9b) a fragmentation can be observed after 1 ps. The oscillatory feature, which shows a periodicity of 870 fs, is assigned to the bending vibration of the 2 $^2A''$ state. This will be discussed later. The E_{gap}=2.45 eV indicates MD on the 6 $^2A'$ state. Trajectories in the energy range between 2.45 and 3.35 eV reveal the molecular dynamics on the 2 $^2A''$, 1 $^2A''$, 5 $^2A'$ and 4 $^2A'$ states without fragmentation.

Figure 2.9c shows that 80% of the trajectories diverge within the first 5 ps, which indicates that fragmentation takes place. Thus, fragmentation is a dominant process in this case. The low energy features reveal again dynamics occurring on the 6 $^2A'$ state. Contrary to Fig. 2.9b, however, no oscillations occur, and therefore no stable dynamics can be initiated in the 2 $^2A''$ state. The remaining trajectories reveal dynamics in lower lying states.

It is important to realize that the characteristic features of the pump–probe signals depend significantly on the kinetic energy taken into account. Similar to the cases of NeNePo spectroscopy (cf. Sect. 2.3), the ZEKE conditions provide better resolution of underlying processes in contrast to those cases with excess kinetic energy for which the integration over the energy (continuum) must be considered. Therefore, two sets of results are presented here. First, continuum with restricted values was taken into account (Fig. 2.9d and

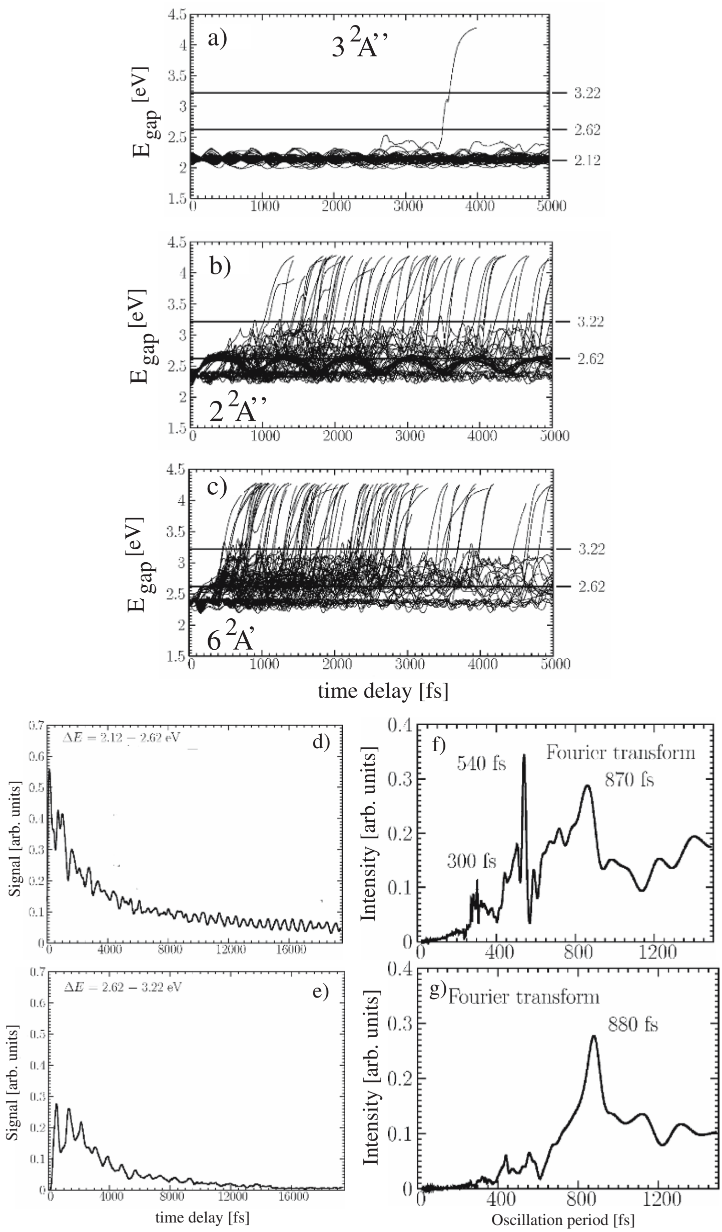

Fig. 2.9. Bunches of energy gaps between the neutral excited states and the cationic ground state of Na_2K (E_{gap}) for 100 representative trajectories which started on a) 3 ^{2}A", b) 2 ^{2}A", and c) 6 ^{2}A' states. An initial temperature of 50 K was assumed. The values of 3.22, 2.62, and 2.12 eV correspond, respectively, to ZEKE (see below), to the lower limit of the restricted, and to the full continuum. Simulated pump–probe signals account (d) $\Delta E = E_{pr} - e\mathrm{KE} = 2.12$ – 2.62 eV and (e) $\Delta E = 2.62$ – 3.22 eV. The corresponding Fourier transforms are given in f) and g).

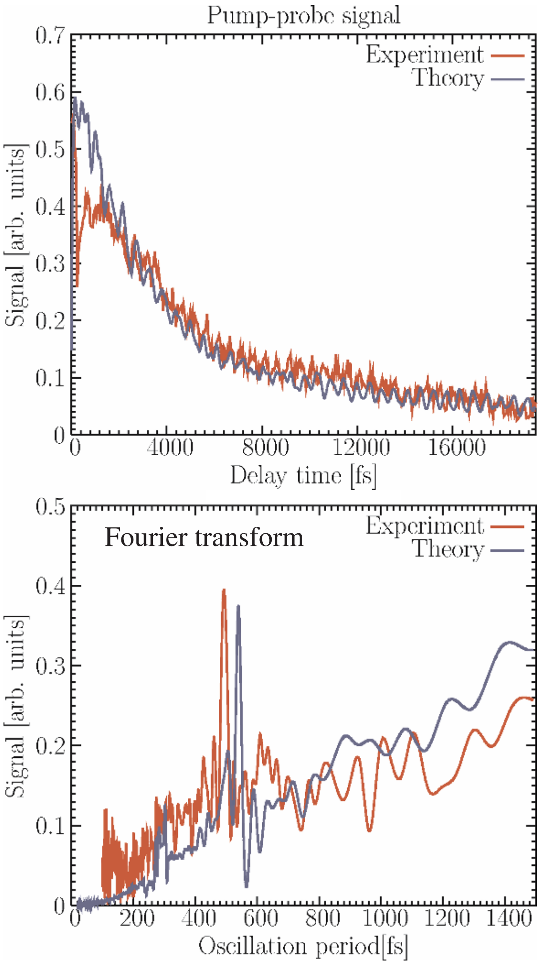

Fig. 2.10. Comparison of theory and experiment for the pump-probe signal of the nonadiabatic fragmentation of electronically excited Na_2K and the relating Fourier transform signal [46].

e) and then the complete continuum (Fig. 2.10), which corresponds better to the experimental conditions [46]. In the first case, different oscillations can be revealed in the pump–probe signals. From the Fourier transforms (cf. Fig. 2.9f and g) it is possible to identify the period of oscillations and to assign them to the particular vibrational mode within the given electronic state. In the case of complete continuum some characteristic features such as oscillations of a particular vibronic mode can easily be smeared out. This can be seen from a comparison of Figs. 2.9 and 2.10.

For the continuum restricted to the energy intervals $I_1 = [2.12 - 2.62]$ and $I_2 = [2.62 - 3.22]$ eV (cf. energy gaps of Fig. 2.9) the pump–probe signals calculated using Eq. 2.8 are given in Fig. 2.9d and e. The corresponding Fourier transforms are given in Figs. 2.9f and 2.9g, respectively. The pump–probe signals decay, but the oscillatory behavior exhibits characteristic features of the 3 $^2A''$ state (Fig. 2.9a) and of the 2 $^2A''$ state (Fig. 2.9b). The oscillation period of 540 fs can be assigned to the bending vibration mode and the oscillation period around 300 fs corresponds to the stretching vibration, both characterizing the 3 $^2A''$ state, as it can be seen from Fourier transforms of Fig. 2.9f. The decay of the signal with an oscillatory feature with the period of 870 fs stems from the bending mode on the 2 $^2A''$ energy surface. The pump–probe signal shown in Fig. 2.9d exhibits mainly features of the 2 $^2A''$ state alone. This is due to the negligible contribution of the 3 $^2A''$ state and the signature of the 6 $^2A'$ state only during earlier times. In the Fourier transform, the peak corresponding to an oscillation period of 870 fs represents the main contribution; it can be assigned to the bending vibration of the 2 $^2A''$ state.

After including the full continuum, the oscillatory behavior with a period of $\sim$ 870 fs is completely suppressed, as shown in Fig. 2.10a. At early times the signal is characterized by an oscillation period of 300 fs for the symmetric stretch and 520 fs corresponding to the bending vibrational modes. At later times the oscillation of the bending mode dominates. These features are confirmed by the Fourier transforms shown in Fig. 2.10b.

The results in Fig. 2.10b clearly indicate that the pump–probe signal obtained from (2.8), which accounts for full continuum is in excellent agreement with experimental findings [46]. This allows to conclude that the experimental results are strongly influenced by the excess kinetic energy of the ionization step. The only fingerprint of an individual electronic state which remains present in the experimental and theoretical signal is the oscillatory structure with a period of 540 fs, which corresponds to the 3 $^2A''$ state.

Altogether, the analysis shows that nonadiabatic dynamics over several excited states of Na_2K leads to a decay of the pump–probe signal which corresponds to the fragmentation process of the photoexcited system. Time scales and mechanism of the underlying processes can easily be determined, if the kinetic energy excess is restricted is in accordance with the experimental results.

2.2.5 Experimental and theoretical treatment of the geometrical rearrangement in electronically excited Na_2F

In comparison with metallic trimers the replacement of one metal atom by a fluorine atom, which leads to the Na_2F trimer with polar Na–F bonds, simplifies the situation drastically, since the first excited state is well separated from other excited states, and it has relatively low transition energies [41,47,48]. Therefore, the time resolved theoretical and experimental studies of this system offer the opportunity to identify the time scales of adiabatic processes in the pump-probe spectra [41, 49]. Again, the Wigner–Moyal representation of the vibronic density matrix for the simulation of pump–probe spectra based on ensembles of classical trajectories is used [31]. The analytical expression for the signals was again derived under the assumption of weak fields and short pulses (cf. (2.6)). The signals are simulated by an ensemble of independent classical trajectories, which are obtained for Na_2F from ab initio molecular dynamics "on the fly" involving excited electronic states.

Due to one excess electron in Na_2F, an accurate description of the excited states is particularly simple; it is even possible in the framework of the one–electron "frozen ionic bonds" approximation [41]. In this method the optical response of a single excess electron can explicitly be considered, in the field of the other (n-1) valence electrons, which are involved in the strongly polar ionic Na–F bonding (cf. [41]). In the framework of this approach, the fast computation of the adiabatic MD "on the fly" is particularly favorable and can be combined with (2.6) derived in the framework of the Wigner distribution approach. The only difference is that now the ground state and the first excited state of the neutral Na_2F are involved, as well as the ground state of the cationic Na_2F for probing.

After vertical excitation, the conformational change in the first excited state of Na_2F starts from the triangular ground state geometry and leads then to the linear structure. Considerable lowering of the energy in the excited state occurs as shown in Fig. 2.11a. A relatively small energy gap between the ground and the first excited state is a consequence of an avoided crossing, obtained from breaking the Na-Na bond and overshooting the linear geometry connecting two equivalent triangular geometries. In spite of the avoided crossing, the nonadiabatic coupling is weak and therefore adiabatic dynamics can be performed.

As a starting point the generation of a temperature dependent initial Wigner phase space distribution on the neutral ground state is needed. A canonical thermal ensemble at a given temperature is suitable for low temperatures at which a harmonic approximation holds. This initial ensemble has to be brought to the first excited state with a Franck-Condon transition probability, which involves the corresponding excitation energies shown in Fig. 2.11C. The propagation of this ensemble on the first excited state involves classical trajectory simulations. The probe window includes the time-dependent energy gaps between the cationic and the neutral excited states, taken at the propagated coordinate (cf. Fig. 2.11 B-a). The calculation of the signal requires a summation over the entire phase space (cf. Fig. 2.11 B-b).

The results presented in Fig. 2.11B are based on simulations using an ensemble of 300 classical trajectories at an initial temperature of 300 K, which corresponds to the experimental conditions [49]. The theoretically and experimentally obtained results are given in Fig. 2.11B. Pulse duration and laser wavelength used in the experiment and in the simulations are shown in Fig. 2.11B. The probe wavelength of 3.06 eV corresponds to the minimum of the

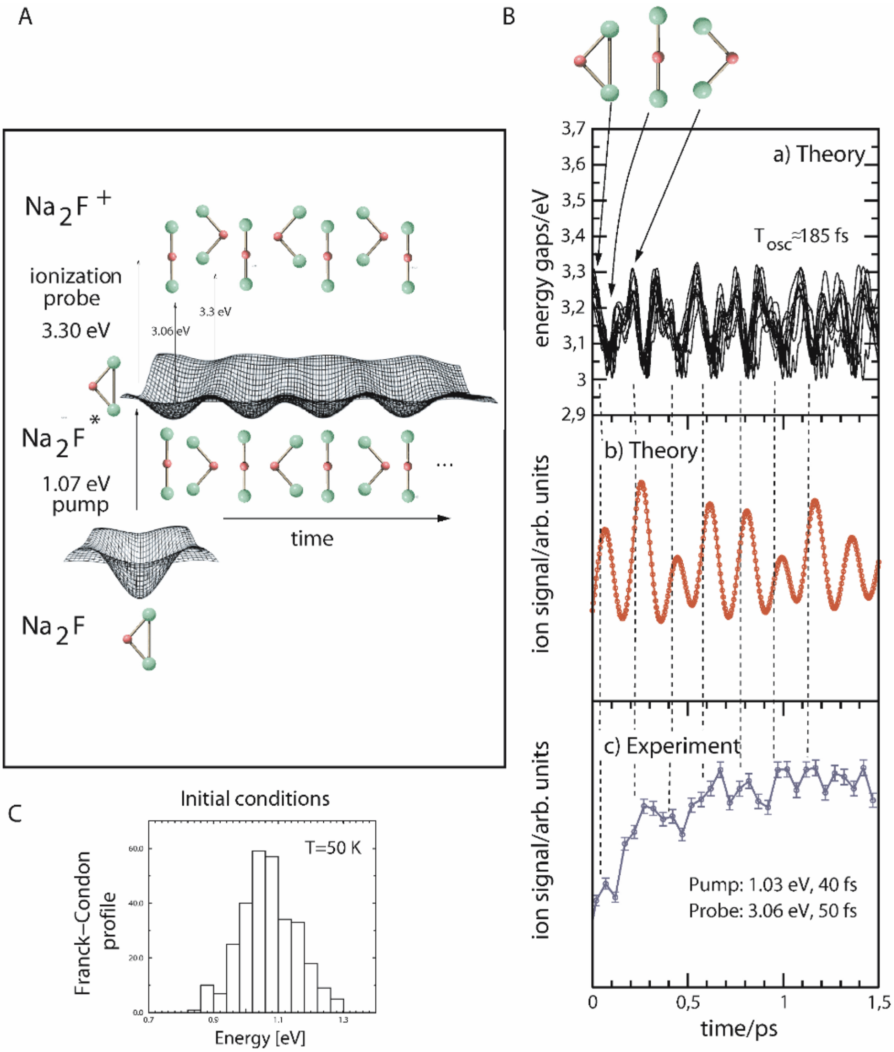

Fig. 2.11. A) Pump-probe NeExPo scheme for Na_2F involving the neutral ground state (Ne), the electronic excited state (Ex), and the cationic ground state (Po). B) Temperature dependent (T=50 K) initial conditions; histogram of transition energies between first excited and ground state. C) Comparison of theoretical with experimental results [49]: (a) bunch of energy gaps between the first excited states of Na_2F and the cationic ground state reflecting the dynamics in the first excited state; (b) simulated pump-probe signal; (c) experimentally observed transient. The involved structures are shown in the top panel. [49]

first excited state with a linear geometry, as can also be seen from Fig. 2.11A. From the bunch of the time dependent energy gaps shown in Fig. 2.11B-a the periodic relaxation dynamics with a period of ≈ 185 fs can be identified. The maxima correspond to the bent and the minima to the linear structures. At longer times, anharmonicities in the bending mode introduce aperiodicity. Because the energy gaps are essential for the determination of fs pump-probe signals, the oscillations in the simulated signal have the same period of 185 fs, as can be seen from Fig. 2.11B-b. Since the linear geometries are probed for an ionization energy of 3.06 eV, they give rise to maxima in the signal. The periodic feature of the signal allows the identification of structural rearrangements from triangular to linear geometry during the butterfly type relaxation dynamics in the first excited state of Na_2F. This occurs due to the breaking of the Na-Na metallic bond. The strong Na-F ionic bonds on the other hand remain almost intact, which hinders fragmentation to take place. The period of 185 fs corresponds to half of the normal bending mode frequency in the first excited state. Therefore, the observed oscillations can be assigned primarily to the bending mode. Consequently the IVR is very small, because the stretching modes do not significantly contribute. This means that the time scale for the metallic bond breaking is $\sim$ 90 fs. A recorded transient Na_2F ion signal is shown in Fig. 2.11B-c. The comparison of the theoretical pump-probe signal (Fig. 2.11B-b) with the experimentally obtained transient (Fig. 2.11B-c), shows very good agreement. Both curves exhibit oscillations with a period of 185 fs corresponding to a periodic butterfly type rearrangement between bent and linear geometries [49]. It is important to notice that theoretical predictions [41] have initiated the experimental work, which confirmed predicted findings and consequently the proposed simple theoretical approach. In fact, theoretical results on Na_2F based on quantum mechanical dynamics and precalculated energy surfaces [50] fully support the theoretical results presented in Fig. 2.11. Therefore the conclusion can be drawn that excited state dynamics in the framework of the "frozen ionic bond" approximation, combined with the Wigner distribution approach is capable to describe accurately processes on the femtosecond time scale.

2.3 Probing the dynamics of the transition state

V. Bonačić-Koutecký, T. M. Bernhardt, R. Mitrić, L. Wöste, and J. Jortner

As shown before, pump-probe spectroscopy allows the investigation of ultrafast nuclear dynamics in molecules and clusters during the geometric transformation along the reaction coordinates. This involves the preparation of a transition state by optical excitation of a stable species into a nonequilibrium nuclear configuration in the pump step, and the probing of its time evolution by laser induced processes. Neumark et al. and Lineberger et al. have demonstrated that such nonequilibrium can also be produced by vertical photodetachment of stable negative ions. The state of the neutral species can be close to the stable geometry of anions [51–60], or it can provide the starting point for an isomerization process in the neutral ground state [61–63]. The vertical one-photon detachment spectroscopy was advanced by introducing the charge reversal (NeNePo) pump-probe technique [8, 9]. The approach employs, after preparing the system by vertical photodetachment from its anion, a time delayed probe pulse to ionize the vibrationally excited neutral molecule to a positive ion. This allows to probe structural processes and isomerization relaxation and internal vibrational energy redistribution (IVR) in neutral molecules and clusters as a function of the cluster size and composition. An extension of the NeNePo technique by two-color pump- excitations has been also proposed [64]. As shown in Chap. 3, besides the NeNePo approach, also time resolved photoelectron spectroscopy [51] is a powerful technique, which can be applied to study dynamics of molecules and clusters [51].

In theory, the conceptual framework and scope of ultrafast spectroscopy is provided by simulations which allow to determine the time scales and the nature of configurational changes as well as IVR in vertically excited or ionized states [31,40–42,65–68]. The separation of the time-scales of different processes is essential for identifying them in the experimentally observed features. Moreover, the distinction between resonant and dissipative IVR in finite systems can be addressed as a function of the molecular size and its atomic composition. For the investigation of the dynamics in fs-spectroscopy, the generation of the initial conditions and multistate dynamics for the time-evolution of the system itself and for the probe or the dump step are needed. For this purpose, two basic requirements have to be fulfilled. First, accurate determination of electronic structure is mandatory. In the case that the electronic states involved are well separated, the Born-Oppenheimer approximation is valid and the adiabatic dynamics is appropriate, as it is usually the case for the ground states involved in the NeNePo spectroscopy. The second basic requirement is the accurate simulation of ultrafast observables such as pump-probe signals. This involves an appropriate treatment of optical transitions such as ultrafast creation and detection of the evolving wave packet or classical ensemble. In the latter case, the dynamics is described by classical mechanics, and the average over a sufficiently large number of trajectories has to be made in order to simulate the spectroscopic observables.

Since atomic clusters, in particular with metallic atoms [69], usually do not contain a “chromophore type” subunit and do not obey regular growth patterns [70], it is mandatory to include all degrees of freedom in the simulation of dynamical processes. Consequently, first principle (ab initio) molecular dynamics “on the fly” (AIMD), without precalculation of the energy surfaces, represents an appropriate choice to study ultrafast processes in elemental clusters with heavy atoms for which in the first approximation, the classical description of nuclear motion, is acceptable. The basic idea is to compute forces acting on nuclei from the electronic structure calculations which are carried out “on the fly” [71]. Related AIMD methods with plane wave basis sets have significantly contributed to the success of the method applied to clusters [72].

2.3.1 Multistate adiabatic nuclear dynamics and simulation of NeNePo signals

The goal of theoretical fs-NeNePo spectroscopy is to provide conditions under which different processes and their time scales can be observed and to establish the scope of this experimental technique [31, 67, 68, 73].

To illustrate these goals, first the electronic and structural properties of noble metal clusters will be addressed. Then attention will be paid to MD "on the fly" and to the theoretical approach for the simulation of signals. Furthermore, the analysis of the signals and the comparison with the experimental findings will be presented allowing for the identification of processes and conditions under which they can be observed. Finally, reactivity aspects and the scope of NeNePo spectroscopy will be addressed.

2.3.1.1 Electronic structure

Noble metal molecules are good candidates for probing multistate adiabatic nuclear dynamics because of their relatively simple electronic structure in comparison with transition metals, and their similarity to s-shell alkali metals. Their structural, reactive, and optical properties have attracted numerous theoretical [66–68, 74–87] and experimental studies [86–100] over the years. This is particularly the case for silver clusters with a large s-d gap in contrast to gold clusters. In the latter case, the s-d gap is considerably smaller, due to the relativistic effects which strongly lower the energy of the s-orbital. These differences in the electronic structure are also reflected in different structural properties of small silver and gold clusters [78, 79, 86, 87]. Increasing interest in gold and silver clusters is due to their newly discovered size-selective reactivity toward molecular oxygen and carbon monoxide [80–83, 101–104]. All together, the noble metal clusters represent an attractive research direction for fs-chemistry.

Relativistic effective core potentials (RECP) are mandatory for accurate theoretical description of these species. Gradient corrected density functional theory (GDFT) is presently the method of choice for the ground state properties of metallic clusters provided that the exchange and correlation functionals used, allow for the accurate determination of binding energies and structural properties, which is not always the case [81]. This is particularly important for a reliable calculation of the energy ordering of different isomers, which assume related or very different structures with close lying energies.

In the early work on ground state structural properties of neutral and charged silver clusters one-electron relativistic effective core potentials (1e-RECP) with corresponding AO basis sets were developed [74–76], which have been later revisited in connection with the DFT method [67] employing Becke and Lee, Yang, Parr (BLYP) functionals [105, 106] for exchange and correlation. The justification for the use of 1e-RECP is that the d-electrons are localized at the nuclei of the silver atoms, and almost do not participate therefore in bonding. Recent DFT calculations on structural properties using 19e-RECP, and ion mobility experiments carried out on Ag_n^+ [87] clusters, have confirmed the early findings [74, 75].

In contrast, the use of 1e-RECP for gold clusters might be useful only if the results agree with those obtained from 19e-RECP, due to the fact that the former one is computationally less demanding (for details cf. reference [79]). Moreover, for reactivity studies involving oxidized clusters, 19e-RECP is mandatory also for silver clusters which is due to the activation of d-electrons by p-electrons of the oxygen atom [81–83].

2.3.1.2 NeNePo pump–probe signals

Semiclassical molecular dynamics using classical trajectories with quantized initial conditions in the frame of Wigner distribution approaches outlined in Sect. 2.2.4 will be used for the simulation of NeNePo signals. For this purpose (2.6) is modified as follows:

$$\begin{aligned} S[t_d] &= \lim_{t\to\infty} P_{22}^{(2)}(t) \\ &\approx \int d\mathbf{q}_0 d\mathbf{p}_0 \int_0^\infty d\tau_1 \exp\left\{-\frac{(\tau_1 - t_d)^2}{\sigma_{pu}^2 + \sigma_{pr}^2}\right\} \times \\ &\quad \exp\left\{-\frac{\sigma_{pr}^2}{\hbar^2}\left[\hbar\omega_{pr} - V_{neu,po}(\mathbf{q}_1(\tau_1; \mathbf{q}_0, \mathbf{p}_0))\right]^2\right\} \times \\ &\quad \exp\left\{-\frac{\sigma_{pu}^2}{\hbar^2}\left[\hbar\omega_{pu} - V_{neu,neg}(\mathbf{q}_0, \mathbf{p}_0)\right]^2\right\} P_{00}(\mathbf{q}_0, \mathbf{p}_0). \qquad (2.12) \end{aligned}$$

where $V_{neu,neg}$ and $V_{neu,po}$ are the energy gaps between the neutral and anionic state and between cationic and neutral states, respectively. For the simulation of the NeNePo signals the initial conditions are obtained using (2.7).

Notice that (2.12) corresponds to zero electron kinetic energy conditions (ZEKE). Usually in NeNePo experiments these conditions are not satisfied and therefore the integration over the excess kinetic energy of the photoelectrons has to be carried out and expression (2.12) adequately modified.

2.3.1.3 Experimental setup for NeNePo spectroscopy

The accurate temperature control of the initial molecular cluster ensemble in the NeNePo experiment is an important issue and has already been emphasized [68]. Only through the experimental knowledge of the temperature parameter, a detailed comparison with theoretically obtained NeNePo signals

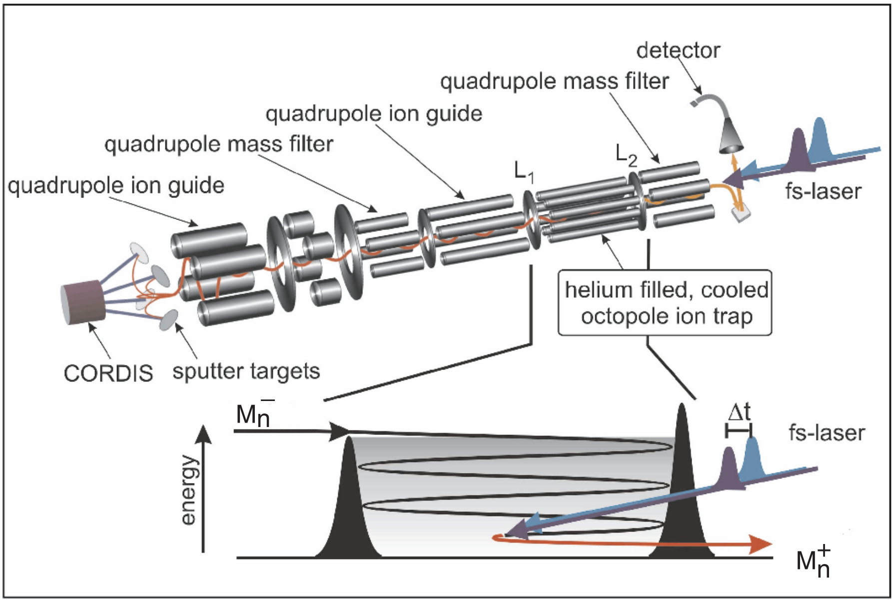

Fig. 2.12. Schematic representation of the setup for the temperature-controlled NeNePo pump-probe experiment. The upper part illustrates the arrangement of the particle source, the quadrupole mass filter and ion guides, and of the octupole ion trap with entrance and exit lenses L_1 and L_2. The process of trapping and cooling molecules inside the octupole ion trap is schematically depicted in the lower part [68].

becomes possible and different contributions to the observed nuclear dynamics can be distinguished. Therefore, the original experimental setup [8, 107] had been extended to enable the control of cluster temperature in the range between 20 and 300 K [108]. The NeNePo experiment was carried out in a helium filled, temperature variable radio frequency (rf)-octopole ion trap. The complete experimental setup is depicted in Fig. 2.12 [68]. The strong effect of the temperature on the observed nuclear dynamics is apparent from the NeNePo signals depicted in Fig. 2.14a. The molecular ions are generated by sputtering metal targets with accelerated xenon ion beams (CORDIS-source [109]). The emerging anions are subsequently mass-filtered and guided into the octupole ion trap (cf. upper part of Fig. 2.12). Inside the ion trap the cluster ions rapidly loose energy by collisions with the helium buffer gas (cf. lower part of Fig. 2.12) and perfect thermalization is reached within a few milliseconds. The ions are spatially confined by the rf-field and the electrostatic potential of octupole entrance and exit lenses. The average residence time of the molecular anions in the octupole ion trap before interaction with a laser pulse is on the order of a few hundred milliseconds. The femtosecond laser beams enter the rf-ion trap collinearly with the axis of the apparatus from the opposite side

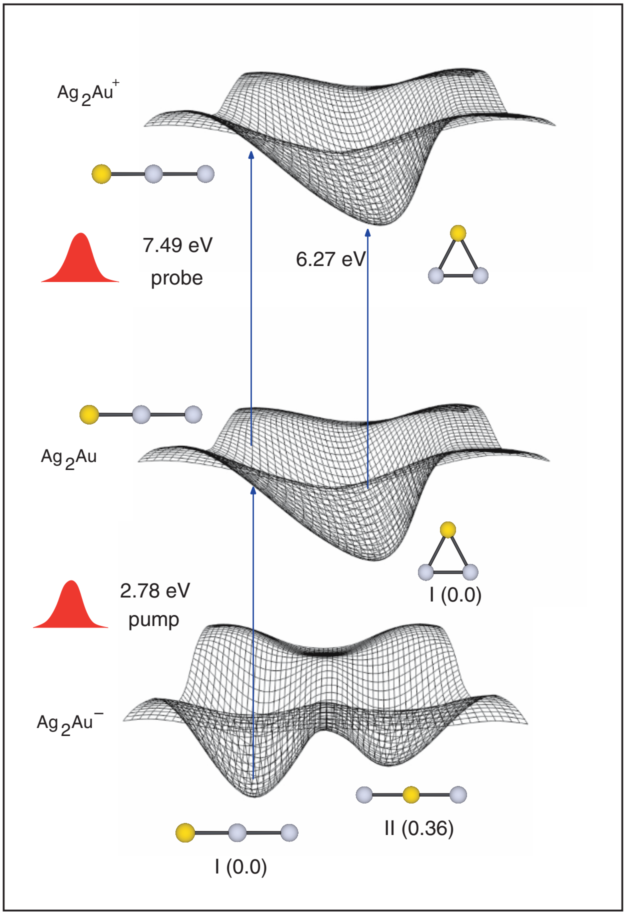

Fig. 2.13. Scheme of the multistate femtosecond dynamics for NeNePo pump-probe spectroscopy of Ag_2Au with structures in different charge states and energy intervals of the pump and probe steps.

as the injected ions. The first ultrafast laser pulse (pump) then detaches the excess electron of the anion resulting in a neutral cluster in the geometry of the anion. This leads to nuclear relaxation dynamics, which can be probed in real-time by femtosecond time-delayed ionization of the cluster to the cationic state (probe). As soon as cations are prepared inside the ion trap, they will be extracted by the electrostatic field of the octupole exit lens and can be mass analyzed with the final quadrupole mass filter. The recorded ion current at the detector as a function of the pump-probe delay time Δt gives rise to the transient NeNePo signal that reflects the time dependent ionization prob-

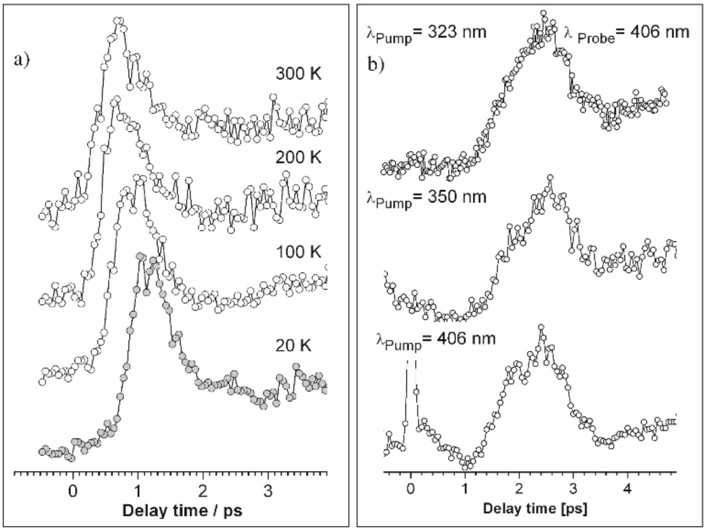

Fig. 2.14. a) NeNePo signal for Ag_2Au obtained at different ion trap temperatures. Note the change of the signal with increasing temperature. For the interpretation of the signal at T=20 K see text and Fig. 2.16. b) Ag_2Au NeNePo signal obtained at three different pump (electron detachment) energies. Note that the dynamics at 406 nm probe wavelength is independent of the pump photon energy. The peak at t=0 fs for the one-color experiment is due to pump-probe interferences (lower trace).

ability of the neutral clusters due to the nuclear dynamics initiated by the initial photodetachment. However, only by comparison of transient NeNePo signals with theoretically simulated signals the conditions can be identified under which a ZEKE-like situation can be achieved, as illustrated below.

2.3.1.4 Geometry relaxation and onset of IVR in the Ag_2Au trimer

The mixed silver-gold trimer $Ag_2Au^-/Ag_2Au/Ag_2Au^+$ has been chosen as an example to demonstrate the ability of the ab initio Wigner distribution approach to accurately predict the NeNePo signals, to interpret them, and to identify conditions under which the separation of time scales of processes, such as geometric relaxation and IVR can be achieved. This has been realized by using the experimental setup at low temperature and close to the zero-kinetic energy electron (ZEKE) conditions as described above. Furthermore, the aim was to study the influence of the heavy atom on the time scale of fs-processes since a comparison with the "light" Ag_3 trimer [31] can be made. The simulations of the NeNePo pump-probe spectra have been performed by using the ab initio Wigner distribution approach combined with the ab initio MD "on the fly" in the framework of the density functional theory [67, 68] as described above. The mixed Ag_2Au trimer has the following structural properties: the anionic Ag_2Au^- trimer assumes a linear structure with one Au-Ag heterobond. The symmetric linear isomer with two hetero Ag-Au bonds lies 0.36 eV higher in energy. In the neutral state of Ag_2Au both linear structures are transition states between the two equivalent triangular geometries which correspond to the most stable structure. In the cationic state the obtuse triangle is the minimum. It is important to notice that the structural properties of these mixed trimers are sensitive to the details of the methodological treatment like the choice of RECP and of the functional in the DFT procedure. Therefore, the explicit treatment of d-electrons is necessary for quantitative considerations. The energetic scheme relevant for NeNePo together with the structural properties of the neutral and the charged Ag_2Au is shown in Fig. 2.13.

Since for the simulations the initial temperature of 20 K has been chosen in correspondence with the experimental conditions, it can be assumed that only the most stable structure is populated in the anionic state. Under these conditions, the harmonic approximation is valid and therefore the initial conditions for the MD simulations have been obtained by sampling from the canonical Wigner distribution given in (2.7). Due to the low temperature the Franck-Condon transition probabilities to the neutral state assume an almost Gaussian shape centered around 2.78 eV. The experimentally determined adiabatic detachment energy of Ag_2Au^- amounts also to 2.78 eV [100]. The first excited neutral state is separated from the anion by about 4 eV [100]. Pump photon energies of 2.78 eV and 4.00 eV should, therefore, be suitable to prepare the neutral Ag_2Au in the electronic ground state. The experimental transient NeNePo signals do indeed show the same temporal evolution independently from the pump wavelength (Fig. 2.14b).

In order to simulate the NeNePo signals, an ensemble of trajectories (e.g. ~ 500) has to be propagated in the neutral state, and the time-dependent energy gaps to the cationic state need to be calculated along the trajectories. The energy gaps are presented in Fig. 2.15. They provide visual information about the time evolution of individual processes such as the onset of geometrical changes and of IVR. Within the first 2 ps after the photodetachment, the swarm of energy gaps decreases from 7.5 eV to 6.5 eV, and subsequently all energy gaps exhibit oscillations in the energy interval between 6.1 and 6.5 eV. This allows to distinguish two different types of processes: i) the geometric relaxation from the linear toward the triangular structure, taking place within the first 2 ps and ii) subsequent IVR process within the triangular structure. The minimum energy gap value of ~ 6.1 eV corresponds to the structure with the closest approach of the terminal silver and gold atoms, which is referred to as an internal collision within the cluster. Therefore the adjustment of the pump-probe energies experimentally allows to probe these processes. The highest value of the IP is 7.5 eV, choosing higher probe pulse energy will lead to the signal which is rising very rapidly and which subsequently remains constant due to the contribution of the continuum. Pulse energies between 6.5 eV

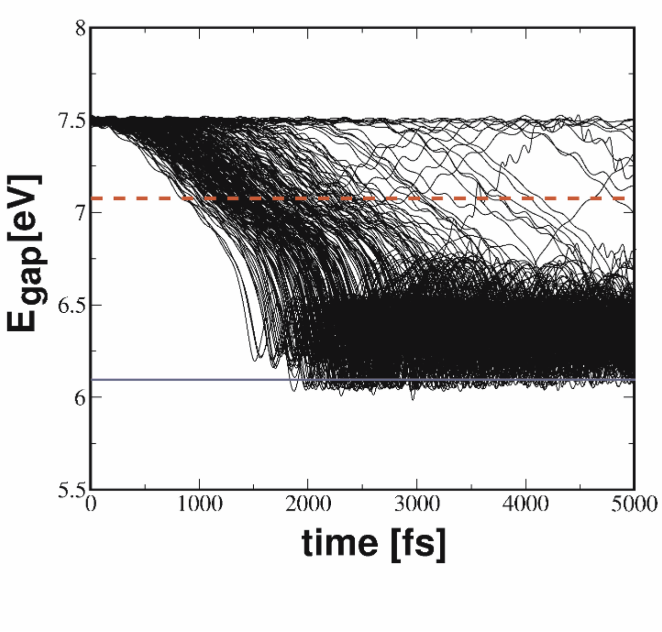

Fig. 2.15. Bunch of the cation-neutral energy gaps of Ag_2Au (right side). Energies of 7.09 eV (dashed line) and of 6.1 eV (full line) indicate the proximity of the Franck-Condon region and of the minimum of neutral species, respectively. They are used for simulating the signals.

and 7.5 eV probe the onset of the geometric relaxation processes. Therefore, it is expected that the signals exhibit maxima at delay times when the probe energy is resonant with energy gaps and decrease to zero at later times. Pulse energies below 6.5 eV probe the arrival and the dynamics at the triangular structure. It is to be expected that at ∼ 6.1 eV pulse energies, the signal will rise after ∼ 2 ps and remain constant at later times. This is illustrated also in Fig. 2.16a in which the theoretical NeNePo and NeNePo-ZEKE signals are compared with the experimental results at low temperature (T∼20K) for three energies: $E_{pr} = 7.7$ eV; probing above the ionization threshold of the linear structure, $E_{pr} = 7.10$ eV; probing the Franck-Condon region, and $E_{pr} = 6.10$ eV; probing the triangular geometry region corresponding to the minimum of the neutral Ag_2Au [68].

The NeNePo signal in the upper trace of Fig. 2.16 has been obtained with the probe energy $E_{pr2ph} = 7.7$ eV. The signal rises fast between about 700 fs and 1.5 ps and remains constant afterwards due to the contribution of the continuum. The middle trace of Fig. 2.16 shows the signal obtained with the probe pulse energy $E_{pr2ph}= 7.1$ eV. The Ag_2Au^+ ion intensity is minimal around zero time, but starts to rise already after about 500 fs with

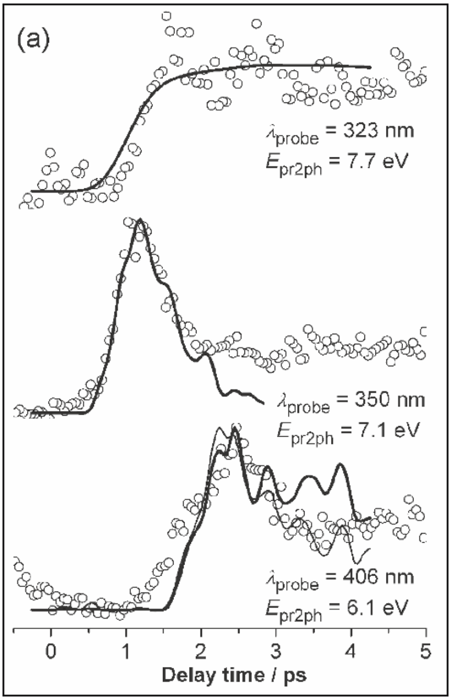

Fig. 2.16. Experimental NeNePo signals (open circles) obtained for three different probe pulse wavelengths in comparison with the simulated time dependent signals (solid lines) for the different probe pulse energies. The ionization probe step is two photonic as confirmed by power dependent measurements. The signals are normalized in intensity: lower graph: The experimental data obtained at $\lambda_{pr} = 406$ nm ($E_{pr2ph} = 6.1$ eV) are overlaid by the simulated NeNePo-ZEKE (bold line) and NeNePo (thin line) signals at $E_{pr} = 6.1$ eV, middle: experimental data obtained at $\lambda_{pr} = 350$ nm ($E_{pr2ph} = 7.1$ eV) are overlaid by the simulated NeNePo-ZEKE signal at $E_{pr} = 7.1$ eV, upper graph: the experimental data obtained at $\lambda_{pr} = 323$ nm ($E_{pr2ph} = 7.7$ eV) are overlaid by the simulated NeNePo signal at $E_{pr} = 7.41$ eV. A common time zero between experiment and theory has been chosen for all probe energies. The deviation in the time origin corresponds to less than 0.1 eV in the probe energy.

a considerably steeper slope than in Fig. 2.16 to reach a maximum already at 1.1 ps. The signal decreases again comparably fast and stays at a constant low level after 2 ps. The lower trace of Fig. 2.16 displays the NeNePo signal for 6.1 eV reached with two photon probe energy (E_{pr2ph}) measured at 20 K. The signal stays at the same low level for 1.1 ps, then rises gradually until it reaches its maximum value around 2.5 ps. It subsequently decreases again and remains almost constant at about half of its maximal intensity from 3.5 ps on.

The comparison between the theoretically obtained NeNePo signals (solid lines in Fig. 2.16) and the measured time dependent NeNePo signals enables the assignment of the observed pronounced probe energy dependence to the fundamental processes of nuclear dynamics. At $E_{pr2ph} = 6.1$ eV (Fig. 2.16 lower trace) the onset of IVR and the dynamics of Ag_2Au initiated by the collision of the terminal Au and Ag atoms can be probed exclusively. The good agreement between the experimental (open circles) and the simulated NeNePo-ZEKE signals (bold line) in Fig. 2.16 is apparent, indicating that the experimental signal starts to rise when the system approaches the triangular potential well. The signal maximum can be assigned to the time of intracluster collision at around 2.4 ps followed by IVR in the potential minimum of the neutral triangular geometry. The experimental signal offset at longer delay times is somewhat lower with respect to the maximum than expected from the simulated NeNePo-ZEKE signal. This might be attributed to contributions from the rather similar NeNePo type signal (thin line in the lower trace of Fig. 2.16). This shows explicitly in which regime ZEKE conditions hold in the experiment. The middle trace of Fig. 2.16 presents the comparison of simulated and experimental transient ion signals at 7.1 eV probe energy. Because the initial peak of the experimental transient is perfectly matched by the simulated NeNePo-ZEKE signal (solid line) at the corresponding wavelength the experimental conditions in this case allow for direct exclusive probing of the geometrical relaxation of Ag_2Au. The trimer passes through bending angles of $\phi = 166^o$ at the signal onset around 500 fs to $\phi = 13^o$ at the signal maximum and finally up to $\phi = 96^o$ at 2 ps, where the terminal atoms already interact and the intracluster collision is closely ahead (cf. upper trace of Fig. 2.17). The experimental signal offset at times later than 2 ps can again be attributed to the imperfect NeNePo-ZEKE conditions. The possible reason for the good agreement of the experimental transient signal with the simulated NeNePo-ZEKE transient signal is most likely due to a particularly favorable Franck-Condon overlap in the case of 7.1 eV two photon probe energy. Finally, at high ionization energy $E_{pr2ph} = 7.7$ eV, a comparably weak experimental transient signal is detected. This signal is in agreement with the simulated NeNePo transient (solid line) at a probe energy of 7.41 eV just below the highest theoretically predicted ionization energy which corresponds to the linear transition state structure (see top trace of Fig. 2.16). Thus, the experiment at $E_{pr2ph} = 7.7$ eV apparently monitors the system when it leaves this transition state region. Still there is a considerable signal onset time of about 700 fs which reflects the very shallow slope of the PES around the linear transition state geometry.

In summary, experiment and theory are in excellent agreement. The simulated signal at E_{pr}=7.70 eV rises after 1 ps and remains constant subsequently without allowing to identify the dynamical processes which take place due to the contribution of the continuum. The signals at $E_{pr} = 7.1$ eV reflect geometric relaxation from linear to triangular geometry of the neutral Ag_2Au. The signals at $E_{pr} = 6.10$ eV are due to IVR.

For an analysis of the vibrational energy redistribution, the kinetic energy was decomposed into normal mode contributions. Figure 2.17 shows a single-trajectory example together with the two distinct Ag-Ag-Au bond angles ϕ. From this representation, valuable insight into the IVR in this model system can be gained. The bond angle ϕ in Fig. 2.17 decreases from an initial value of about 180^o at t = 0 to a minimum value of 54^o at t = 2.36 ps. However, the kinetic energy begins to increase notably only at t$\sim$ 2.0 ps, when ϕ falls short of 90^o. Accordingly, within the next 360 fs ϕ decreases much more rapidly and the kinetic energy in the bending mode passes a pronounced maximum.

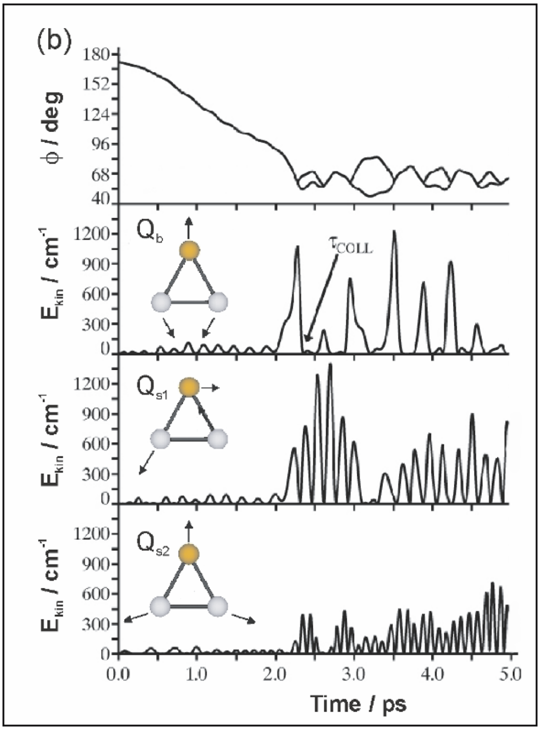

Fig. 2.17. A single-trajectory example of the evolution of the Ag-Ag-Au bond angle ϕ (upper panel) and of the kinetic energy in the three vibrational normal modes Q_b, Q_{s1}, and Q_{s2} (lower panels). In the upper panel two functions are given for ϕ, since for triangular geometries two Ag-Ag-Au bond angles can be defined. The lower curve for ϕ reflects the atom connectivities of the initial linear geometry and therefore monitors the geometrical relaxation until the closest approach of the terminal atoms (internal collision). The upper curve is the larger of the two Ag-Ag-Au bond angles and indicates partial escapes from the potential well of the triangular geometry. In the second panel from top, the collision time τ_{COLL} = 2.36 ps, determined from the first pronounced rise and the subsequent sharp minimum of the kinetic energy in the bending mode, is marked in the diagram.

Shortly afterwards, the kinetic energy decreases to zero, as the system passes the potential minimum and the terminal atoms subsequently further approach each other ("internal collision"), until the kinetic energy is consumed by running against the repulsive part of the potential. In parallel to the increase of the kinetic energy in the bending mode Q_b, intense oscillations are triggered in the first, antisymmetric stretching mode Q_{s1} and to a smaller extent only in the symmetric stretching mode Q_{s2}. Apparently, the simultaneous gain of kinetic energy of the Q_b and of the Q_{s1} mode is a consequence of the fact that both normal coordinates together make up the major components of the linear-to-triangular geometric relaxation coordinate.

Intense kinetic energy oscillations of the stretching modes appear between two pronounced kinetic energy maxima of the bending mode, when the system is in the deep region of the potential, so that enough energy is available for the stretching modes. This relation is particularly apparent for the antisymmetric stretching mode Q_{s1}, manifesting an extensive energy exchange and a close coupling of these modes. Shortly after the bending mode has passed its maximum kinetic energy, its kinetic energy drops to zero (manifesting internal collision), which for the single trajectory of Fig. 2.17 occurs at 2.36 ps. Since the other mode energies increase at the same time, IVR is manifested; the drop of the kinetic energy in the bending mode cannot be solely explained by a conversion of kinetic to potential energy in the bending mode. This behavior is also found for other trajectories, whereupon one can generally state that notable IVR sets in at the instant of internal collision.

These results imply that the nature of IVR in Ag_2Au is related to the one found for Ag_3 (cf. [31, 40]). However, two important aspects should be emphasized. First, time scales are much longer than in the case of Ag_3, due to the heavy atom effect. Second, importantly, in contrast to the Ag_3, the experimental results for Ag_2Au reveal for the first time geometric relaxation separated from an IVR process, indicating that the experimental signals are close to the ZEKE-like conditions, which has been proposed by theory as a necessary condition for the separation of time scales of these processes [68].

2.3.1.5 Vibrating rhombus of Ag_4

In order to further illustrate the ability of the theoretical approach to treat systems with more degrees of freedom, one example, Ag_4, has been chosen for the presentation. In the case of the silver tetramer, the global minima of the anion and of the neutral cluster assume related rhombic structures. Therefore, after photodetachment at low temperatures ($T \approx 50$ K), which assures that only the rhombic isomer is populated, the nonequilibrium rhombic configuration close to the global minimum of the neutral species is reached, as shown on the left hand side of Fig. 2.18.

The probe in the Franck-Condon region with $E_{pr} = 6.41$ eV reveals the vibrational structure of the rhombic configuration after photodetachment. For the probe with, e. g. $E_{pr} = 6.46$ eV, the dynamics in the vicinity of the neutral

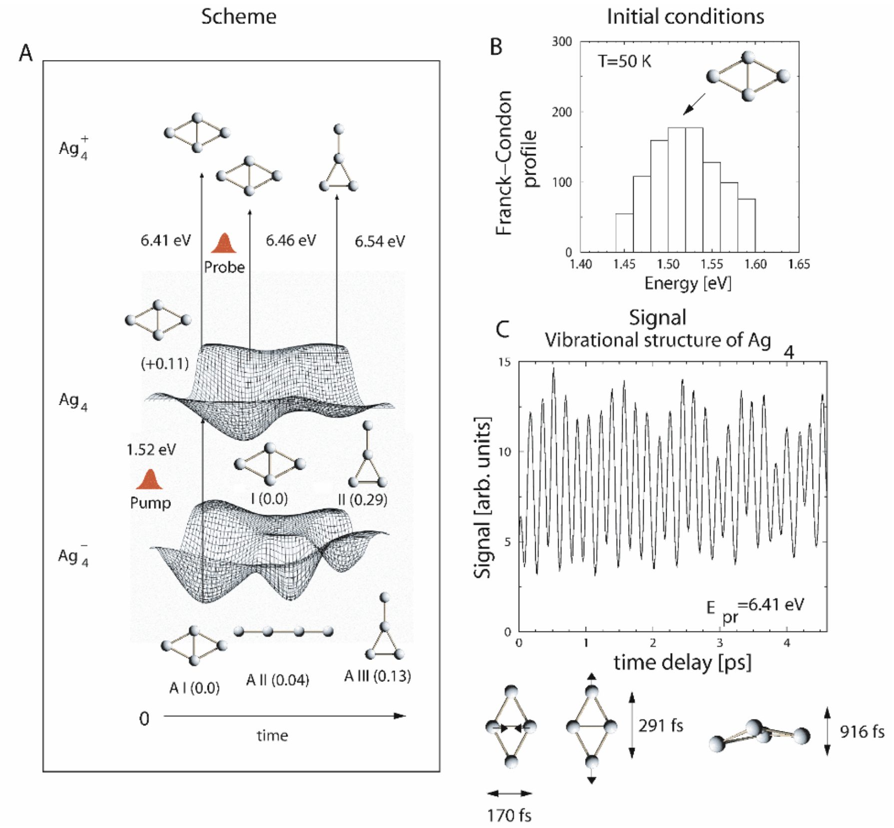

Fig. 2.18. Scheme of multistate fs-dynamics for NeNePo pump-probe spectroscopy of $Ag_4^-/Ag_4/Ag_4^+$ with structures and energy intervals for the pump and probe steps (A). Simulated NeNePo-ZEKE signals for the 50 K initial condition ensemble (B) at the probe energy of 6.41 eV and a pulse duration of 50 fs (C). Normal modes responsible for relaxation leading to oscillatory behavior of the signal are also shown [67].

rhombic structure can be monitored. The simulated NeNePo-ZEKE signal at 6.41 eV for a probe duration of 50 fs shown in Fig. 2.18 exhibits oscillations with a vibrational period of $\sim$ 175 fs which is close to the frequency of the short diagonal stretching mode, indicating the occurrence of the geometric relaxation along this mode toward the global minimum. The analysis of the signal also reveals contributions from two other modes shown in Fig. 2.18. In summary, this example illustrates that an identification of the structure of a gas-phase neutral cluster in experimental NeNePo signals is possible due to its vibronic resolution [67]. The theoretically predicted main features of the pump-probe signals for Ag_4 have been also found experimentally.

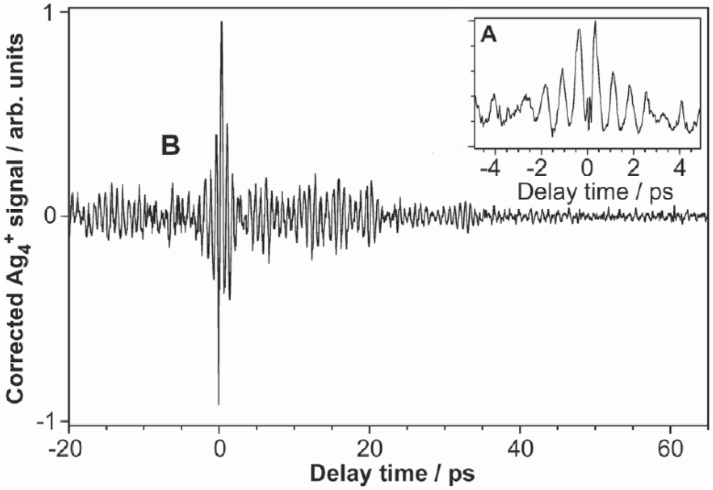

Fig. 2.19. NeNePo spectrum of Ag_4 recorded in a one-color experiment (385 nm) at 20 K ion temperature. Trace A (insert) shows the uncorrected, mass selected Ag_4^+ yield. Trace B is a composite of two measurements and the signal has been corrected for the FFT analysis. Figure taken from [108].

One-color NeNePo-spectra of Ag_4^- measured at 385 nm and an anion temperature of 20 K are shown in Fig. 2.19. [108] Trace A (top right) shows the (uncorrected) mass selected Ag_4^+ yield as function of the delay time between the pump and probe pulses from -4.9 ps to +4.9 ps in steps of 20 fs and exhibits a pronounced oscillatory structure, characterized by a period of about 740 fs. The intensity of the maxima decreases for larger delay times and additional, weaker structures are observed at delay times > 2.8 ps overlapping the 740 fs beat structure.

Trace B in Fig. 2.19 is a composite of two measurements covering delay times from -20 ps to +20 ps and +20 ps to +65 ps. The spectra have been baseline corrected and transformed for the following fast Fourier transform (FFT). Trace B shows that the oscillations in the Ag_4^+ signal intensity extend up to 60 ps, with decreasing intensity. Pronounced partial recurrences are observed. The FFT analysis of this time-resolved signal reveals as dominant feature several peaks centered around 45 cm^{-1} [108]. Comparison to photoelectron data of Ag_4^- [62] leads to the conclusion that the oscillations observed in the NeNePo spectra of Ag_4 are due to vibrational wave packet dynamics in the $2a_g$ mode of either the $^3B_{1g}$ or $^1B_{1g}$ “dark” electronically excited state of rhombic Ag_4 which is probed by a two photon ionization step to Ag_4^+. Ab initio calculations of the harmonic frequencies of the low-lying electronic states of rhombic Ag_4 support this assignment and confirm the observed pronounced anharmonicity of this vibrational mode of $2\nu_0\chi_0 = 2.65 \pm 0.05$ cm^{-1}. The $2a_g$ mode was not resolved in the previous anion photoelectron spectroscopy studies, due to its low frequency of 45 cm^{-1} which lies below the resolution of conventional anion photoelectron spectrometers. The results on Ag_4 demonstrate the successful application of femtosecond NeNePo spectroscopy to study the wave packet dynamics in real time. This is manifested by a beat structure in the cation yield, of a "purely" bound potential, in contrast to the transition-state experiments on the noble metal trimers which connect linear with triangular structures. The spectra of Ag_4 enable the characterization of a selected vibrational mode with a resolution, which is superior to that of conventional frequency domain techniques.

2.3.1.6 Reactivity aspects elucidated by the fragmentation of Ag_2O_2 and isomerization in Ag_3O_2

Noble metal clusters exhibit fascinating reactive properties such as strongly size and charge dependent reactivity toward small molecules, e. g. O_2 [110]. One particularly appealing example in this respect is the reactive behavior of the silver dimer toward dioxygen in the gas phase which has been investigated in detail by different groups [83, 94, 111–116]. Under the conditions of an rf-ion trap experiment, the anionic dimer adsorbs one O_2 molecule in a straightforward association reaction mechanism [83]. Photoelectron spectroscopic studies confirm that the oxygen is molecularly bound to Ag_2^- [116]. In contrast to Ag_2^-, the positively charged silver dimer shows a strongly temperature dependent O_2 adsorption behavior: O_2 is first adsorbed molecularly on Ag_2^+, but in an activated reaction step, the O-O bond can dissociate leading to the adsorption of atomic oxygen at temperatures above 90 K [112]. A NeNePo experiment starting from the stable $Ag_2O_2^-$ complex is thus expected to probe the real-time nuclear dynamics associated with the change in the reactive O_2 adsorption behavior initiated by the pump-photodetachment step. Figure 2.20a displays the experimental NeNePo spectrum of the bare silver dimer without adsorbed oxygen obtained in a one-color pump-probe experiment (406 nm) at 100 K anion temperature. The NeNePo trace exhibits two remarkable features: (i) A pronounced maximum in the recorded Ag_2^+ signal at 190 fs pump-probe delay time and (ii) distinct vibrational dynamics at longer delay times (>400 fs). The amplitude of the vibrational structure at delay times >400 fs is about ten times smaller than the maximum signal. The vibrational period of the observed signal oscillation was determined by FFT analysis to be 180 ± 1 fs ($\nu = 185 \pm 1$ cm^{-1}). The femtosecond NeNePo dynamics detected in the Ag_2^+ signal in Fig. 2.20a can be understood on the basis of the known spectroscopic properties of Ag_2^- and Ag_2 [97] (cf. Fig. 2.21 a and b). Through photodetachment with 406 nm (3 eV) photons, the electronic ground state of Ag_2 (X-$1^1\Sigma_g$) is populated, but also the lowest excited triplet state $1^3\varSigma_u$. This latter triplet state is, however, only very weakly bound (Fig. 2.21a). The system is thus populated in the repulsive part of the potential energy curve in the dissociation continuum of this state. During the propagation along the triplet potential curve, the wave packet might

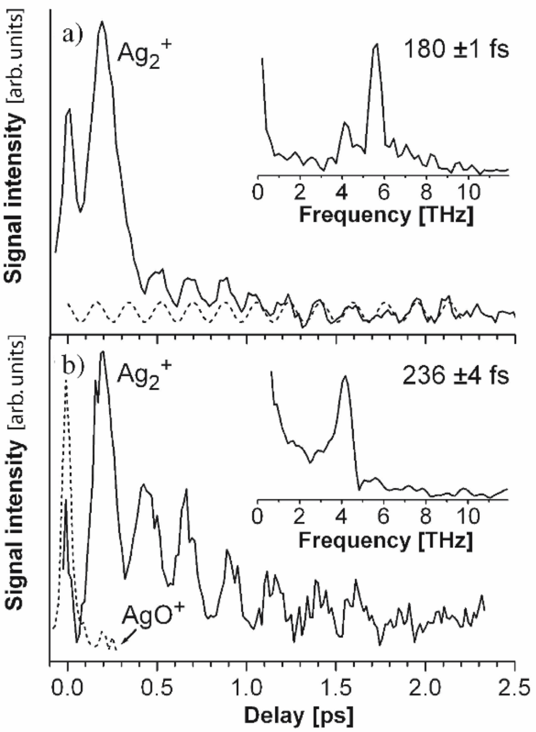

Fig. 2.20. (a) NeNePo spectrum of Ag_2 recorded in a one-color experiment (406 nm) at 100 K ion temperature. (b) Pump-probe spectra of the NeNePo fragment signals Ag_2^+ (solid line) and AgO^+ (dashed line, magnified by a factor of 10) resulting from neutral Ag_2O_2 dissociation after photodetachment of $Ag_2O_2^-$ (406 nm, 100 K).

be transferred via resonant two photon transitions at two close lying locations to the cationic state for detection (via C-$2^3\Pi_u$ and B-$1^1\Pi_u$-states of Ag_2). The existence of these resonances explains the strong enhancement of the Ag_2^+ signal at 190 fs delay time. The lack of a periodical revival with comparable amplitude confirms the assumption that the wave packet further propagates freely to the dissociation on the triplet state potential. The wave packet at the same time prepared on the X-$1^1\Sigma_g$ ground state of Ag_2 oscillates between the inner and outer turning point of the potential leading to the observed periodic signal at delay times >400 fs with 180 fs oscillation period (2.21b). The localization of the wave packet is highest at the turning points of the potential where it can be efficiently transferred into the ground state of Ag_2^+ by irradiation with the probe pulse. The ionization step requires three 406 nm photons, where a resonant transition via the A-$1^1\Sigma_u$-state is possible [117].

If a small partial pressure of O_2 is added to the helium buffer gas inside the rf-ion trap, the complex $Ag_2O_2^-$ is immediately formed, before the silver dimer

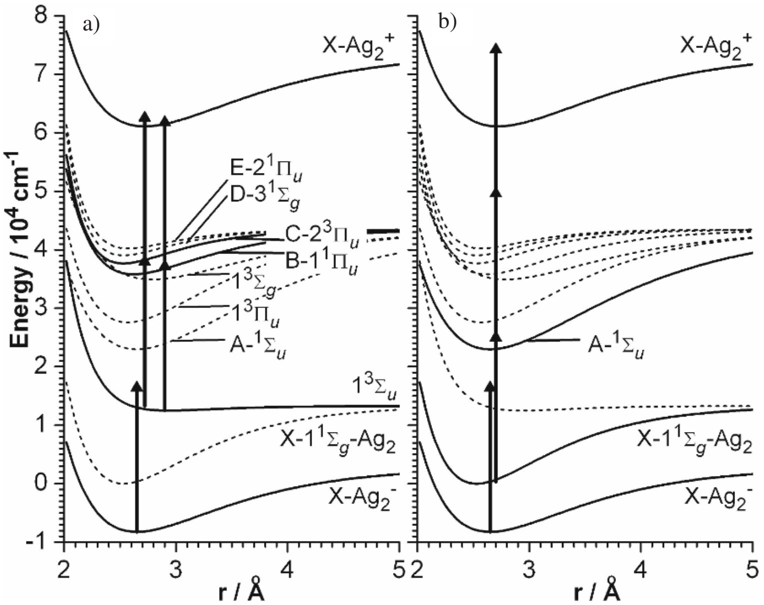

Fig. 2.21. Potential energy curves for the NeNePo process of Ag_2 in the triplet state (a) and the neutral singlet ground state (b).

can interact with the femtosecond laser pulses [83]. Thus, under these conditions, the NeNePo experiment exclusively probes the dynamics launched by photodetachment from the $Ag_2O_2^-$ cluster complex. Figure 2.20b shows the result of the NeNePo experiment starting form $Ag_2O_2^-$ performed under otherwise identical conditions as in the case of Ag_2^- (Fig. 2.19a). It is first interesting to note that at zero delay a signal of $Ag_2O_2^+$ was detected resulting from the NeNePo process. This indicates that the neutral Ag_2O_2 formed by photodetachment is unstable and rapidly dissociates. The observation is in accordance with gas-phase reactivity measurements which show that the neutral complex Ag_2O_2 is not bound [111]. Surprisingly, two fragmentation paths which lead to the formation of the product ions Ag_2^+ and AgO^+ (solid and dashed lines in Fig. 7b, respectively) seem to exist. The Ag_2^+ signal is a factor of ten larger than the AgO^+ signal. The AgO^+ signal exhibits only a peak at zero delay time with a width corresponding to the cross correlation of the laser pulses (80 fs). This suggests that Ag_2O_2 decays on a short time scale of less than 80 fs to fragments. Most likely, AgO^+ arises from fragmentation in the cationic state, i.e. by decay of $Ag_2O_2^+$, which is generated by vertical multi photon transition from $Ag_2O_2^-$ in the interference (cross correlation) time range of the two laser pulses of the same color. The much more intense Ag_2^+ signal shows pronounced oscillatory dynamics, which differs significantly from bare Ag_2 (cf. Fig. 2.20a). First, the amplitude of the observed vibrations is much larger than that of the long delay time dynamics of pure Ag_2. Second, the oscillation is damped, and third, the NeNePo spectra do not show the short time scale dynamics as it appears for bare Ag_2 in Fig. 2.20a. The FFT-analysis of the oscillatory dynamics in Fig. 2.20b leads to a vibrational period of 236 ± 4 fs ($\nu = 141 \pm 3$ cm^{-1}) which is significantly red-shifted in comparison to the 180 fs period of bare Ag_2. The red shift of the vibration points toward the substantial influence of the fragmentation of the oxygen ligand on the dynamics. Qualitatively, the fragmentation of the O_2 molecule apparently leaves the silver dimer fragment with higher vibrational levels populated. An estimation based on known spectroscopic constants of Ag_2 and the Morse approximation gives a vibrational excitation up to levels around v=40 for ν=141 cm^{-1}, which means a vibrational energy gain of approximately 0.7 eV compared to the bare Ag_2 prepared by the photodetachment from Ag_2^-. Due to the substantial anharmonicity of the potential in this frequency region, the wave packet experiences a rapid dephasing after only a few vibrational periods as can be seen from Fig. 2.20b. The amplitude of the vibration in Fig. 2.20b can be fitted in good approximation by an exponentially damped sine function with a lifetime of 650 ± 50 fs, which gives an approximate time scale for the dephasing of the wave packet [117]. This observation reflects the strong influence of the molecular adsorbate on the metal cluster structure. Such adsorbate induced structural changes, geometric as well as electronic, have recently been identified as the origin for the cooperative adsorption of multiple adsorbate molecules on small noble metal clusters. This cooperative action is regarded essential for the catalytic activity of gas-phase noble metal clusters in, e.g., the CO combustion reaction [83, 115]. In the particular case of negatively charged silver clusters Ag_n^- with an odd n, the joint experimental and theoretical work showed that a weakly bound first O_2 cooperatively promotes the adsorption of a second O_2 molecule, which is then differently bound with the O_2 bond elongated and thus activated for further oxidation reactions such as CO combustion [83]. The possible prospects of these intriguing catalytic properties of free noble metal clusters for real time laser spectroscopic investigations and photon-induced control of catalytic reactions will be illustrated for the prototype example of Ag_3O_2.

The scheme of the multistate dynamics for Ag_3O_2 is presented in Fig. 2.22a. Anionic isomers in which the isomer I has a linear Ag_3 subunit, and the isomer II a triangular Ag_3 subunit, are very close in energy and the exact energy sequence is difficult to predict theoretically, even when highly accurate methods are applied. However, due to the pronounced differences in vertical detachment energies (VDE) of both isomers, they can be selected by appropriate choice of the pump-pulse energy. It is assumed that only isomer I is populated in the anionic ground state and a canonical Wigner distribution function given in (2.7) at T=20 K is used to generate the initial conditions. After the photodetachment with the pump-pulse energy of 2.75 eV a transition state in neutral Ag_3O_2 is reached. Three isomers are present for Ag_3O_2 as shown in Fig. 2.22. In the structure of the global minimum (isomer I),

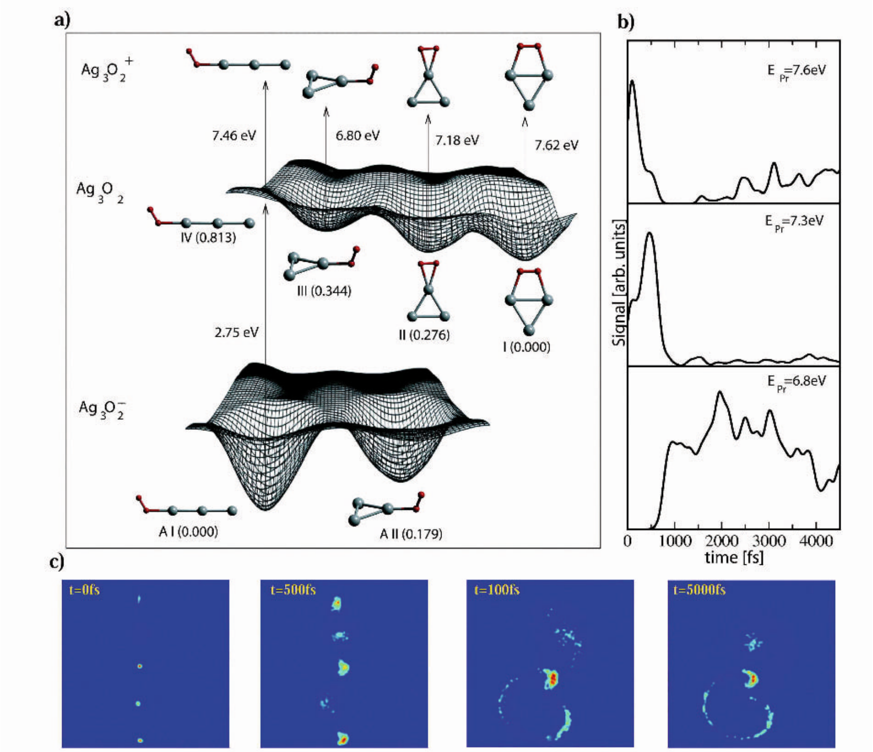

Fig. 2.22. Scheme of the multistate fs-dynamics for NeNePo pump-probe spectroscopy of $Ag_3O_2^-/Ag_3O_2/Ag_3O_2^+$ with structures and energy intervals for pump and probe steps. (b) Simulated NeNePo-ZEKE pump-probe spectra, (c) snapshots of the dynamics in the neutral Ag_3O_2 after the photodetachment.

the molecular oxygen bridges two silver atoms (cf. Fig. 2.22a). In the two higher lying isomers, molecular oxygen is bound to one silver atom, forming one and two bonds, respectively. Therefore, after the photodetachment a dynamical process dominated by the Ag_3 relaxation from the linear to the triangular structure is induced. At later times the energy gained by the cluster isomerization is partly transferred to molecular oxygen leading mainly to the mixture of two higher lying isomers (II and III). After 5 ps the global minimum (isomer I) is populated only by about 10%. Therefore, in principle the population of the chosen minimum with its corresponding reactive center can be controlled with a tailored laser field. The snapshots of the dynamics in the neutral state are presented in Fig. 2.22c; they show the onset of the geometric relaxation of the Ag_3 subunit at 500 fs, the arrival to the triangular Ag_3 subunit at 1 ps, and the final ensemble of isomers after 5 ps. The simulated NeNePO-ZEKE pump-probe signals for Ag_3O_2 are presented in Fig. 2.22b. The signal for the probe pulse energy of 7.6 eV exhibits a fast decay after 1 ps due to the escape from the initial Franck-Condon region reached upon the photodetachment. However, this signal starts to rise again after 2 ps since the global minimum with the ionization potential of 7.62 eV is being populated at later times. This signal offers an opportunity to identify the isomerization process leading to the global minimum in the ground state and also to determine its time scale. If the energy of the probe pulse is lowered to 7.3 eV the onset of isomerization of the Ag_3 subunit starting at 500 fs can be selectively probed. Further lowering of the energy to 6.8 eV allows to probe the IVR process induced after the intracluster collision within the Ag_3 subunit. It should be pointed out that in contrast to the Ag_2Au, here the IVR process is extended also to the O_2 subunit. It is responsible for the final populations of the isomers, since they mainly differ by the bonding of the O_2 subunit. In general, it can be expected that future studies of the dynamics of reactive complexes between metal clusters and small molecules may shed a new light on the influence of the dynamics and particularly IVR on their reactive (catalytic) properties.

2.3.1.7 The scope of NeNePo spectroscopy

Finally, the question can be raised: what general information can be inferred from simulated NeNePo-ZEKE signals on the multistate energy landscapes and dynamics? First, the theoretical simulations allowed to establish the connections between three objectives: the structural relation of anionic and neutral species, the influence of the nature of the nonequilibrium state reached after photodetachment, and the character of subsequent dynamics in the neutral ground state [44]. Three different situations can be encountered in which i) transition state ii) global minimum and iii) local minimum can influence the dynamics after photodetachment. Second, different types of relaxation dynamics can be identified in NeNePo-ZEKE signals. Moreover, iv) the fragmentation and signature of fragments can be also identified and v) different nature of IVR, dissipative versus resonant can be used to characterize the catalytic capability of cluster species and to use NeNePo technique for verifying these important properties.

i) In cases where the anionic structure is close to a transition state of the neutral electronic ground state (e.g. trimers), large amplitude motion toward the stable structure dominates the relaxation dynamics. In other words, the dynamics is incoherent but localized in phase space. IVR can be initiated as a consequence of the localized large amplitude motion. Large amplitude structural relaxation after the transition state is responsible for a pronounced single peak in NeNePo-ZEKE signals at a given time delay and probe excitation wavelengths. In addition, subsequent IVR processes can be identified but only under ZEKE-like conditions since the integration over the continuum of electron kinetic energies leads to the loss of the fine features in the signals.

ii) In cases where the anionic structure is close to the global minimum (i. e. the stable isomer) of the neutral electronic ground state, vibrational relaxation reflecting the structural properties of the neutral stable isomer (e.g. Ag_4) takes place. The dynamics can be dominated by a single (e.g. Ag_4) or only by few modes which are given by the geometric deviations between anionic and neutral species. Other modes and anharmonicities weakly contribute, leading to dephasing on a timescale up to several ps (longer than 2 ps for Ag_4). Vibrational relaxation gives rise to oscillations in NeNePo signals (for different pulse durations) which can be analyzed in terms of normal modes. This allows to gain indirect information about vibrational spectra of a neutral cluster and use them as a fingerprint for identification of their structure.

iii) In cases where the anionic structure (the initial state) is close to a local minimum (energetically high lying isomer) of the neutral electronic ground state, the local minimum governs the dynamics after the photodetachment. Vibrational relaxation within the local minimum is likely to dominate the ultrashort dynamics.

Moreover, the local minimum can act as a strong capture area for nuclear motion with timescales up to several ps. As a consequence, isomerization processes toward other local minima and/or toward the global minimum structure are widely spread in time. In other words, structural relaxation dynamics is characterized as being incoherent and delocalized in phase space. The signals exhibit (at different excitation wavelengths of the probe laser) fingerprints of vibrational relaxation within the local minimum, providing structural information. After the systems escape from the local minima, the beginning of structural relaxation can be identified by an onset of signals appearing at the probe wavelengths ($\approx$1 ps for $Ag_3O_2^-$).

iv) The fragmentation patterns as well as the characteristics of fragments can also be identified in NeNePo signals. So, connected with the optimal control schemes the NeNePo technique provides a promising technique to introduce the control of the chemical reactivity, such as for the example of the oxidation of CO by noble metal oxide clusters, which is of relevance for heterogeneous catalysis. Moreover, the identification of IVR in the framework of the NeNePo technique represents a powerful tool which has a significant impact on the investigation of reactivity and catalysis.

2.4 Optimal control of dynamical processes

A. Lindinger, V. Bonačić-Koutecký, R. Mitrić, V. Engel, D. Tannor, A. Mirabal, and L. Wöste

2.4.1 General control concepts

The control of the selective product formation in a chemical reaction, using ultrashort pulses by choosing proper time duration and delay between the pump and the probe (or dump) step or their phase, is based on the coherence properties of laser radiation [10,11,13,14,118–121]. First, single-parameter control-schemes were proposed and tested. The scheme, introduced by Tannor and Rice [11,118] uses the time parameter for control, taking the advantage of differences in potential energy surfaces of different electronic states. Within the Brumer-Shapiro phase-control scheme [13, 14, 119], constructive and destructive interference between different light induced reaction pathways is used in order to favor or to suppress different reaction channels. Single parameter control schemes like linear chirps [122,123] corresponding to a decrease or increase of the frequency as a function of time under the pulse envelope were confirmed experimentally [124–135]. They represented the first step toward shaping the pulses in the framework of the optimal control theory (OCT) which involves many parameters. Variational optimization in the weak electric field limit was first introduced by Tannor and Rice [136]. Variational optimization with applications to arbitrary i.e. weak or strong fields was introduced by Rabitz et al. [12, 20, 21, 137], with important extensions by Kosloff et al. [17], Jakubetz et al. [121], and Rice et al. [16].

A related approach, that has grown in popularity recently, is known as 'local optimization'. [138–149]. The control method known as "tracking" is closely related [147]. In these methods, at every instant in time the control field is chosen to achieve a monotonic increase in the desired objective (see Fig. 2.28b). Typically in these methods, two conditions are used at each time step: one to determine the phase of the field and one to determine the amplitude. In contrast with OCT, which incorporates information on later time dynamics through forward-backward iteration, these methods use only information on the current state of the system. The examples of local control theory will be presented in Sect. 2.4.2.

Technological progress due to fs pulse shapers [150–154] lead to the closed loop learning control (CLL) which was introduced by Judson and Rabitz in 1992 [22] opening the possibility to apply optimal control to more complex systems. Since the potential energy surfaces (PES) of multidimensional systems are complicated and mostly not available. The idea is to combine a fs-laser system with a computer-controlled pulse shaper to produce and optimize specific fields acting on the system initiating a photochemical process. After detecting the product, the learning algorithm [150, 155, 156] modifies the field based on information obtained from the experiment and from the objective (the target). The optimal shape for the chosen target is then reached iteratively. Judson and Rabitz's CLL approach initiated flourishing of the field and the success has been demonstrated by numerous control experiments [151–154, 157–175]. However any multiparameter optimization scheme has a manifold of local solutions which are reachable depending on initial conditions. Particularly in the case of closed-loop learning control research activities are directed toward improvements of these aspects [176, 177].

Metallic dimers [177–185] and diatomic molecules [186, 187] have been studied in numerous contributions, since they were suitable model systems for verifying the scopes of different control schemes and they are accessible by experimental pulse shaping techniques [46, 162, 164–166, 188–193]. Theoretical and experimental studies using two parameter control have been performed: In addition to the pump-probe time delay the second control parameter involved the pump [178, 188, 189] and/or probe [179, 182] wavelength, the pump-dump delay [180, 190, 191], the laser power [181], the chirp [183, 192] or temporal width of the laser pulse [184]. Optimal pump-dump control of K_2 has been carried out theoretically in order to maximize the population of certain vibrational levels of the ground electronic state using one electronic excited state as an intermediate pathway [177, 185–187].

2.4.1.1 Pump-dump scheme

In order to tackle the very elementary chemical process of branching reaction channels, the ground electronic state potential energy surface in Fig. 2.23 can be considered. This potential energy surface, corresponding to collinear ABC, has a region of stable ABC and two exit channels, one corresponding to A+BC and one to AB+C. This system is the simplest paradigm for a control of chemical product formation: a two degree of freedom system is the minimum that can display two distinct chemical products. The objective is, starting out in a well defined initial state (v=0 of the ABC molecule) to design an electric field as a function of time which will steer the wave packet out of channel 1, with no amplitude going out of channel 2, and vice versa [11, 136].

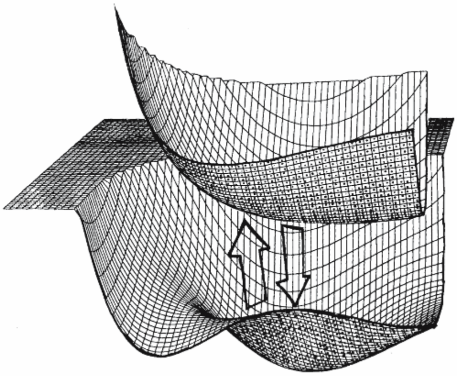

Fig. 2.23. Stereoscopic view of the ground and excited state potential energy surfaces for a model collinear ABC system with the masses of HHD. The ground state surface has a minimum, corresponding to the stable ABC molecule. This minimum is separated by saddle points from two distinct exit channels, one leading to AB+C the other to A+BC. The object is to use optical excitation and stimulated emission between the two surfaces to 'steer' the wave packet selectively out one of the exit channels.

A single excited electronic state surface is introduced at this point. The motivation is severalfold: 1) transition dipole moments are generally much stronger than permanent dipole moments. 2) the difference in functional form of the excited and ground potential energy surface will be the dynamical kernel; with a single surface one must make use of the (generally weak) coordinate dependence of the dipole. Moreover, the use of excited electronic states facilitates large changes in force on the molecule, effectively instantaneously, without necessarily using strong fields. 3) the technology for amplitude and phase control of optical pulses is significantly ahead of the corresponding technology in the infrared.

The object now will be to steer the wave function out of a specific exit channel on the ground electronic state, using the excited electronic state as an intermediate. Insofar as the control is achieved by transferring amplitude between two electronic states, all the concepts regarding the central quantity μ_{eg} will now come into play.

Consider the following intuitive scheme, in which the timing between a pair of pulses is used to control the identity of products [11]. The scheme is based on the close correspondence between the center of a wave packet in time and that of a classical trajectory (Ehrenfest's theorem). The first pulse produces an excited electronic state wave packet; the time delay between the pulses controls the time that the wave packet evolves on the excited electronic state. The second pulse stimulates emission. By the Franck-Condon principle, the second step prepares a wave packet on the ground electronic state with the same position and momentum, instantaneously, as the excited state wave packet. By controlling the position and momentum of the wave packet produced on the ground state through the second step, one can gain some measure of control over product formation on the ground state. This 'pump-dump' scheme is illustrated classically in Fig. 2.24. The trajectory originates at the ground state surface minimum (the equilibrium geometry). At $t = 0$ it is promoted to the on the excited state potential surface (a two dimensional harmonic oscillator in this model) where it originates at the Condon point, i.e. vertically above the ground state minimum. Since this position is displaced from equilibrium on the excited state, the trajectory begins to evolve, executing a two-dimensional Lissajous motion. After some time delay, the trajectory is brought down vertically to the ground state (keeping both the instantaneous position and momentum it had on the excited state) and allowed to continue to evolve on the ground state. Figure 2.24 shows that for one choice of time delay it will exit into channel 1, for a second choice of time delay it will exit into channel 2. Note how the position and momentum of the trajectory on the ground state, immediately after it comes down from the excited state, are both consistent with the values it had when it left the excited state, and at the same time are ideally suited for exiting out their respective channels.

A full quantum mechanical calculation based on these classical ideas is shown in Figs. 2.25-2.26 [136]. The dynamics of the two-electronic state model, was solved, starting in the lowest vibrational eigenstate of the ground elec-

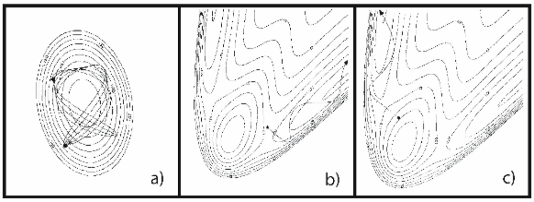

Fig. 2.24. Equipotential contour plots of the ground and the excited state potential energy surfaces (here a harmonic excited state is used because that is the way the first calculations were done). a) The classical trajectory that originates from rest on the ground state surface makes a vertical transition to the excited state, and subsequently undergoes Lissajous motion, which is shown superimposed. b) Assuming a vertical transition down at time t_1 (position and momentum conserved) the trajectory continues to evolve on the ground state surface and exits from channel 1. c) If the transition down is at time t_2 the classical trajectory exits from channel 2.

tronic state, in the presence of a pair of femtosecond pulses that couple the states. Because the pulses were taken to be much shorter than a vibrational period, the effect of the pulses is prepare a wave packet on the excited/ground state which is almost an exact replica of the instantaneous wave function on the other surface. Thus, the first pulse prepares an initial wave packet which is almost a perfect Gaussian, and which begins to evolve on the excited state surface. The second pulse transfers the instantaneous wave packet at the arrival time of the pulse back to the ground state, where it continues to evolve on the ground state surface, given its position and momentum at the time of arrival from the excited state. For one choice of time delay the exit out of channel 1 is almost completely selective (Fig. 2.25), while for a second choice of time delay the exit out of channel 2 is almost completely selective (Fig. 2.26). Note the close correspondence with the classical model: the wave packet on the excited state is executing a Lissajous motion almost identical with that of the classical trajectory (the wave packet is a nearly Gaussian wave packet on a two-dimensional harmonic oscillator). On the ground state, the wave packet becomes spatially extended but its exit channel, as well as the partitioning of energy into translation and vibration (i.e. parallel and perpendicular to the exit direction) are seen to be in close agreement with the corresponding classical trajectory.

This scheme is significant for three reasons: it shows that control is possible, it gives a starting point for the design of optimal pulse shapes; and it gives a framework for interpreting the action of two pulse and more complicated pulse sequences. Nevertheless, the approach is limited: in general with the best choice of time delay and central frequency of the pulses one may achieve only partial selectivity. Perhaps most importantly, this scheme does not exploit the phase of the light. Intuition breaks down for more complicated processes and

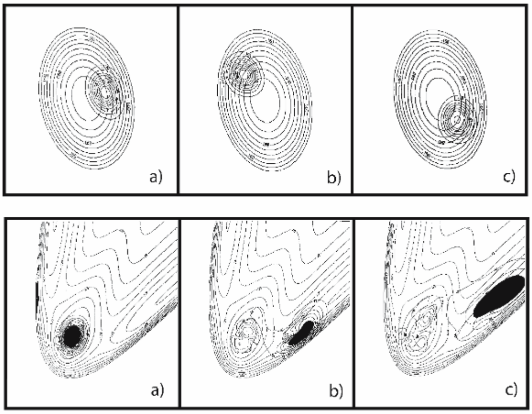

Fig. 2.25. Top: Magnitude of the excited state wave function for a pulse sequence of two Gaussians with time delay of 610 a.u.=15 fs. a) t=200 a.u., b) t=400 a.u., c) t=600 a.u. Note the close correspondence with the results obtained for the classical trajectory (Fig. 2.25). Bottom: Magnitude of the ground state wave function for the same pulse sequence, at a) t=0, b) t=800 a.u., c) t=1000 a.u. Note the close correspondence with the classical trajectory of Fig. 2.24b). Although some of the amplitude remains in the bound region, which does exit exclusively from channel 1.

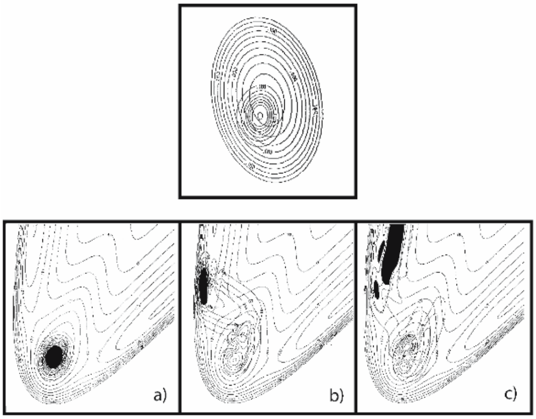

Fig. 2.26. Magnitude of the ground and excited state wave functions for a sequence of two Gaussian pulses with time delay of 810 a.u. Top: excited state wave function at 800 a.u., before the second pulse. Bottom: a) ground state wave function at 0 a.u. b) ground state wave function at 1000 a.u. c) ground state wave function at 1200 a.u. That amplitude which does exit does so exclusively from channel 2. Note the close correspondence with the classical trajectory of Fig. 2.24c.

classical pictures cannot adequately describe the role of the phase of the light and the wave function. Hence attempts were made to develop a systematic procedure for improving an initial pulse sequence.

Before turning to these more systematic procedures for designing shaped pulses, an interesting alternative perspective on pump-dump control will be pointed out. A central tenet of Feynman's approach to quantum mechanics was to think of quantum interference as arising from multiple dynamical paths that lead to the same final state. The simple example of this interference involves an initial state, two intermediate states, and a single final state, although if the objective is to control some branching ratio at the final energy then at least two final states are necessary. By controlling the phase with which each of the two intermediate states contributes to the final state, one may control constructive vs. destructive interference in the final states. This is the basis of the Brumer-Shapiro approach to coherent control [24]. It is interesting to note that pump-dump control can be viewed entirely from this perspective [24]. Now, however, instead of two intermediate states there are many, corresponding to the vibrational levels of the excited electronic state. The control of the phase which determines how each of these intermediate levels contributes to the final state, is achieved via the time delay between the excitation and the stimulated emission pulse. This "interfering pathways" interpretation of pump-dump control is shown in Fig. 2.27.

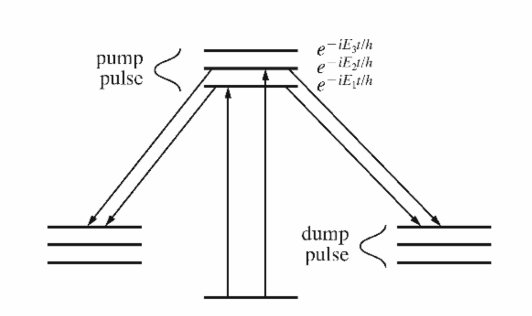

Fig. 2.27. Multiple pathway interference interpretation of pump-dump control. Since each of the pair of pulses contains many frequency components, there are an infinite number of combination frequencies which lead to the same final energy state, which generally interfere. The time delay between the pump and dump pulses controls the relative phase among these pathways, and hence determines whether the interference is constructive or destructive. The frequency domain interpretation highlights two important features of coherent control: First, if final products are to be controlled there must be degeneracy in the dissociative continuum. Second, that a single interaction with the light, no matter how it is shaped, cannot produce control of final products: at least two interactions with the field are needed to obtain interfering pathways.

2.4.1.2 Variational formulation of control

In the following a brief outline of theoretical and experimental approaches will be given. In OCT the optimized pulses are obtained from the functional in the framework of the variational method [12, 17]:

$$J = \langle \psi(T) | \hat{P} | \psi(T) \rangle. \tag{2.13}$$

J is the functional of the radiation field $E(t)$. Therefore, the maximization has to be carried out with respect to the variation of the functional form of $E(t)$ which involves temporal shape and spectral content. $\hat{P}$ is the projector operator which selects the desired target.

A constraint which the energy per pulse is given by

$$E = \int_0^T dt |E(t)|^2, \tag{2.14}$$

which, together with (2.13) implies that the following functional must be optimized:

$$J_\alpha = \langle \psi(T) | \hat{P}_\alpha | \psi(T) \rangle - \lambda \left[\int_0^T dt |E(t)|^2 - E \right], \ \alpha = target. \tag{2.15}$$

Here λ is a Lagrange multiplier.

If one imposes the constraint that the Schrödinger equation must be satisfied, the modified objective functional, which should be optimized, takes the following form:

$$\begin{aligned} \bar{J}_\alpha = \langle \psi(T) | \hat{P}_\alpha | \psi(T) \rangle + 2Re \int_0^T dt \langle \chi(t) | i\hbar \frac{\partial}{\partial t} \\ - \hat{H} | \psi(t) \rangle - \lambda \left[\int_0^T dt |E(t)|^2 - E \right]. \end{aligned} \tag{2.16}$$

If $\psi(t)$ satisfies the time-dependent Schrödinger equation, the second term on the right hand side of (2.16) vanishes for any $\chi(t)$, and the third term is zero when $E(t)$ satisfies (2.14). Both of these terms allow variations of $\bar{J}_\alpha$ with respect to $E(t)$ and $\chi(t)$ independently to the first order in $\delta E(t)$.

The condition $\delta \bar{J}_\alpha / \delta \psi = 0$ generates a partial differential equation for the Lagrange multiplier function $\chi(t)$

$$i\hbar \frac{\partial \chi(t)}{\partial t} = \hat{H} \chi(t), \tag{2.17}$$

which is the time dependent Schrödinger equation subject to the final condition

$$\chi(T) = \hat{P}_\alpha \psi(T), \tag{2.18}$$

and a partial differential equation for $\psi(t)$

$$i\hbar \frac{\partial \psi(t)}{\partial t} = \hat{H}\psi(t), \tag{2.19}$$

subject to the initial condition

$$\psi(0) = \psi_0. \tag{2.20}$$

Finally, the optimal applied field is defined by the condition $\delta \bar{J}_\alpha / \delta E(t) = 0$ which leads to

$$E(t) = -\frac{i}{\lambda\hbar} \left[\langle \chi_g(t) | \hat{\mu}_{ge} | \psi_e(t) \rangle - \langle \psi_g(t) | \hat{\mu}_{ge} | \chi_e(t) \rangle \right] \tag{2.21}$$

with

$$\lambda^2 = \frac{1}{E} \int_0^T dt | \langle \chi_e(t) | \hat{\mu}_{eg} | \psi_g(t) \rangle - \langle \psi_e(t) | \hat{\mu}_{eg} | \chi_g(t) \rangle |^2, \tag{2.22}$$

where μ_{eg} is the dipole operator and the indices e and g label the excited and the ground state energy surfaces. The equation of motion of the coupled amplitudes on two potential energy surfaces reads

$$i \frac{\partial}{\partial t} \begin{pmatrix} \psi_e \\ \psi_g \end{pmatrix} = \begin{pmatrix} \hat{H}_e & \hat{V}_{ge} \\ \hat{V}_{eg} & \hat{H}_g \end{pmatrix} \begin{pmatrix} \psi_e \\ \psi_g \end{pmatrix}, \tag{2.23}$$

with the interaction potential $\hat{V}_{ge}$ defined as $\hat{\mu}_{ge} E(t)$.

The numerical calculations then involve an iterative procedure which includes the following:
(i) initial guess for the pulse shape $E(t)$;
(ii) integration of the Schrödinger equation forward starting from the initial condition in the ground state;
(iii) application of the projector operator which selects the target (the exit channel to $\psi(t)$) to obtain $\chi(t)$ as an initial value for backwards propagation;
(iv) propagation of $\chi(t)$ backwards in time;
(v) during the propagation, calculation of the overlap function

$$O(t) = i \left[\langle \chi_e(t) | \hat{\mu}_{eg} | \psi_g(t) \rangle - \langle \psi_e(t) | \hat{\mu}_{eg}(t) | \chi_g(t) \rangle \right]; \tag{2.24}$$

and
(vi) after completion of the backwards propagation, renormalization of the result needed to obtain the new pulse

$$E(t) = O(t) \left(\frac{1}{E} \int_0^T dt |O(t)|^2 \right)^{-1/2}. \tag{2.25}$$

(vii) iterative procedures starting from step (ii) should be repeated until convergence has been achieved (cf. [17, 122]).

2.4.1.3 Local vs. global in time optimization

As described above, the optimal control equations typically have the structure of five coupled differential equations: one for the wave function, one for the *dual* wave function, an initial condition on the wave function, a final condition on the dual, and finally, an equation for the optimal field, which in turn is expressed in terms of the wave function and its dual.

Typically, the OCT equations have to be solved via an iterative procedure, involving forwards in time propagation of the wave function, followed by backwards in time propagation of the dual, until self-consistency is achieved with respect to the equations for the wave function, the dual and the control field. Because of the structure of this forwards-backwards propagation, the optimal field 'knows' about the future, i.e. the form of the optimal field at time t takes into account the dynamics at time $t' > t$. Thus, the optimal field may be willing to tolerate a nonmonotonic increase in the objective during the action of the pulse, since, given knowledge of the future, that may be the best way to attain the highest objective at the final time (see Fig. 2.28a).

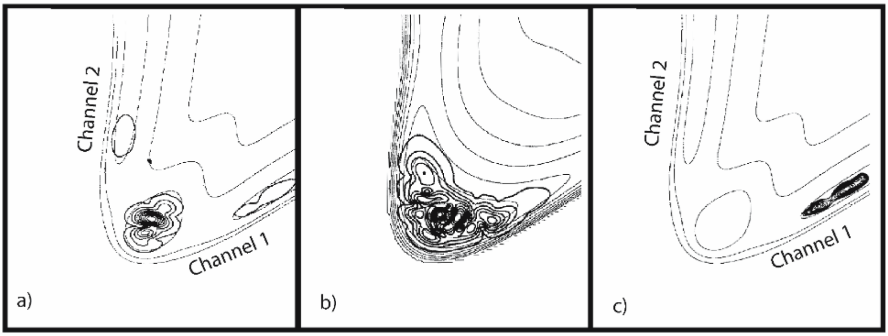

Fig. 2.28. Representative plot showing the difference between global-in-time and local-in-time optimization. (a) In global-in-time optimization, the objective may decrease at intermediate times, but is guaranteed to take on its maximum value at the final time. (b) In local-in-time optimization, the objective increases monotonically in time.

A different class of techniques that have been developed for control of atomic and molecular dynamics is called 'local optimization' [138–149]. In these methods, at every instant in time the control field is chosen to achieve monotonic increase in the desired objective see Fig. 2.28b. Typically in these methods, two conditions are used at each time step, one to determine the phase of the field and one to determine the amplitude. In contrast with OCT, which incorporates information on later time dynamics through forward-backward iteration, these methods use only information on the current state of the system.

At first glance, one would expect that the solution(s) that come out of an optimal control calculation would give a higher value of the objective than that from the local optimization: since the approach to the objective in OCT at intermediate times is unconstrained, while in local optimization it is constrained to increase monotonically in time, one expects a higher yield from OCT since the space of allowed solutions includes those from local optimization as a subset see Fig. 2.29a. However, there is one fallacy with the above argument. The optimal control equations generally have multiple solutions; these solutions are in general *local*, not global maxima in the function space (see Fig. 2.29b). Thus, the value of the objective attained with the local-in-time optimization algorithm can be larger than that obtained with the optimal control algorithm, since the latter may be stuck in the region of a poor quality local maximum!

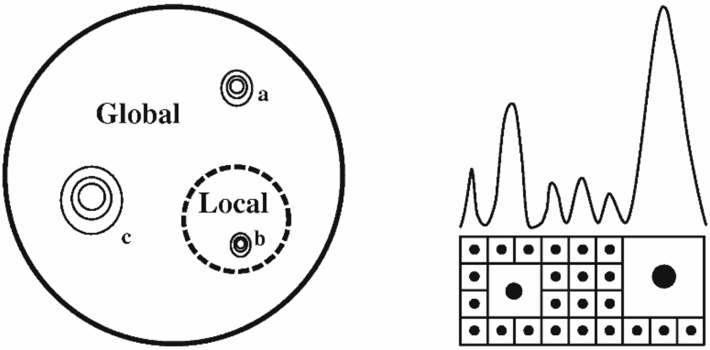

Fig. 2.29. Left: Venn diagram of the set of control fields. Fields that yield monotonically increasing solutions are a *subset* of the set of fields that lead to either an increase or a decrease at intermediate times. (Concentric circles indicate neighborhoods of fields that lead to a local maximum in the objective in the function space.) Right: The checkerboard is a schematic depiction of the space of all allowed control fields. The dots indicate the positions of the optimal fields, i.e. fields that lead to a local maximum of the objective in the function space. The squares show "basins of attraction", i.e. neighborhoods of control fields that converge to the same optimal field. The one-dimensional function above the checkerboard symbolizes the value of the objective, and it, (as well as the concentric circles in the figure on the left) are intended to convey the idea of multiple *local* maxima (see text).

There are several other attractive features to the local methods. 1) Since the increase in yield is continual, these fields are often amenable to immediate interpretation. 2) Since these methods use only information on the current state of the system, they could in principle be adapted for laboratory implementation. 3) These methods, because they differ so radically in algorithm from OCT, are capable of identifying entirely different classes of mechanisms which may be appealing because of other properties, e.g. robustness.

2.4.2 Local control theory and the analysis of control processes

When approaching the problem of the analysis of laser control from a theoretical point of view, the question to be asked is: ‘How can one relate the outcome of a laser-control process to the properties of the driving electric field?’ To answer this question, the approach of local control theory as introduced in Sec. 2.4.1 is discussed. For this purpose, two specific examples will be presented, which illustrate, - without going into the most general formulation - the basic ideas. They also demonstrate how the “analysis” aspect is inherent to this theory.

2.4.2.1 Infrared dissociation of a diatomic molecule

As a first example, the infrared dissociation of a diatomic molecule is treated. Therefore, only the radial motion in the single coordinate r is considered and the rotational degree of freedom is frozen. In order to initiate a fragmentation, the energy of the vibrational motion must exceed the dissociation energy, that is, the control field should be such, that an effective energy transfer from the field to the molecule is guaranteed (a process which, in what follows, is referred to as ‘heating’), and a sufficient condition that this takes place is that the rate of energy transfer is positive at all times.

The Hamiltonian of a molecule with reduced mass m can be given as

$$\hat{H}_0 = \frac{\hat{p}^2}{2m} + \hat{V}(r), \tag{2.26}$$

where $\hat{p}$ is the momentum operator, and $\hat{V}(r)$ denotes the potential energy which provides a set of bound states. The internal energy rate then is calculated as the time-derivative

$$\frac{d}{dt}\langle \hat{H}_0 \rangle_t = \frac{d}{dt}\langle \psi(t)|\hat{H}_0|\psi(t)\rangle = \frac{i}{\hbar}E(t)\langle \psi(t)|[\hat{T}, \hat{\mu}]\psi(t)\rangle. \tag{2.27}$$

Here, $|\psi(t)\rangle$ is the time-dependent molecular state and $[\hat{T}, \hat{\mu}]$ denotes the commutator between the kinetic energy operator $\hat{T}$, and the dipole operator $\hat{\mu}$, where the latter appears in an additional term of the total Hamiltonian containing the dipole interaction of the molecule with an external field $E(t)$:

$$\hat{W}(t) = -\hat{\mu}(r)\; E(t). \tag{2.28}$$

Within local control theory, the field is constructed from the instantaneous dynamics of the system. In particular, the choice

$$E(t) = \lambda Im\langle \psi(t)|[\hat{\mu}, \hat{T}]|\psi(t)\rangle, \tag{2.29}$$

leads to energy absorption if the value of λ is taken to be positive, as can be readily taken from (2.27) realizing that the expectation value of the commutator is purely imaginary [194].

Assuming now, for the purpose of illustration, a linear dipole moment ($\hat{\mu}(r) = \mu_0 + \mu_1 r$) this will lead to the rate expression

$$\frac{d}{dt}\langle \hat{H}_0 \rangle_t = \frac{\mu_1}{m} E(t) \langle \hat{p} \rangle_t . \tag{2.30}$$

It is now easy to anticipate that, if the field is in phase with the expectation value of the momentum operator, the rate is positive ('heating'), whereas for a field being out of phase, a negative rate is obtained, i.e. the system is 'cooled'. Thus, here the entanglement between control field and system dynamics is clearly visible. Returning to the problem of infrared dissociation, this means that a control field which permanently pumps energy into the system, is directly connected to the momentum. If energy is transferred into the system, the frequency of the vibrational motion will, due to the anharmonicity of the potential curve (and the decreasing spacing of the energy levels), decrease as time goes along. Thus, the driving field is "down-chirped" by construction. Here, local control theory directly leads to the conclusion that a down-chirped field induces an effective infrared dissociation [195, 196].

The interpretation of the control field in terms of expectation values can easily be carried over to the classical picture Therefore, in (2.27), the commutator is replaced by the Poisson bracket [197] as

$$[\hat{T}, \hat{\mu}] \leftrightarrow (i\,\hbar)\,\{T, \mu\} = (i\,\hbar)(\frac{\partial T}{\partial r}\frac{\partial \mu}{\partial p} - \frac{\partial T}{\partial p}\frac{\partial \mu}{\partial r}) = -(i\,\hbar)\frac{\mu_1}{m} p(t), \tag{2.31}$$

where $p(t)$ is the classical momentum. This is the well studied problem of a classically driven oscillator [198]. In particular, the induced molecular fragmentation corresponds to the case of a resonantly driven oscillator with ever increasing energy. The connection between classical and quantum treatments of control processes has been explored in detail before, see e.g. [199–201].

To illustrate what has been said above, a simplified model of the NaI molecule is regarded. This system served as one of the first gas-phase examples to demonstrate the power of femtosecond spectroscopy [1, 2] and laser control [202], for additional work see, e.g. [203–207]. Fig. 2.30, upper panel, shows an excitation scheme where a first pulse ($E_p(t)$) excites the system from its electronic ground state $|0\rangle$ to an excited state $|1\rangle$. The scenario to be discussed below is, that an additional control field $E(t)$ is applied to induce an excited state dissociation. Within the model, the nonadiabatic coupling of the two electronic states occurring around 7 Å is neglected [208], for the effect of the predissociation channel see [209]. The lower panel of the figure shows the dipole moment in the excited state [210]. At smaller distances, the function vanishes indicating a covalent bonding situation, whereas for longer bondlengths the dipole moment is linear, illustrating the ionic character of the electronic state.

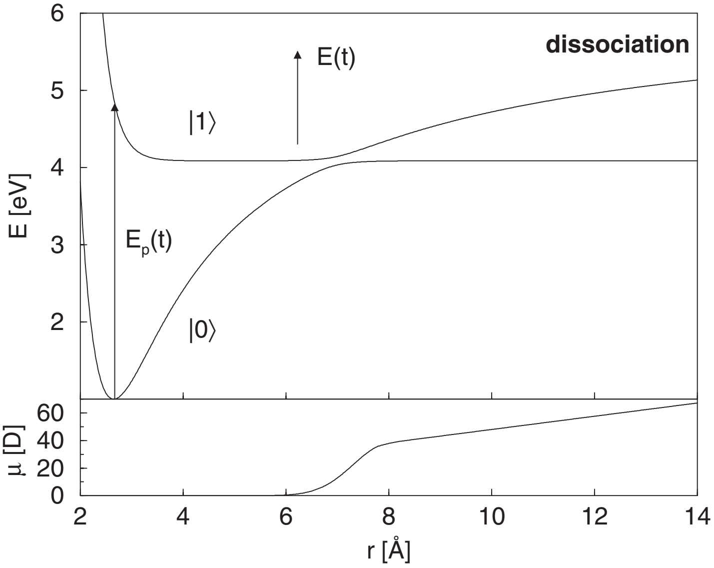

Fig. 2.30. Upper panel: excitation scheme for the NaI molecule. An initial transition ($|1\rangle \leftarrow |0\rangle$) induced by the pump field $E_p(t)$ prepares a vibrational wave packet in the excited state. An additional control field $E(t)$ then heats the system so that excited state dissociation becomes effective. The lower panel shows the permanent dipole moment in the excited state. Its functional form illustrates the change from a covalent (at distances smaller than the region where the avoided crossing occurs) to an ionic bonding situation at larger bond lengths.

The pump-pulse transition from the vibronic ground state is treated by time-dependent perturbation employing a pulse-width of 50 fs and a photon energy of 3.875 eV. This prepares a vibrational wave packet which enters into the determination of the electric field via (2.29). Results obtained from a calculation with fields of different strength parameters λ are contained in Fig. 2.31. There, the excited state populations $P(t)$ (upper panels), the bond-length expectation-values $\langle r \rangle_t$ (middle panels) and the control fields $E(t)$ (lower panels) are shown. The coordinate expectation-values reflect the vibrational wave packet dynamics which proceeds with increasing amplitude and decreasing frequency. In the case of the weaker field (right panels), three oscillations are completed before the system has absorbed sufficient energy for fragmentation to take place (at around 8.5 ps). It is then, that the fraction of still bound molecules $P(t)$, calculated from the norm of the wave packet for values $r \leq$ 20 Å) decreases, and a fragmentation yield of approximately 60% is obtained at longer times. The control field (lower right panel) follows the vibrational dynamics, exhibiting the same characteristic oscillations which demonstrates the entanglement of field and system dynamics. The same trends are present

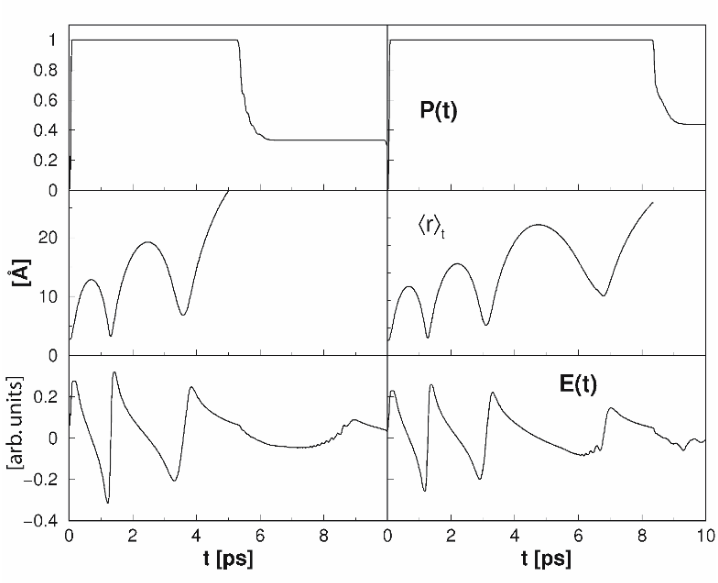

Fig. 2.31. Analysis of the laser induced excited state fragmentation of NaI. Results are displayed for different values of the field strength parameter $\lambda = 6 \cdot 10^{-6}$ a.u. (left panels) and $\lambda = 5 \cdot 10^{-6}$ (right panels). The lower panels show control fields $E(t)$ which oscillate with the instantaneous vibrational period of the wave packet motion. This can be seen in comparing the fields to the bond length expectation values (middle panel). The vibrational motion proceeds with increasing amplitude and decreasing frequency until the bound state population $P(t)$ (upper panels) starts decreasing, i.e. fragmentation takes place.

for the stronger driving field (left panels of Fig. 2.31). There, it takes only two vibrational periods until the necessary energy is absorbed so that, on the way outward a substantial part of the wave packet enters the exit channel at about 5 ps. Here, about 70% of the molecules undergo dissociation.

It is noted that at longer times, no additional fragmentation takes place. This is due to the dispersion of the wave packet which moves in an extremely anharmonic potential. As soon as the packet becomes de-localized, the expectation values entering into the construction scheme for the fields become meaningless [211]. In other words, the efficiency, but also the interpretation of the fields in terms of a classical-like motion rests on the property that the wave packets are localized in comparison with the extension of the system, for a discussion see, e.g. [212].

2.4.2.2 Population transfer between electronic states

As a second example, electronic transitions in the Na_2 molecule are regarded. In Fig. 2.32a, three electronic states are displayed. The femtosecond spec-

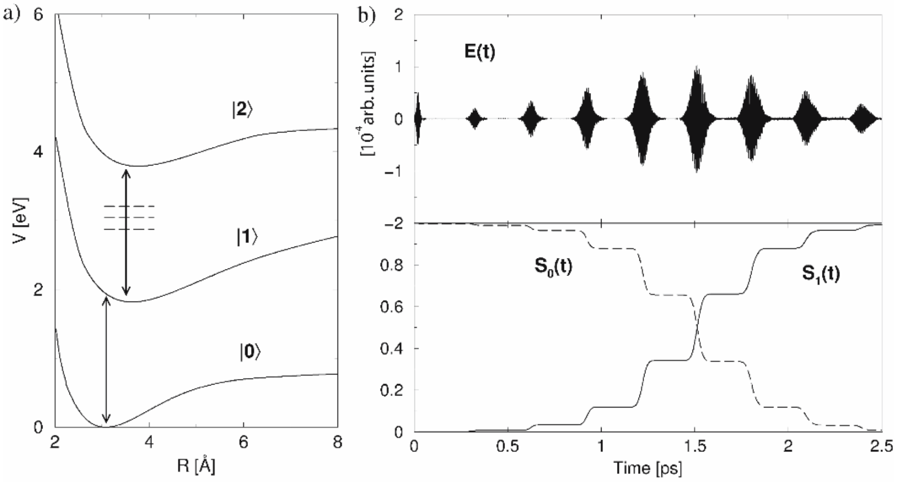

Fig. 2.32. a) Excitation scheme of the Na_2 molecule. In coupling three electronic states to a control field the objective is a complete population transfer from the ground ($|0\rangle$) to the first excited state ($|1\rangle$) without loosing population into the higher state ($|2\rangle$). b) Lower panel: time-dependence of the population in the electronic ground ($S_0(t)$) and first excited state ($S_1(t)$). The population in the second excited state ($|2\rangle$) is too small to be seen in the figure. The upper panel contains the control field and, at early times, a seed pulse which transfers a small amount of population to the state $|1\rangle$. The pulse train reflects the vibrational dynamics in the excited state.

troscopy of this dimer, employing pulses of around 620 nm wavelength is well understood [213–215]. In what follows, a complete population transfer form the ground state $|0\rangle$ to the first excited state $|1\rangle$ without a loss into the excited state $|2\rangle$ (and as a consequence to any other higher lying states) is considered. As above, local control theory is used with the hope to find a field which effectively triggers the transition and also is easily understood in terms of the system dynamics.

To put the objective into the frame of LCT, the rate of population transfer to the excite state is calculated. Therefore, the molecular state vector is represented as

$$|\psi(t)\rangle = \sum_{n=0}^{2} \psi_n(r,t)\ |n\rangle, \tag{2.32}$$

where $\psi_n(r,t)$ is the vibrational wave function in the electronic state $|n\rangle$. The population in the target state $|1\rangle$ is then calculated with the help of the projector $\hat{A}_1 = |1\rangle\langle 1|$ as

$$P_1(t) = \langle\psi(t)|\hat{A}_1|\psi(t)\rangle. \tag{2.33}$$

Upon taking the time-derivative and evaluating appearing commutators one finds [145, 148]

$$\frac{d}{dt}P_1(t) = -E(t)\frac{2}{\hbar}Im\{\langle\psi_1(r,t)|\mu_{10}|\psi_0(r,t)\rangle + \langle\psi_1(r,t)|\mu_{12}|\psi_2(r,t)\rangle\}, \tag{2.34}$$

where Im denotes the imaginary part and μ_{nm} is the transition dipole-moment between the states $|n\rangle$ and $|m\rangle$. Two things become apparent in inspecting the latter equation. First, in principle, by choosing the field proportional to the negative imaginary part of the sum of overlap integrals, the rate can be forced to assume only positive numbers. This then results in an increase of the target-state population at each increment of time. Second, if this choice is made, the field will, by construction, be determined from the ground- and excited state dynamics, thus an interpretation of the field properties should be readily obtainable. It should be noted, that the construction scheme needs a small initial population in the excited state because otherwise the dipole matrix elements (and thus the control fields) are identically zero at all times. This is usually achieved by applying a weak 'seed pulse' preceding the control pulse.

In this numerical example, a control field constructed as

$$E(t) = -\lambda Im\{\langle\psi_1(r,t)|\mu_{10}|\psi_0(r,t)\rangle + \langle\psi_1(r,t)|\mu_{12}|\psi_2(r,t)\rangle\}, \tag{2.35}$$

is employed. It has a strength parameter of $\lambda = 1.4 \cdot 10^{-4}$ a.u. This field (and also the seed pulse) is displayed in Fig. 2.32b (upper panel). It consists of a pulse train where several sub-pulses can be distinguished. Also shown is the ground- and excited-state population. The latter increases in steps every time, the field is non-zero, until a 100% population transfer is obtained. It is worth to note that the second excited state $|2\rangle$ is never populated, for an analysis see [216]. Thus LCT delivers a field being optimal in the sense that it completely populates the target state thereby minimizing the loss into other excitation channels.

Returning to the initially posed question, the appearance of the electric field is now analyzed. An analysis of a single sub-pulse shows that its frequency corresponds to the energy separation between the potentials in the Franck-Condon window of the $|1\rangle \leftarrow |0\rangle$ transition. Because the second excited state is not populated, the field oscillations are determined by the temporal variation of the first overlap integral appearing in (2.35) which can be evaluated as

$$\langle\psi_1(r,t)|\mu_{10}|\psi_0(r,t)\rangle = \sum_{e,g} a_e^*(t)\; a_g(t)\; \langle\psi_e|\mu_{10}|\psi_g\rangle e^{i(E_e-E_g)t/\hbar}. \tag{2.36}$$

Here, the wave functions are expanded in terms of the ground- and excited-state vibrational eigenfunctions $\psi_g(r)$ and $\psi_e(r)$ with energies E_g and E_e, respectively. Note, that the coefficients $a_e(t), a_g(t)$ are explicitly time-dependent.

From the latter equation it is clear, that the fast field oscillations are determined by the energy differences between vibrational states in the excited and ground electronic states. Thus, the frequency is automatically adjusted to induce resonant transitions. In this way, a vibrational wave packet is built in the excited state which, due to the repulsive force, moves toward longer bond-lengths so that, after a while, the overlap with the ground state wave packet, being still localized in the vicinity of the potential minimum, is diminished. As a result, the field amplitude decreases and approaches zero. The situation changes when the excited state wave packet, after performing a vibrational period, returns to the Franck-Condon region. Because then the overlap integral increases, the field amplitude rises again and the same scenario repeats itself. In this way, the vibrational motion is reflected in the structure of the pulse train: the temporal separation of the sub-pulses equals the well known vibrational period on Na_2 in its A $(^1\Sigma_u^+)$ electronic state [215]. Thus, the form of the field is clearly understandable. Additionally, the sub-pulse intensity increases until the two electronic states are equally populated and it decreases at later times.

In order that the population in the upper state does not decrease, no loss into other states has to occur. Concerning the coupling to the ground state, this means that the interference between the excited state and ground state wave packets has to be completely constructive. This is indeed the case and the scenario of wave packet interferometry [217] is encountered, which has been realized experimentally by Scherer et al. [218], see also more recent work [219]. There, a pair of phase-locked pulses are used to constructively interfere a wave packet (prepared by the first pulse) returning to the Franck-Condon region with another packet (prepared by the second pulse). By shifting the relative phase of the pulses by π, destructive interference can be obtained as well. In this approach it is straightforward to rationalize this phase-sensitivity: if the control field is multiplied with a phase factor of (-1), the rate (2.34) becomes negative, so that the excited state population is diminished, i.e. one encounters destructive interference.

The given example illustrates again, that local control theory delivers fields which are accessible to an interpretation. It is to be kept in mind, however, that the construction scheme is a purely theoretical and one aim of future investigations should be the comparison of fields derived from various algorithms with the ones from LCT, having the analysis aspect of laser control processes in mind.

2.4.3 Feedback control

The steering of dynamical processes requires a successive photon-molecule interaction, across a sequence of temporally open Franck-Condon windows of the evolving quantum system. To reach this goal, shaped fs-pulses can be applied which influence - as proposed by Judson and Rabitz [22] - the dynamics temporally and spectrally . These tailored pulses can be produced by a pulse shaper which can either be realized by an acousto-optic modulator [220] or a liquid crystal modulator mask [221] placed in the Fourier plane of a zero dispersion compressor [222] (see Fig. 2.33). Modulators with two arrays can be utilized to allow for independent spectral phase and amplitude modulation [223]. Additionally, the polarization can still be shaped as shown later in Sect. 2.4.6.

In the optimization experiment, a learning algorithm based on evolutionary algorithms [155, 156] produces new pulse shapes regarding the experimental input and the defined objective. Then the procedure is repeated several times in a loop until the optimized laser pulses give rise to the aimed experimental yield [22]. As first demonstrated by Gerber et al., the approach has opened new roads in the field of laser control, in particular, with regard to the optimization of the yield of chosen reactivity channels [224].

The experimental setup for feedback control measurements used here (see Fig. 2.33) combines a fs-laser system with a programmable liquid crystal pulse shaper and a molecular beam apparatus as already described in Sect. 2.2.3. Each pulse shape is determined by an array of numbers called individual, representing the spectral phase and amplitude values. Individuals consisting of random numbers are created in the beginning and then modified by crossover and mutation operators. After being written on the modulator, each pulse form creates an ion signal which represents its fitness. In the last step of the

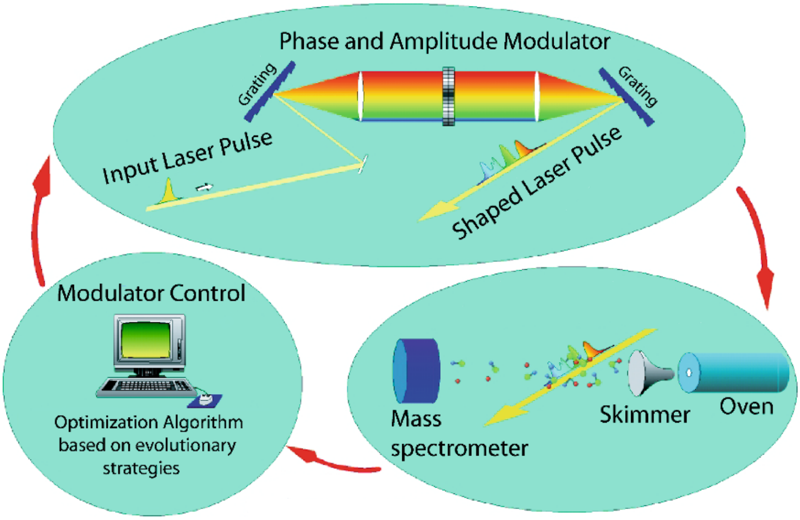

Fig. 2.33. Schematic of the closed loop experiment. Arbitrary pulse shape patterns altered by cross over and mutation operators are send to a pulse shaper. The iteratively improved pulse shapes are tested by mass selectively detecting the ion product yield. The resulting yields are a measure for the quality (fitness) of the applied pulse forms.

first cycle the best individuals are selected and serve as parents for the next iteration. For details of the applied algorithm see [162]. A Ti:sapphire laser oscillator is utilized, which provides pulses at a repetition rate of 80 MHz in the weak field regime. This allows a good signal-to-noise ratio through a very high degree of averaging, and it avoids undesired multiphotonic transitions, which would also complicate the interpretation of the obtained data.

When having obtained an optimum pulse shape the important question arises, what can be retrieved from this result with regard to the underlying dynamical processes. In order to answer this, the optimized pulse form has to be measured accurately by intensity cross correlation and spectrally resolved cross correlation (SFG-XFROG). So the cross correlation traces of the shaped test pulse and the reference pulse are recorded for different frequency components of the spectrum. When operating in the weak field regime, SFG-XFROG offers the advantage of providing an intuitive viewgraph, indicating the time-frequency character of the pulse shape. In order to fully characterize the pulse form, the amplitude and phase can be calculated from the SFG-XFROG spectrogram by an iterative phase-retrieval algorithm.

2.4.4 Controlling multiphoton ionization processes in NaK

The NaK dimer was chosen as a model system for The investigation of the multiphoton ionization process of the NaK dimer is a good model system for testing the feedback optimization procedure. The system is easily excited and ionized in a resonant three-photon process by wavelengths within an easily accessible range around $\lambda_0 = 770$ nm. Furthermore, the wave packet dynamics of low lying excited states of this system is well known from fs-pump-probe experiments; its oscillation periods are around T_{osc}^{NaK}=440 fs [225]. Also from a theoretical point of view the dynamics of the system is easily described by optimal control theory [17] as will be shown later. So the challenging question arises, whether the optimization algorithm will identify the fingerprints of these spectroscopic features.

2.4.4.1 Experimental approach

In the experiments shown here the spectral width of the laser of 9 nm was dispersed across all 128 pixels of the modulator, and pure phase optimizations were performed. So the resulting $n = 128$ spectral phase parameters $\varphi_n(\omega)$ ($\in [0 - 2\pi]$) of the shaped spectral field

$$E_{n,mod}(\omega) = E_{n,in}(\omega) \cdot A_n \; e^{-i\varphi_n(\omega)} \tag{2.37}$$

were the optimization variables, while the amplitude values were set to $A_n \equiv 1$. In Fig. 2.34a the learning curve of the optimization measurement is shown. A pronounced rise in the NaK$^+$ ion signal with increasing iteration (generation) number is clearly visible. The three values for each generation show the best, the worst and the mean of all values in one generation. The ion signal at the beginning is very small because the phase values of the first generation are randomly chosen. This leads to complex pulse structures spread over several ps. Such a randomly shaped pulse yields small ion signals. With successive iterations the signal exceeds the outcome of the transform-limited pulse after about 40 generations. Leveling off the signal is achieved after about 120 generations.

The mass spectrum (Fig. 2.34b) shows the distribution of NaK ions produced by a transform-limited pulse. The NaK^+ intensity is dominant. Larger $\mathrm{Na}_n\mathrm{K}^m$ clusters are not detectable in the beam. The ion distribution after optimization is represented in Fig. 2.34c. The optimization factor amounts to

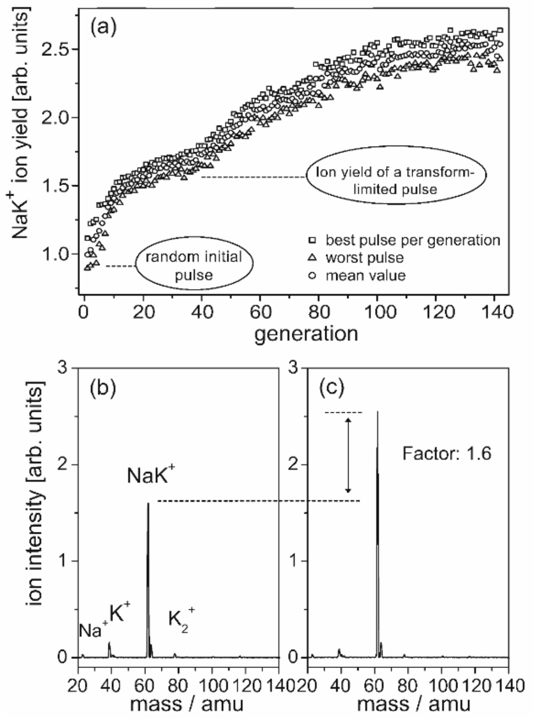

Fig. 2.34. (a) Progression of the NaK^+ ion signal during optimization. At the beginning the yield is small since the initial pulses are randomly formed. After approximately 120 generations convergence is reached. The value achieved by a transform-limited pulse is exceeded after approximately 40 generations. Shown are the values for the best, the worst and the mean for each generation. (b) The mass spectrum of the transform-limited pulse exhibits only monomers and dimers. (c) The mass spectrum recorded with an optimized pulse reveals an increased NaK^+ yield of $I_{opt}/I_{tl} = 1.6$. [226]

$I_{opt}/I_{tl} = 1.6$, where I_{opt} is the optimized ion yield and I_{tl} the yield from the transform limited pulse. Thus, the phase optimized control pulse leads to a noticeably higher ion yield than the short pulse, even though the peak intensity is reduced due to its time stretched profile. In the following the optimized pulse form will be analyzed.

The intensity cross correlation of an optimized pulse form for NaK^+ is depicted in the upper part and the SFG-XFROG trace in the lower part of the Fig. 2.35. The cross correlation shows a sequence of three main pulses. The first and second pulses are separated by $\Delta t_{1,2} \approx 650$ fs and the second and third pulses by $\Delta t_{2,3} \approx 220$ fs. The intensities of the sub pulses differ substantially: the first pulse is weak, the central pulse is strong and is followed by a weaker third pulse. The intensity ratio of these pulses is about 1:4:2.

The SFG-XFROG trace in Fig. 2.35 reveals a slight quadratic frequency chirp for the first sub pulse and a positive chirp for the middle sub pulse. The third pulse is also slightly chirped and blue shifted with respect to the second pulse. The pulse separation of $\Delta t_{1,2} \approx 220$ fs and $\Delta t_{2,3} \approx 650$ fs correspond

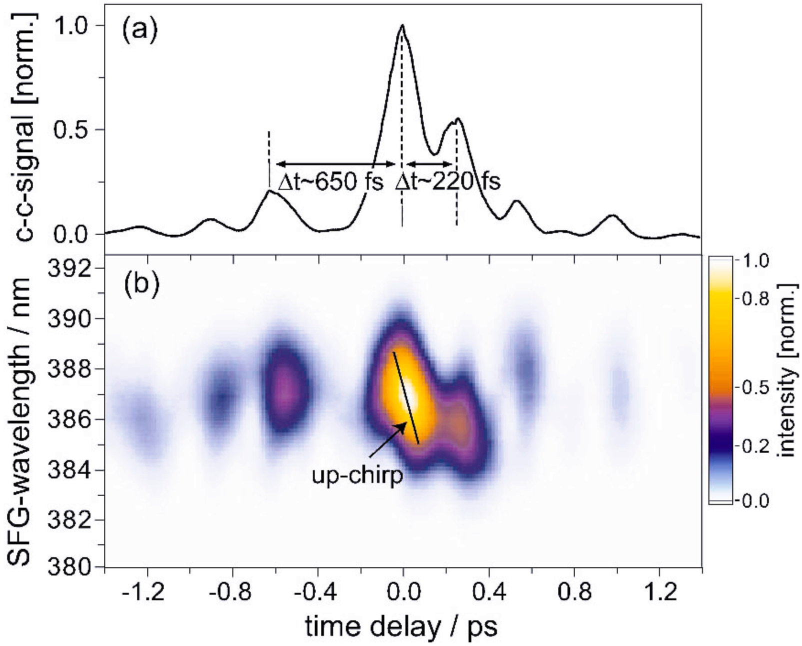

Fig. 2.35. Phase optimized control pulse for the ionization of NaK. (a) The intensity cross correlation of the pulse reveals a pulse train consisting of three main pulses. The distance between the first and the central pulse is $\Delta t_{1,2} \approx 650$ fs, whereas the central and the third pulse are separated by $\Delta t_{2,3} \approx 220$ fs. (b) The SFG-XFROG trace reveals a positively chirped central pulse and a blue shift of the third pulse. [226]

to half and one and a half oscillation periods in the excited $A^1\Sigma^+$ state, respectively, which was observed by means of fs pump-probe spectroscopy at $\lambda_{pump} = \lambda_{probe} = 770$ nm [225].

The phase profile of the pulse shape, calculated from the SFG-XFROG trace with a phase retrieval algorithm, reveals a complex structure with a phase shift of approximately $\Delta\varphi \approx 1.5 \cdot \pi$ over the whole range. For the positively chirped middle pulse a quadratic phase is found, from which the main component of the linear chirp could be calculated to $b_2 \cong +1220$ fs^2.

The result emphasizes a first simple explanation of the optimized pulse shape. In the process involved are all relevant electronic states, namely the ground state $X(1)1\Sigma^+$, the excited states $A(2)^1\Sigma^+$, $b(1)^3\Pi$, $B(3)^1\Pi$, $A(6)^1\Sigma^+$ and the ionic ground state $X(1)$ NaK$^+$ (see Fig. 2.36). Prior to the interaction with the laser pulse the system is located in the electronic and vibrational ground state $X(1)^1\Sigma^+$. The first subpulse creates a wave packet in the excited $A(2)^1\Sigma^+$ state (see Fig. 2.36). Contributions of wave packet motion in higher states are neglected here, since they do neither appear in the pump-probe spectra of NaK [225].

The generated wave packet subsequently evolves across the potential of the $A(2)^1\Sigma^+$ state. Due to the Franck-Condon principle the wave packet is created at the inner turning point of the $A(2)^1\Sigma^+$ state and it requires $T_{osc}^{NaK} = 440$ fs to return to the starting point [225]. The second subpulse arrives after $\Delta t_{1,2} \approx 650$ fs when the wave packet is located at the outer turning point. Also the pump-probe spectrum shows a markedly enhanced NaK$^+$ ion yield at the same spacings of two transform limited pulses of $\Delta t = (2n+1) \cdot 220$ fs. So , ionization occurs most efficiently, when the subpulse is applied, while the wave packet is situated at the outer turning point of the $A(2)^1\Sigma^+$ state. This position is optimally located with regard to a resonant two photonic ionization across the $B(3)^1\Pi$ state.

Since the intensity of the second subpulse is rather high it can very well also excite remaining particles from the $\mathrm{X}(1)^1\Sigma^+$ ground state to the excited $A(2)^1\Sigma^+$ state and create another wave packet there. So half an oscillation period later also these particles are ionized by the third subpulse which appears precisely $\frac{1}{2}T_{vib} = 220$ fs later. The relative intensities of the pulses support this interpretation. The excitation into the $A(2)^1\Sigma^+$ state by the first pulse is a one photon transition. The second pulse performs a two photon ionization (and additionally a one photon excitation into the $A(2)^1\Sigma^+$ state) and is therefore more intense. The intensity of the last pulse again reflects the two photon process, as presented in Fig. 2.36.

The question can be raised whether the experimentally obtained pulse shapes can be reproduced by optimal control theory, which would allow also to gain a significantly more detailed insight into the underlying processes.

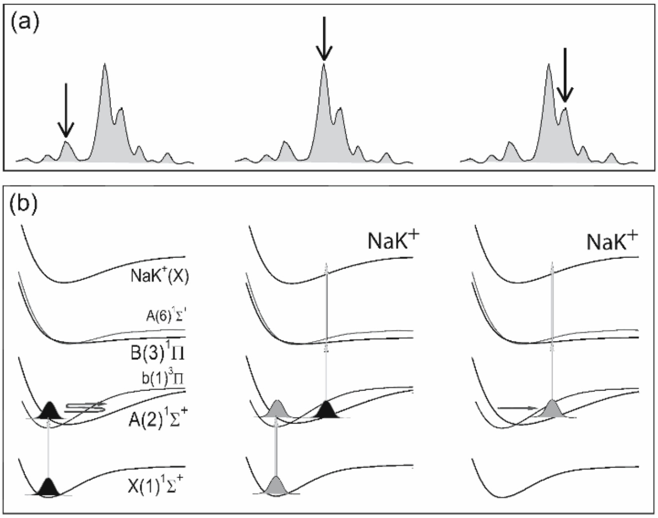

Fig. 2.36. Emphasized three step mechanism of the phase optimized photoinduced transition from the ground neutral state of NaK to the ground ionic state of NaK^+. (a): Optimized pulse train taken from Fig. 2.36a. The active subpulses are indicated by arrows. (b): The first subpulse creates a wave packet in the excited $A(2)^1\Sigma^+$ state of NaK, which is transferred into the ion state at the outer turning point of the potential by the second subpulse. This sequence is repeated with the second and third subpulse. The shown potential energy curves of NaK were taken from Magnier et al. [227]. [226]

2.4.4.2 Theoretical approach

The optimization of laser fields for controlling the photoionization in NaK has been performed using optimal control theory formulated by Kosloff et al. [17] as outlined previously . The combination of i) electronic structure, ii) quantum dynamics and iii) optimal control considering iv) experimental conditions will briefly be described. i) accurate potential energy surfaces for the ground and excited states of NaK are available in the literature [227] and have been extended by calculation of the cationic ground state necessary for the consideration of the ionization process. For this purpose the calculations using the ab initio full CI method for the valence electrons and an effective core potential with core-polarization (ECP-CPP) together with adequate AO basis sets [7s6p5d2f/5s5p4d2f] for Na and [7s5p7d2f/6s5p5d2f] for K atoms have been performed. Investigation of photoionization processes in the energy interval of 4.83 eV corresponding to three photons of 1.61 eV used in the experiments involves the three excited states $2\ {}^1\Sigma^+$, $3^1\Pi$, and $6\ {}^1\Sigma^+$ of the neutral NaK which are resonant with one- and two-photon energies, respectively. ii) Quantum dynamics simulations have been carried out by representing the wave function on a grid and using a nonperturbative approach based on a Chebychev polynomial expansion of the time evolution operator [228]. The interaction with the time-dependent electric field, which involves ground and three excited states of the neutral NaK as well as a manifold of cationic states, has been treated within the dipole approximation and using the rotating wave approximation (RWA) being justified in the weak field regime. The rotational motion has been neglected because of the large atomic masses and short time scales involved.

The outlined procedure involves the following steps. The Hamiltonian $\hat{H}$ is given in Born–Oppenheimer and dipole approximation

$$\hat{H}(t) = \hat{T} + \hat{V} - \hat{\mu}_{ge} E(t) , \tag{2.38}$$

where $\hat{T}$ is the operator of the nuclear kinetic energy, $\hat{V}$ stands for the potential energy curves of the considered electronic states (both operators are diagonal), and $\hat{\mu}_{ge}$ is the transition dipole moment between the considered electronic states and is off diagonal.

In rotating wave approximation e. g. a cosine-like real electric field can be replaced by

$$E_{\mathrm{RWA}}(t) = \frac{1}{2} A(t) e^{i\omega t} . \tag{2.39}$$

The time propagation follows the principle of a successive application of the time evolution operator

$$|\Psi(t_0 + n\Delta t)\rangle = \prod_{j=0}^{n-1} \hat{U}(t_0 + (j+1)\Delta t, t_0 + j\Delta t)|\Psi(t_0)\rangle, \tag{2.40}$$

with

$$\hat{U}(t + \Delta t, t) = e^{-i\hat{H}(t)\Delta t} , \tag{2.41}$$

assuming that the Hamiltonian does not change significantly within time Δt and can be replaced by piecewise constant terms.

After a normalization of the eigenvalue spectrum of $\hat{H}$ to the range [-1,1], the polynomial expansion of the normalized time evolution operator $e^{-i\hat{H}'\Delta t'}$ can be obtained by means of the Chebychev propagator [228]

$$e^{-i\hat{H}'\Delta t'} \approx \sum_{n=0}^{N} (2 - \delta_{0,n})(-i)^n J_n(\Delta t') T_n(\hat{H}') , \tag{2.42}$$

where T_n represents the n–th Chebychev polynomial and $J_n(\Delta t')$ are Bessel functions of the first kind of order n. Since the Bessel function decreases exponentially if the order n becomes larger than the argument $\Delta t'$, an exponential convergence of the expansion coefficients of (2.42) can be achieved.

iii) The objective of the optimal control is the maximization of the photoionization yield and the target operator corresponds to the total occupation of the cationic states. For the transition dipole moments between the excited electronic states of the neutral species and the ground state cation [178,179,181–184] the constant value of 5 Debye was chosen. It is in the range of transition dipole moments between electronic states of the neutral NaK and is sufficiently large to provide the robustness of the optimized pulses according to [229] and the experience. The influence of the nuclear distance-dependent transition dipole moments (cf. [184]) has been tested and found to be negligible. However, an explicit treatment of the electronic continuum for the cationic ground state dramatically influences the optimization of the ionization process and therefore it is mandatory for the appropriate treatment. For this purpose, the electronic continuum was discretized by introducing fourteen replica of the cationic ground state with energy differences of 95 cm^{-1} in the range from 1075 cm^{-1} to 2310 cm^{-1} for the electron kinetic energies . This energy range covers both, the direct and the sequential photoionization from the outer turning points of the involved electronic states. For the optimization of the pulses the Krotov algorithm [230] has been employed with additional penalty factors which allows to take into account the experimental conditions. The experimental parameters were described in the last Section where the optimization experiment was presented. The experiments were carried out in the weak field regime which is comprised in the theoretical treatment and the magnitude of the simulated laser field was adjusted to the experimental values according to the method given in [183].

2.4.4.3 Optimized pulses: Comparison between theory and experiment

Theoretically optimized pulses in the framework of OCT, obtained according to the procedure outlined above using experimentally optimized pulses as an initial guess, are shown in Fig. 2.37 [231]. They are compared with the experimentally optimized pulse using the CLL technique described above, which provided an increase of the ion yield by 60% with respect to that generated by a transform limited pulse. The leading features of both phase modulated pulses obtained from OCT and CLL are in a good agreement, as shown in Fig. 2.37a. The snapshots of the wave packet propagation under the influence of the theoretically optimized pulse (Fig. 2.37b) serve to assign the subpulses to underlying processes and to reveal the mechanism responsible for the population of the cationic state.

The role of the P_1 subpulse is to transfer a part of the population from the ground electronic state to the first excited $2\ {}^1\Sigma^+$ state. This creates a wave packet in the $2\ {}^1\Sigma^+$ state which propagates almost to the outer turning point within 180 fs. Subsequently, at the outer turning point the dominant P_2 subpulse simultaneously transfers the population to the $3\ {}^1\Pi$ state by a one-photon process as well as to the cationic ground state by a resonant

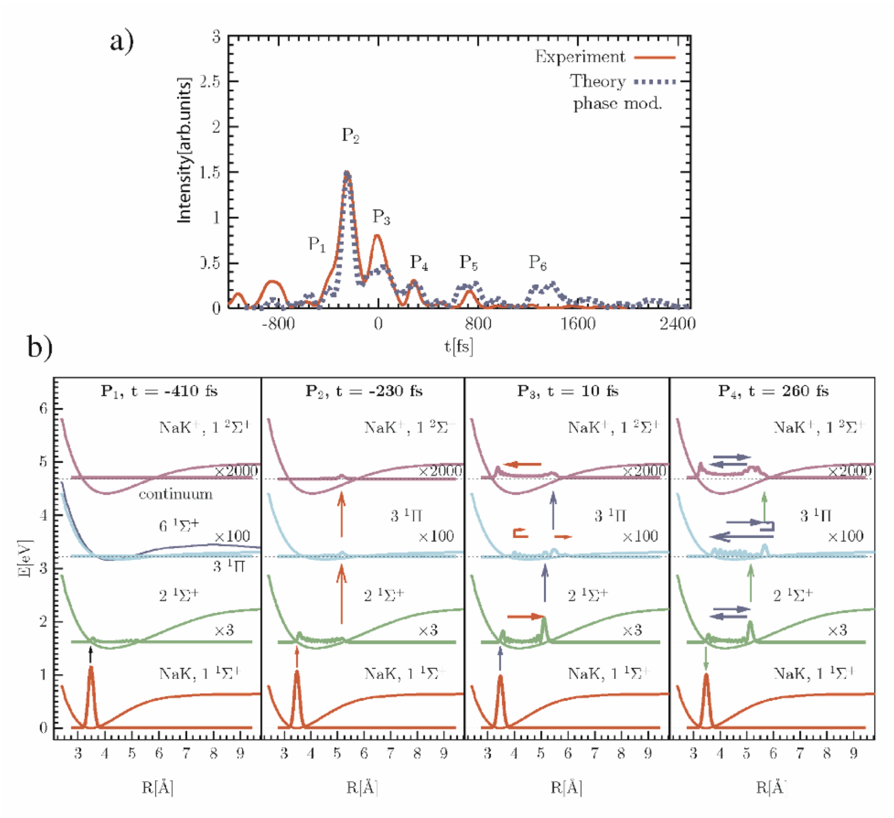

Fig. 2.37. (a) Comparison of the theoretically (dotted line) optimized phase-modulated pulse (starting with the experimentally optimized pulse) with the experimentally (solid line) optimized pulse, using CLL procedure; (b) snapshots of the wave packet propagation corresponding to P_1 (-410 fs), P_2 (-230 fs), P_3 (10 fs), and P_4 (260 fs) [231].

two-photon process as can be seen in Fig. 2.37b. In addition, the P_2 subpulse increases the population of the $2\ ^1\Sigma^+$ state at the inner turning point. Subsequently, the P_3 subpulse brings the wave packet to the $3\ ^1\Pi$ state after the outer turning point has been reached. In contrast to the dominant subpulse P_2, the P_3 subpulse also transfers population to the cationic state by the one-photon sequential processes since the split part of the wave packet, before transferred by P_2, propagates on the $3\ ^1\Pi$ state as well. At later times, e.g. at P_4, the superposition of the wave packets complicates the propagation by interference, as can be seen from the corresponding snapshot.

The separation of the early subpulses up to P_4 reflects the motion on the $2\ ^1\Sigma^+$ state with a periodicity of $\sim$ 440 fs (oscillation period in the $2\ ^1\Sigma^+$ state), while after the P_4 subpulse the periodicity is disturbed by the influence

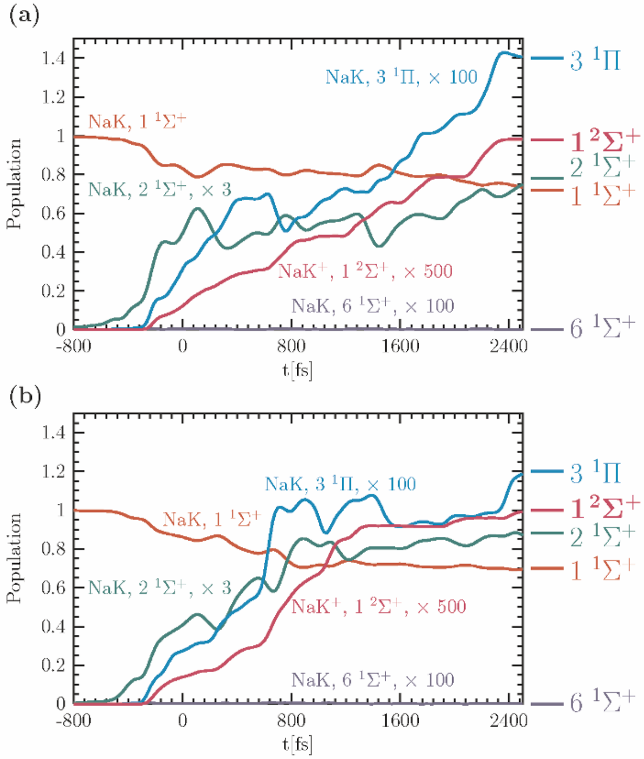

Fig. 2.38. Time-dependent population of participating electronic states of the neutral and cationic NaK, obtained from simulations with an initial guess using (a) the experimentally optimized pulse [231] (b) two Gaussian pulses [231].

of the 3 $^1\Pi$ state. The described steps leading to the desired population of the cationic state can be also identified from the analysis of the state populations displayed in Fig. 2.38a. (Notice that, besides excitation, also dump processes appear (see Fig. 2.38a). Due to the increased population of the 2 $^1\Sigma^+$ and 3 $^1\Pi$ states, the dump processes appear at 200 fs, 800 fs and 1360 fs from the 2 $^1\Sigma^+$ to the ground state and at 700 fs from the 3 $^1\Pi$ to the 2 $^1\Sigma^+$ state. Consequently, a staircase-like behavior in populations of these states is present.) Moreover, the later subpulses cause substantial increase in the population of the cationic states, showing the important contributions of the later subpulses with low intensities.

Based on the above analysis of the underlying dynamics driven by the optimized pulse, the following mechanism for the optimal ionization process of NaK can be proposed. It involves an electronic transition followed by a direct two-photon ionization from the outer turning point of the 2 $^1\Sigma^+$ state. This behavior supports the proposed explanation of the experimental optimal pulse shape given in experimental publications [165,166]. However, according to the analysis of the theoretically optimized pulses described above, the sequential one-photon ionization process mediated by the 3 $^1\Pi$ state takes over the important role at later times.

Additional insight into the energetic and temporal structure of the optimal pulse can be gained from the Wigner-Ville representation shown in Fig. 2.39b. The dominant feature is the increase of the photon energy with time. This up-chirp in the energy regime of 1.59-1.63 eV can be qualitatively explained by an overlap between the propagating wave packet on the 3 $^1\Pi$ state and the successively higher lying vibronic levels of the cationic state. For an identification of the quantitative features, amplitude and phase modulations would be more adequate. However, the X-FROG trace obtained from the experimental result [166] also shows a pronounced up-chirp in full agreement with the features displayed in Fig. 2.39b. Moreover, the up-chirp was found to enhance the NaK ion signal according to recent chirp dependent experiments [164].

In order to verify the robustness of theoretically optimized pulses, the results obtained using two Gaussian pulses separated by 660 fs as an initial guess, are compared with experimental results in Fig. 2.39. The experimental pulse is again roughly reproduced, and the leading features of the theoretical pulse remain unchanged with respect to those obtained by an experimentally optimized pulse as an initial guess (cf. Fig. 2.37). The main differences between the optimized pulses obtained with distinct initial guesses concern relative intensities of the weaker subpulses which lead only to very small relative

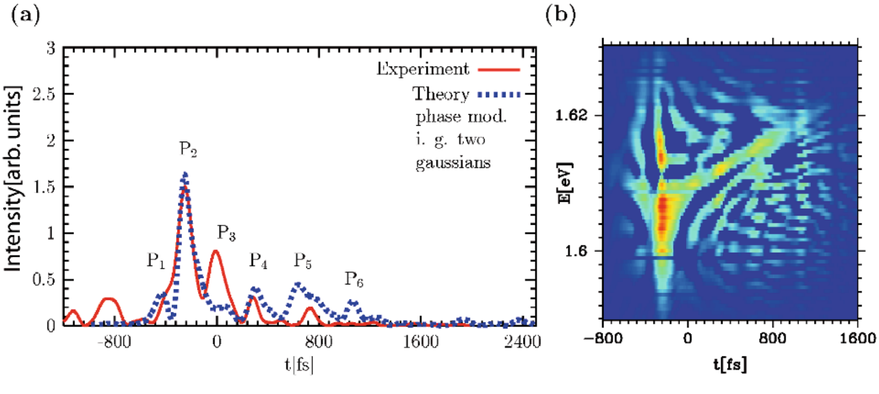

Fig. 2.39. (a) Comparison of the theoretically (dotted line) optimized phase-modulated pulse (starting with two Gaussian pulses) with the experimentally (solid line) optimized pulse, using CLL procedure; (b) Wigner-Ville distribution of the theoretically optimized pulse [231].

changes in the time dependent populations (cf. Fig. 2.38b). The Wigner-Ville representations of both theoretically optimized pulses are almost identical, verifying the robustness of the derived pulses and therefore the validity of the proposed mechanism. These findings were obtained only if the continuum of the cationic state was taken into account as described above.

In summary, the agreement between experimentally and theoretically optimized pulses, which is independent from the initial guess, shows that the shapes of the pulses can be used to deduce the mechanism of the processes underlying the optimal control. In the case of optimization of the ionization process in NaK, this involves a direct two-photon resonant process followed by a sequential one-photon processes at later times. These findings obtained from a simple system are promising for using the shapes of tailored pulses to reveal the nature of processes involved in the optimal control. Therefore, the studies were extended on isotope selective photoionization processes in NaK.

2.4.5 Isotope selectivity

The selection of particular isotopes is a topic of great interest in several fields of science and technology. Previously employed laser isotope separation schemes utilize minor isotope shifts of spectral lines [232, 233]. Yet, narrowband tunable cw-lasers and detailed knowledge of the system is required for effective isotope selection and allows only to separate the fraction present in a single quantum state. In a more recent treatment femtosecond laser pulses were employed to obtain isotope selective molecular dynamics [25, 234] and to perform isotope separation by generating spatially localized vibrational wave packets due to differences in the free evolution of the different isotopes [235]. Here an approach is presented, where feedback control by means of shaped fs-laser pulses is applied for optimizing specific isotopomer yields.

2.4.5.1 Feedback optimization of isotopomer selective ionization in K_2

As presented in Sect. 2.2, the wave packet dynamics of several electronically excited states of K_2 has systematically been investigated by means of fs-pump-probe spectroscopy. For the $A^1\Sigma_u^+$ state the results revealed oscillation periods of $T_{osc}^{K_2}$= 500 fs [25, 234]. While for the $^{39,41}K_2$ isotope dephasing occurs, a recurrence can be observed in the $^{39,39}K_2$ isotope starting at 5 ps. Thereby a π phase shift appears which leads to an almost anti-phased behavior of the oscillations between the two isotopes in a range between 5 and 15 ps. In the first approach to optimize the ratio of the two isotopes it was tried to take advantage of this long-time recurrence phenomenon. A shaped pump-probe scheme was developed where first the K_2 isotopes where irradiated with a phase and amplitude modulated pump pulse and 9 ps later (where the highest optimization ratios are expected from pump-probe results) with the probe pulse that ionizes both isotopes. The implemented closed loop experiment combines ion detection with a programmable phase and amplitude pulse shaper that is driven by a self-learning optimization algorithm based on evolution strategies. The goal of the evolutionary algorithm is to find a laser field (at 833 nm center wavelength) which maximizes or minimizes the ratio $R = I(^{39,39}K_2)/I(^{39,41}K_2)$ for the above described process. This preliminary experiment yielded a gain of the isotopomer ratio by a factor of about $S_{max} = 1.4$ and a decrease by approximately $S_{min} = 0.75$, measured with respect to the regular isotope ratio of $R_n = 6.9$ [236]. The obtained maximization and minimization ratios are even better than expected from the pump-probe spectra ($S_{max} = 1.25$ and $S_{min} = 0.8$) which already demonstrates the potential of the closed loop approach.

In order to explore this phenomenon to its full extent single shaped laser pulses were used, whereby each pulse performs the entire ionization process (see Fig. 2.40). In this case, long-time wave packet recurrences are not ex-

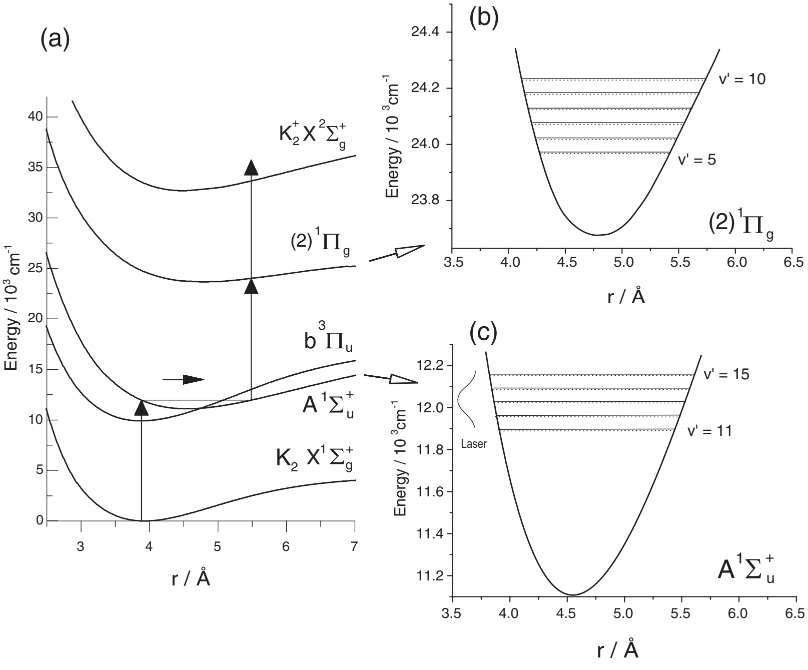

Fig. 2.40. (a) Ionization path of K_2 proposed in [237, 238]. On the right hand side are the potential energy curves and vibrational levels of the $2^1\Pi_g$ (b) and $A^1\Sigma_u^+$ state (c). The solid lines indicate the vibrational levels of the $^{39,39}K_2$ isotope and the dotted lines the levels of the $^{39,41}K_2$ isotope. The states $v'_A = 12, 13$ of the lighter isotope are disturbed by spin-orbit coupling with the $b^3\Pi_u$ state and therefore shifted by $+1.2\ \mathrm{cm}^{-1}$ and $+2.1\ \mathrm{cm}^{-1}$, respectively [25, 239]. (c) also shows the spectrum of the unshaped laser light at 833 nm central wavelength. [240]

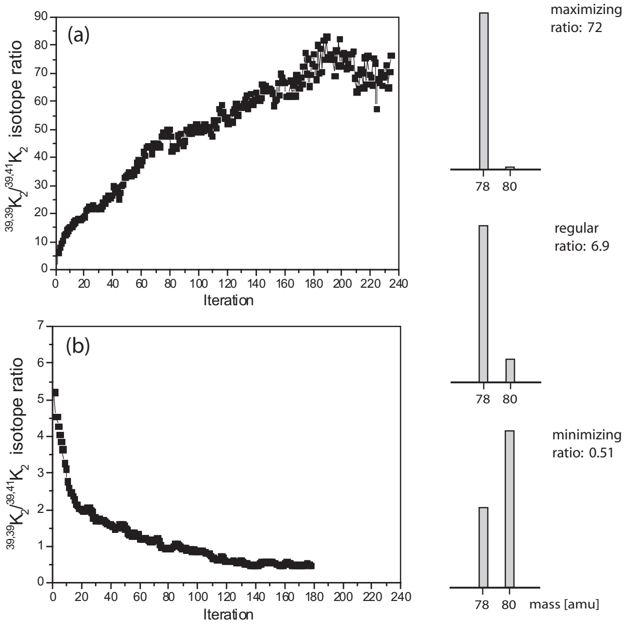

Fig. 2.41. Progressions of the mean $^{39,39}K_2/^{39,41}K_2$ ion ratio during single pulse optimization for maximization (a) and minimization (b). The considerable alteration of the isotope ratio by a factor of about 140 is also illustrated in the corresponding mass spectra on the right. [240]

pected to contribute, since the pulse shaper limits the shaped pulse duration to about 5 ps. The learning curves and the corresponding mass spectra (see Fig. 2.41) show a considerable alteration of the ion ratio by a factor of about $R_{max}/R_{min} = 140$ between minimization and maximization which provides noticeably better isotope selection results than the shaped pump-probe case ($R_{max}/R_{min} \approx 2$). This may be surprising since the shaped pump-probe experimental conditions were particularly chosen to ensure an optimal wave packet separation. Apparently, other effects are much more crucial for isotope selection than wave packet separation by recurrence phenomena. The slight enhancement of the shaped pump-probe results compared to the expected pump-probe isotope ratios already indicate this. The also performed exclusive phase optimizations provide a factor of only about 2 between maximization and minimization. Thus, the spectral amplitudes are most decisive for the observed effect which is in concordance with the results from the pure amplitude measurements (factor of about 40). This demonstrates the efficiency of combined phase and amplitude modulation.

To decipher the underlying isotope selection process, information is gained about the generated pulse shapes by recording the pulse spectra and the XFROG traces. The pulse spectrum for maximization of the $^{39,39}K_2/\ ^{39,41}K_2$

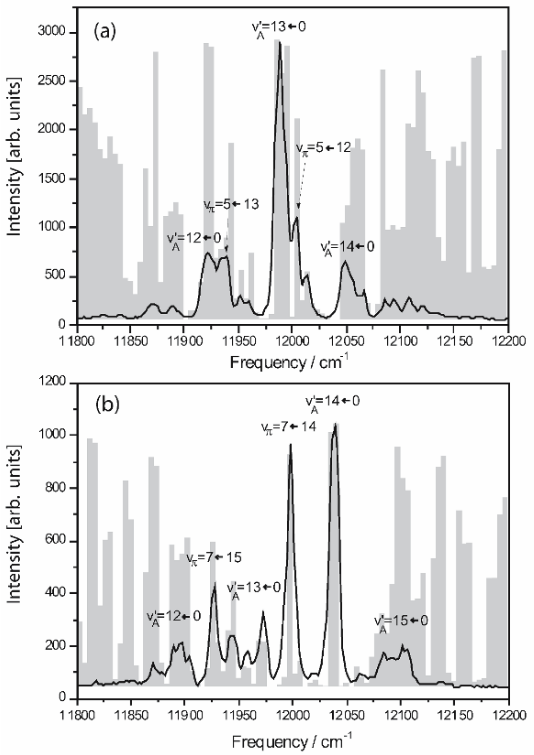

Fig. 2.42. Laser pulse spectra for maximization (a) and minimization (b) of the isotope ratio $^{39,39}K_2/^{39,41}K_2$. The gray bars denote the corresponding transmission pixel pattern of the optimized pulses. The highest peaks are assigned to transitions between particular vibrational energy levels of the different electronic states $X^1\Sigma_g^+$, $A^1\Sigma_u^+$, and $2^1\Pi_g$ of the $^{39,39}K_2$ isotope in (a) and the $^{39,41}K_2$ isotope in (b). Even indications of the mentioned distortion of the v'=13 vibrational level in the $A^1\Sigma_u^+$ state may be observable as a small peak shift, yet this cannot be firmly claimed since it is at the limit of the shaper resolution. [240]

isotope ratio at a center wavelength of 833 nm (see Fig. 2.42a) displays several distinct sharp peaks with differing intensities and intensity attenuation to almost zero between the peaks. The sharp peaks in the spectrum for minimization of the isotope ratio (see Fig. 2.42b) are located at different frequencies compared to the maximization case, shifted on average by about -12 cm^{-1}. The peaks are at positions where the spectral intensity in the maximization case is low and vice versa which predominantly accounts for the high isotope selectivity. Some peaks in the presented pulse spectra can be assigned to transitions to the estimated vibrational levels in the $2^1\Pi_g$ state (see Fig. 240b) calculated by solving the time-independent Schrödinger equation numerically for the potential curve [238]. These levels exhibit isotope shifts themselves which may enhance the achievable selectivity. This demonstrates the potential of the presented method since it is not restricted to a single transition.

In the pure amplitude optimizations it can be noticed that some of the lower frequency peaks are missing. This may be due to the strongly hindered time modulation in this case resulting in a short pulse which can be understood with the superposition of the spectral components (phase-locked). The short interaction time does not allow the wave packet to propagate far in the excited state, therefore all transitions are close to the initial position of the wave packet in the ground state. Thus, higher frequencies are required to resonantly reach the $2^1\Pi_g$ transition state within the ionization step from the $\mathrm{A}^1\Sigma_u^+$ state. Moreover, some peaks belonging to the $2^1\Pi_g \leftarrow \mathrm{A}^1\Sigma_u^+$ transition are missing. This demonstrates the significance of pulse time elongation and phase modulation for molecular wave packet dynamics leading to an enhanced variability in the ionization path. Hence, another advantage of isotope selection by phase *and* amplitude modulation compared to cw-isotope separation methods is apparent.

Without theory an accurate explanation of the complex pulse shapes visible in the XFROG traces (Fig. 2.43) cannot be given, but it is possible to extract some general aspects. The frequently obtained subpulse distance of 250 fs can be explained by a stepwise excitation whereby the excitation to the inner turning point of the $A^1\Sigma_u^+$ potential is followed by an excitation 250 fs later at the outer turning point. This interpretation is backed by the fact that the Franck-Condon window via the resonant $2^1\Pi_g^+$ state is favorable at this distance [238]. Additionally, isotope dependent constructive and destructive interferences of the generated wave packets may occur within the ionization paths, respectively, which could further improve the isotope specific ionization efficiency [241]. It would as well explain the successful optimizations observed in the phase only experiments. Moreover, oscillation periods on other excited states may play a role as well.

In order to get more insight into the involved processes the vibrationally resolved excitation transitions were calculated (assuming no time evolution) by taking the spectral pulse intensities at the determined vibrational transitions into account. This has been done by calculating the vibrational state specific populations $N_{m,n} \propto f_{m,n} \cdot I(\nu_{m,n})$, where $f_{n,m}$ are the Franck-Condon factors and $I(\nu_{m,n})$ the relative spectral intensities at each involved transition for both isotopes. For the electronic transitions the selection factors are estimated to $\mathrm{S}_{trans} = \sum_{m,n} N_{m,n}(^{39,39}\mathrm{K}_2)/\sum_{m,n} N_{m,n}(^{39,41}\mathrm{K}_2)$. This calculation provides excitation step specific information. This can be calculated to $\mathrm{R}(\mathrm{A}^1\Sigma_u^+ \leftarrow \mathrm{X}^1\Sigma_g^+) = \mathrm{S}_{max}(\mathrm{A}^1\Sigma_u^+ \leftarrow \mathrm{X}^1\Sigma_g^+)/\ \mathrm{S}_{min}(\mathrm{A}^1\Sigma_u^+ \leftarrow \mathrm{X}^1\Sigma_g^+) = 31.3$ for the first electronic excitation and $\mathrm{R}(2^1\Pi_g^+ \leftarrow \mathrm{A}^1\Sigma_u^+) = \mathrm{S}_{max}(2^1\Pi_g^+ \leftarrow \mathrm{A}^1\Sigma_u^+)/\ \mathrm{S}_{min}(2^1\Pi_g^+ \leftarrow \mathrm{A}^1\Sigma_u^+) = 1.33$ for the second. Thus it is evident that both electronic excitation steps are utilized to achieve the high selectivity, whereby the first step predominantly contributes. The ionization step from the $2^1\Pi_g$ state can be neglected for determining the optimal iso-

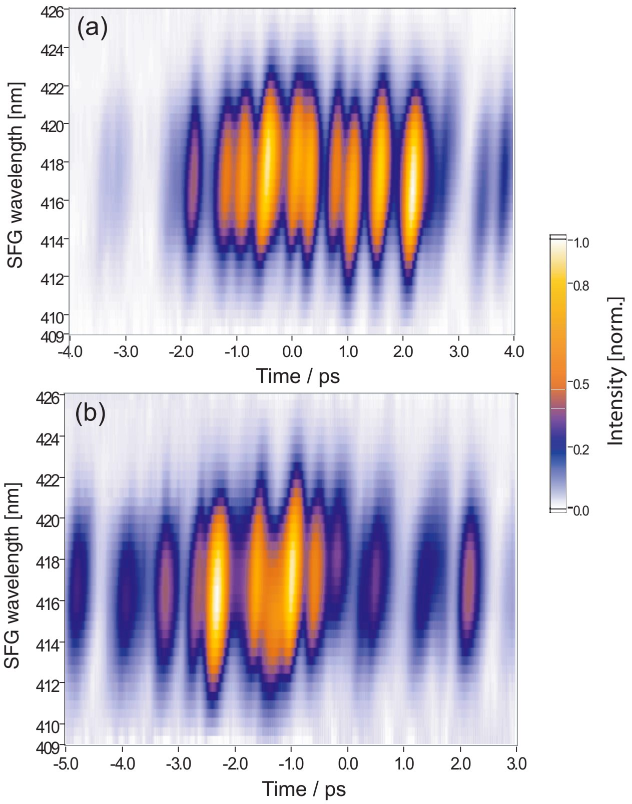

Fig. 2.43. XFROG traces for maximization (a) and minimization (b) of the isotope ratio ${}^{39,39}\mathrm{K}_2/{}^{39,41}\mathrm{K}_2$. The often observed subpulse distance of 250 fs ($\frac{1}{2}\mathrm{T}_{osc}$ of the $A^1\Sigma_u^+$ state) and the wavelength shift of up to 1 nm between two adjacent subpulses indicate a successive excitation of the electronic states on the optimal ionization path. Particularly for minimization the higher frequency subpulses assigned to the $\mathrm{A}^1\Sigma_u^+ \leftarrow \mathrm{X}^1\Sigma_g^+$ transition are followed by the lower frequency ones assigned to the $2^1\Pi_g^+ \leftarrow \mathrm{A}^1\Sigma_u^+$ transition (see Fig. 2.42b). [240]

tope selection since its transition probability is almost equal for the different isotopes. Thus, the total isotope selection calculated by $\mathrm{R} = \mathrm{R}(\mathrm{A}^1\Sigma_u^+ \leftarrow \mathrm{X}^1\Sigma_g^+)\cdot\mathrm{R}(2^1\Pi_g^+ \leftarrow \mathrm{A}^1\Sigma_u^+)$ amounts to 41.7 assuming time-independence. According to this calculation, the obtained frequency pattern accounts for a major contribution to the isotope selection. The substantial remaining difference to the experimental result can be attributed to the time evolution of the optimal pulses. The stepwise excitation process $2^1\Pi_g \leftarrow \mathrm{A}^1\Sigma_u^+ \leftarrow \mathrm{X}^1\Sigma_g^+$ with half oscillation periods in between, observed in the XFROG traces (Fig. 2.43), may account for the enhancement of the optimization factors. This can be simulated by removing spectral lines assigned to the $\mathrm{A}^1\Sigma_u^+ \leftarrow \mathrm{X}^1\Sigma_g^+$ transition (e.g. the peak v'$_A$ $= 14 \leftarrow 0$ in Fig. 2.42b) to determine the $2^1\Pi_g \leftarrow \mathrm{A}^1\Sigma_u^+$ transition factor and vice versa, which leads to an about two times larger factor in the variation of the isotope ratio. Yet, the fact that even this value is lower than the experimental result demonstrates the potential of the optimization method since all involved processes are inherently utilized to achieve the optimal yields, i.e. the above mentioned interference effects described in [241] may additionally contribute.

Isotope selective optimizations were also performed at differing center wavelengths (810 nm and 820 nm) in order to learn about the molecular system (i. e. its potential energy curves and vibrational states) and the chosen optimized ionization paths [242]. Large optimization factors between minimization and maximization of about $\mathrm{R}_{max}/\mathrm{R}_{min} = 14$ and 50 were also obtained for the center wavelengths 810 nm and 820 nm, respectively. The pulse spectra for maximization of the $^{39,39}\mathrm{K}_2/\,^{39,41}\mathrm{K}_2$ isotope ratio at the employed center wavelengths 810 nm, 820 nm, and 833 nm reveal several distinct sharp peaks with differing intensities and intensity attenuation to almost zero between the peaks (see Fig. 2.44). The most pronounced ones can be assigned to transitions from v"=0 in the electronic ground state to the vibrational states v'=12-19 of the $A^1\Sigma_u^+$ state in the $^{39,39}\mathrm{K}_2$ isotopomer.

The pulse spectra for minimization of the isotopomer ratio (see Fig. 2.44b) reveal several sharp peaks located at different frequencies compared to the maximization case. They are shifted by about -11 to -16 cm^{-1} with rising shift at rising frequency. The peaks are located at positions where the spectral intensity in the maximization case is low and vice versa which can be regarded as a major reason for the high isotope selectivity. The observed peaks can be assigned to transitions from v"=0 to v'=12-19 of the $^{39,41}\mathrm{K}_2$ isotope. The peak series at the different center wavelengths can be viewed as an extension of the first isotope optimization experiment performed at 833 nm.

Other peaks are also visible in the pulse spectra in Fig. 2.44 and may be attributed to vibrational transitions to other electronic states during the ionization path. In particular, the transition from the $A^1\Sigma_u^+$ to the $2^1\Pi_g$ state is present in the optimized pulse spectra also for 810 nm and 820 nm. The $2^1\Pi_g$ state thereby serves as a resonant transition state for the ionization step [238]. This transition occurs at the favorable Franck-Condon window at the outer turning point of the wave packet in the $\mathrm{A}^1\Sigma_u^+$ state.

In the presented K_2 experiments the employed parameters laser bandwidth, pulse duration, and liquid crystal array pixel resolution match to fulfill both, the required frequency resolution and the sufficient freedom for time evolution. For this reason K_2 is preeminently suited as a model system, but the described selection method will work for larger molecules or clusters as well. It may even be fast enough to prevent disturbance by IVR, contrary to the above mentioned technique using wave packet recurrence phenomena. When comparing the approach with conventional laser isotope separation methods, the greatest advantage is, that the broad bandwidths allow the total isotope selection of a system with all initially populated quantum states instead of

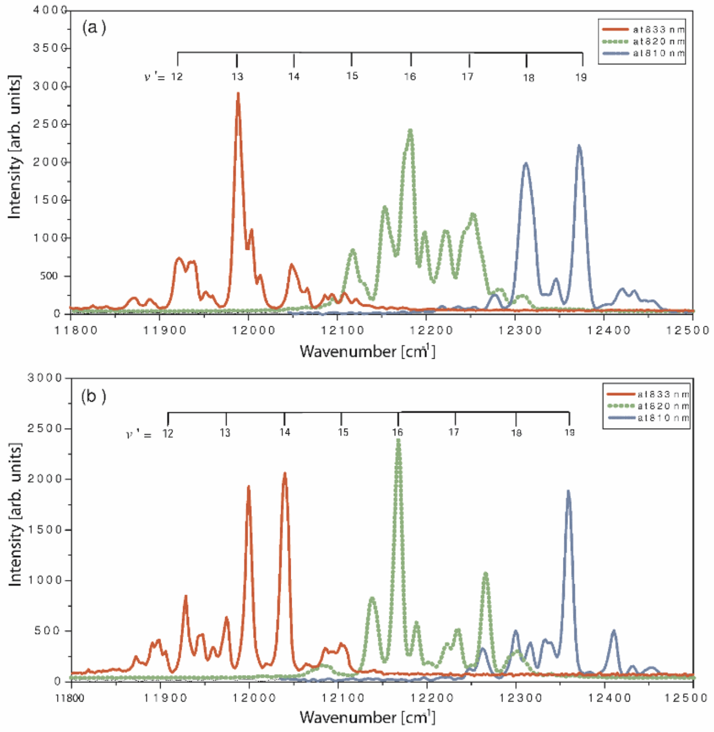

Fig. 2.44. Laser pulse spectra for maximization (a) and minimization (b) of the isotope ratio $^{39,39}K_2/^{39,41}K_2$ at different center wavelengths of the initial pulse. The highest peaks are assigned to transitions between particular vibrational energy levels of the electronic transition $A^1\Sigma_u^+ \leftarrow X^1\Sigma_g^+$ of the $^{39,39}K_2$ isotope in (a) and the $^{39,41}K_2$ isotope in (b). The vibrational series v"=0 to v'=12-19 over all measured optimized pulses is clearly visible in both spectra. [242]

only exciting a fractional single state selection by a narrow laser. Ionization is not explicitly necessary since one could as well populate selected electronic states isotope specific, which would allow isotope selection of neutral molecules/clusters.

The achieved fs-time dependent dynamics of a highly resolved frequency pattern due to superposition of the spectral components open the perspective to alternative spectroscopical treatment which combines time- and energy-resolved observations adapted to the dynamical evolution of the photoexcited system.

2.4.5.2 Theoretical aspects of the isotopomer selective ionization

in NaK

The spectroscopically rather weak differences of different isotopic species represent an excellent probe for the demonstration of selectivity power and efficiency of optimization processes. Since such experiments allow to obtain high optimization yields on selective isotopomers, this calls for deep understanding of underlying processes based on theoretical considerations.

The conceptual basis for optimal control theory to achieve the isotope selection relies on the differences of the wave packet propagation of different isotopomers and on addressing the isotope specific vibrational levels differently with a femtosecond laser field [243], as it will be illustrated below. Theoretical results for phase-only modulation will be compared with experimental pulses obtained from CLL approach and therefore the direct assignment of the processes to experimental features will be made [244].

In order to achieve an optimization of the employed laser fields with regard to controlling the isotope selective ionization in NaK, the previously outlined OCT procedure [17] has to be extended for the treatment of isotopomers. As a target function the simultaneous maximization of $(^{23}\mathrm{Na}^{39}\mathrm{K})^+$ and minimization of $(^{23}\mathrm{Na}^{41}\mathrm{K})^+$ has been considered (simulating the optimization of the isotopomer ratio) in the optimization procedure. Again, the combination of (i) electronic structure, (ii) dynamics, and (iii) optimal control considering (iv) experimental conditions will briefly be described.

(i) Investigation of photoionization processes in the energy interval of 4.83 eV corresponding to three photons of 1.61 eV used in the experiments involves the three excited states $2\ ^1\Sigma^+$, $3\ ^1\Pi$, and $6\ ^1\Sigma^+$ of neutral NaK which are resonant with one– and two–photon energies, respectively. The accurate potential energy surfaces for the ground and excited states of NaK as well as for the cationic ground state necessary for consideration of the ionization processes have been used [231] as already described for optimization of photoionization in NaK.
(ii) Quantum–dynamics simulations have been carried out by representing the wave function on a grid and using nonperturbative approach based on a Chebychev polynomial expansion of the time evolution operator as described previously. In analogy the photoionization of the single isotope of NaK, the interaction with the time dependent field involving the ground, three excited states of the neutral species and a manifold of cationic states (14) imitating the continuum, altogether 18 states for each isotopomer have been treated within the dipole approximation and using the rotating wave approximation. This is justified in the weak–field regime. The rotational motion has been neglected because of the larger atomic masses and short time scales involved.

Now, inclusion of different isotopomers involves the block diagonal extension of the vibrational Hamilton matrix in which each isotopomer is represented by a separate block including all considered electronic states.

(iii) The objective of the optimal control is maximization of the photoionization yield of one isotopomer (here $^{23}\mathrm{Na}^{39}\mathrm{K}$) while the photoionization yield of the other isotopomer (in this case $^{23}\mathrm{Na}^{41}\mathrm{K}$) is minimized at the same time. Therefore, one should introduce in the target functional in the time range $[t_i, t_f]$:

$$\begin{aligned} J = {} & \langle \boldsymbol{\psi}(t_f) | \hat{\boldsymbol{P}}_{\text{Target}} | \boldsymbol{\psi}(t_f) \rangle \\ & + \int_{t_i}^{t_f} \left[2 \cdot \mathrm{Re} \left\{ \langle \boldsymbol{\chi}(t) | - \frac{\partial}{\partial t} - \frac{i}{\hbar} \hat{\boldsymbol{H}}(t) | \boldsymbol{\psi}(t) \rangle \right\} - \lambda \frac{|E(t)|^2}{s(t)} \right] \mathrm{d}t \end{aligned} \tag{2.43}$$

with the target operator

$$\hat{\boldsymbol{P}}_{\text{Target}} = \begin{pmatrix} \overbrace{\begin{matrix} 0 & 0 & \\ & \ddots & \\ 0 & & \sum\limits_{i=0}^{19} |\nu_i^{(1)}\rangle\langle\nu_i^{(1)}| \end{matrix}}^{\text{Isotope (1)}} & 0 \\ 0 & \underbrace{\begin{matrix} 0 & 0 & \\ & \ddots & \\ 0 & & \hat{\mathrm{I}} - \sum\limits_{j=0}^{19} |\nu_j^{(2)}\rangle\langle\nu_j^{(2)}| \end{matrix}}_{\text{Isotope (2)}} \end{pmatrix} \tag{2.44}$$

The functional in (2.43) includes three terms. The first term represents the expectation value of the target operator at time t_f. The second and the third terms represent the constraints which insure that the wave function satisfies the time-dependent Schrödinger equation and limit the energy of the laser field $E(t)$, respectively. Associated with these two constraints are two Lagrange multipliers $\boldsymbol{\chi}(t)$ and λ [148]. Additionally, a sine squared shape function $s(t)$ is used. This enables smooth on and off switching of the laser field at borders of the time interval (cf. [184]).

The target operator defined in (2.44) is used to simultaneously maximize photoionization of the $^{23}\mathrm{Na}^{41}\mathrm{K}$ isotopomer and to minimize photoionization yield of $^{23}\mathrm{Na}^{41}\mathrm{K}$ isotopomer. ($\hat{I}$ labels the identity operator). It consists of two diagonal blocks (one for each isotopomer). Each block represents a 18 × 18 matrix corresponding to the considered electronic states of a given isotopomer. Its nonzero elements project onto the lowest 20 vibrational eigenstates of the cationic state. Upon variation with respect to the real and imaginary components of the laser field $E(t)$ the iterative scheme for the pulse optimization is obtained in analogy to the procedure described previously.

2.4.5.3 Comparison between theoretically and experimentally obtained optimal pulses

Experimentally, the optimization procedure is similar as outlined in Sect. 2.4.3. The ^{23}Na^{39}K/^{23}Na^{41}K ion ratio is used as fitness by sequentially recording the ion yields in time steps of less than half a second. Convergence is reached when the feedback signal does not change significantly within the following generations. The temporal intensity of the generated optimized pulse form is retrieved from the pulse spectra and the sum frequency cross correlations by using PICASO [245]. During the experiment the obtained optimization factors stay almost unchanged for repeated optimization runs [246], whereas the optimized pulse shapes may slightly differ. Therefore the best pulse under the experimental conditions was chosen for comparison with theory.

In the following, theoretically and experimentally optimized phase–modulated laser fields for the simultaneous maximization of the ^{23}Na^{39}K isotopomer and minimization of the ^{23}Na^{41}K isotopomer will be compared and analyzed. The phase–modulated pulses obtained from OCT and from experimental CLL exhibit relatively simple characteristic features and are compared in the upper part of Fig. 2.45. The experimentally shaped pulse is characterized by two dominant subpulses and theoretical results exhibit an additional dominant subpulse at later times. This is independent from the initial conditions which involve either Gaussian pulse (cf. left, upper part of Fig. 2.45) or experimentally optimized pulse (right, upper part of Fig. 2.45). For the former case also the snapshots of the wave packet dynamics for both isotopomers are presented (cf. middle, part of Fig. 2.45) and time dependent populations of the involved states (cf. bottom part of Fig. 2.45). They serve to illustrate the dynamics induced by the pulse and to deduce the mechanism responsible for the isotope selective ionization.

First the role of the dominant subpulses P_3, P_4, and P_5 for the mechanism of the photoionization is addressed. The P_3 subpulse populates the cationic state of ^{23}Na^{39}K in a direct resonant two-photon process. The ionization occurs at the outer turning point because the transition dipole moment between the first and the second excited state is much larger than at the inner turning point. At this time step, the other isotopomer ^{23}Na^{41}K is less efficient for photoionization, as can be seen from the snapshots of Fig. 2.45. The contribution of ^{23}Na^{39}K is larger because the wave packet corresponding to this isotopomer is located at the outer turning point.

Moreover, the snapshots in Fig. 2.45 show that the difference in propagation of the wave function on $2^1\Sigma^+$ state of different isotopomers is caused by dephasing of the wave packets. For example, in the case of P_3 subpulse, during propagation of the wave packet on the $2^1\Sigma^+$ state for the isotopomer ^{23}Na^{41}K toward the inner turning point the population transfer from the electronic ground state accelerates this motion. Therefore the population of the $3^1\Pi$ state and of the cationic state is reduced (cf. snapshot of the isotopomer

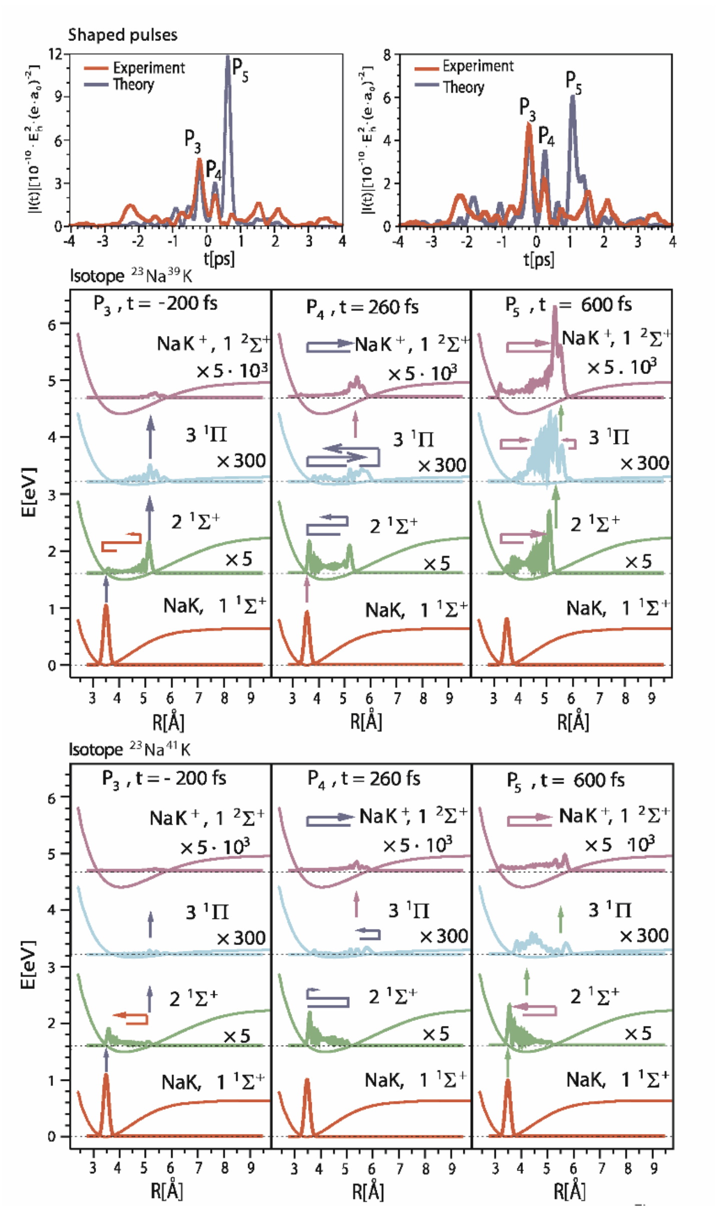

Fig. 2.45. Top: Comparison of pure phase modulated pulses for isotopomer ratio maximization obtained from OCT and from experimental CLL. The initial conditions for the theoretical optimizations involve either a Gaussian pulse (left side) or the experimentally optimized pulse shape (right side). Center and bottom: Snapshots for wave packet propagation of isotopomers ^{23}Na^{39}K and ^{23}Na^{41}K corresponding to the subpulses P$_3$ (-200 fs), P$_4$ (260 fs), and P$_5$ (600 fs) for a simulation started from a Gaussian pulse.

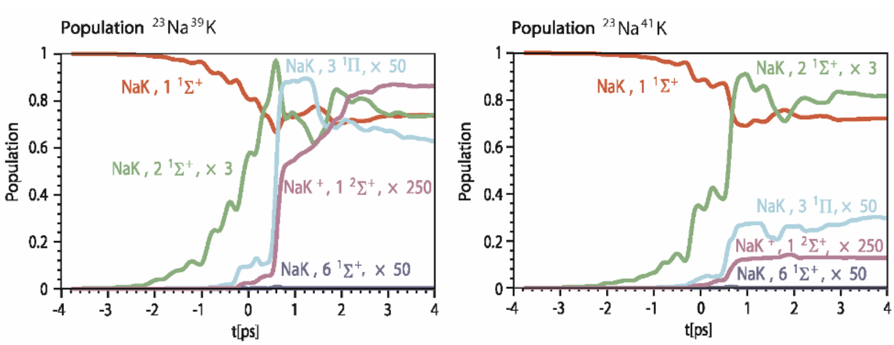

Fig. 2.46. Time-dependent populations of the participating electronic states of neutral and cationic ^{23}Na^{39}K (left) and ^{23}Na^{41}K (right) for the same initial condition.

^{23}Na^{41}K for subpulse P$_3$ in Fig. 2.45) in contrast to the situation occurring for the isotopomer ^{23}Na^{39}K at the time of P_3. After 460 fs which corresponds to one full oscillation period on the first excited state, the subpulse P_4 transfers population from the ground state to the first excited state for the isotopomer ^{23}Na^{39}K. The transfer of the population to the cationic state occurs by a sequential one photon ionization process over the second excited state which is populated by the P_3 subpulse. The subpulse P_4 introduces a sequential process for the ionization but does not increase substantially the population of the cationic state of the isotopomers (cf. Fig. 2.46).

The dominant subpulse P$_5$ strongly enhances the population of the cationic state of the isotopomer ^{23}Na^{39}K due to a direct two–photon process, which occurs very efficiently. The wave packet motion is particularly slowed down at the outer turning point. The reason for this can be depicted from the snapshots: Population as well as depopulation of the $2^1\Sigma^+$ state from the electronic ground state occurs at the inner turning point at the beginning of P_5 (cf. Fig. 2.45). Therefore, a longer residence time of the wave packet at the outer turning point occurs and this provides efficient transfer to the $3^1\Pi$ state and to the cationic state by the later part of P$_5$ subpulse. The role of the individual subpulses is also reflected by the variation of the population of cationic states as shown in Fig. 2.46. As mentioned above, P_3 and P_4 do not contribute substantially to the population of the cationic state. In addition to the important role of subpulse P_5 for the ionization of the isotopomer ^{23}Na^{39}K the later subpulses contribute with a fraction of 39% via sequential one–photon processes to the cationic population.

The maximization of the isotopomer ^{23}Na^{39}K is experimentally less efficient than in the case of OCT ($\sim$ 2 versus $\sim$ 8). This is independent from the initial conditions. Similar results and mechanism are obtained from OCT approach if the optimization has been started using experimentally shaped pulses in the frame of CLL. The reason for this can be connected with the presence of the dominant P_5 subpulse in the OCT which is responsible for efficient two–photon process. Experimentally optimized pulse has reached the solution which is characterized by only two dominant subpulses. However, their spacing is similar to those obtained by OCT showing the agreement between the experimental solution and the parts of theoretically optimized pulses.

In order to examine the conditions under which the pulse features obtained by the experimental CLL approach can be obtained, the theoretical optimization procedure was interrupted after three iterations starting from the experimental pulse shape. The obtained pulse shape is almost identical to the experimental one as shown in Fig. 2.47 which is characterized by two dominant subpulses. The time dependent populations of the involved states are shown as well. Moreover, an optimization factor of ~ 3 for the theoretical simulation is close to the experimental efficiency of ~ 2. This confirms that the parameters of the simulation were well adapted to the experimental conditions. By analyzing the snapshots, a difference in the propagation of the wave packets on the $2^1\Sigma^+$ state of different isotopomers was found, again due to photoinduced dephasing. The ionization occurs at the outer turning point due to larger transition dipole moment between the first and the second excited state.

The gained insight reveals that photoinduced isotopomer specific acceleration of the wave packets followed by ionization at the outer turning point of the $2^1\Sigma^+$ state is responsible for the isotopomer selection observed experimentally.

In summary, it should be pointed out that selective phase-optimization of ionization of ^{23}Na^{39}K isotopomer is in general due to the different isotopomer specific wave packet dynamics in the first excited state. The optimal pulse induces dephasing of initially formed wave packet leading to different spatial localization of the two wave packets at the same time corresponding to two isotopomers. This enables isotope selective ionization since only the portion of the wave packet at the outer turning point can be efficiently ionized due to the larger transition dipole moment between the first and second excited states than at the inner turning point. The pulses obtained from the OCT with different initial conditions have common leading features. This means that theoretically optimized pulses are sufficiently robust and independent from the initial conditions. Consequently the analysis of the underlying processes provides equivalent mechanisms. The subpulses which are responsible for the described mechanism are also present in the experimental findings. In this context it is interesting to note that two qualitatively different search strategies were utilized for OCT and experimental CLL, respectively. Yet, the nondeterministic evolution search strategy in CLL and the deterministic iterative search strategy in OCT provide similar results.

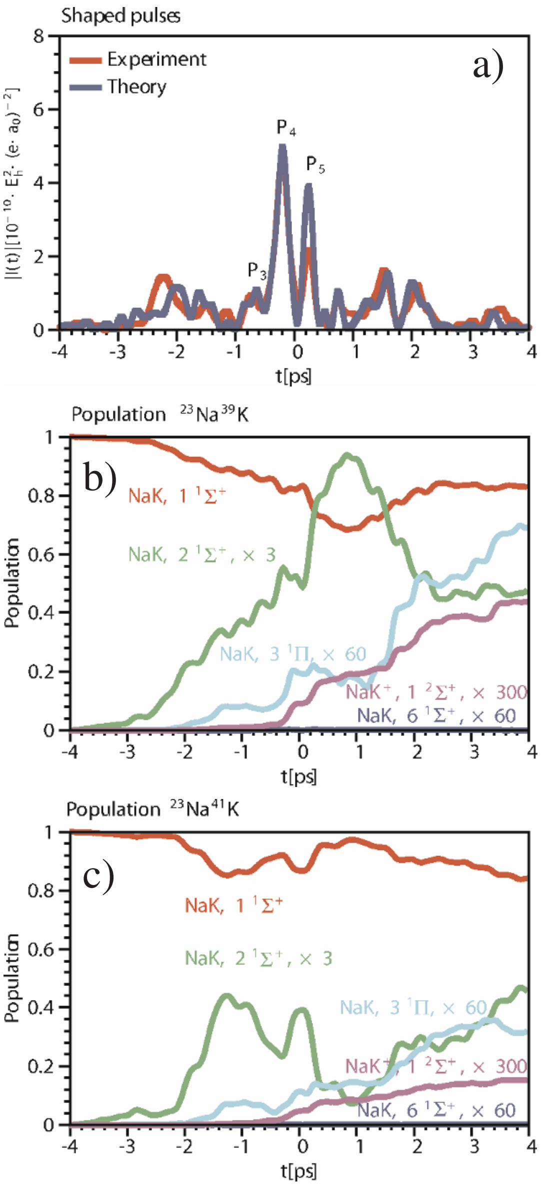

Fig. 2.47. Left: Pulse shape (blue line) obtained from a optimization started from an experimentally optimized pulse (red line) and interrupted after three iterations. Center and right: Time dependent populations of the electronic states of neutral and cationic NaK for both isotopomers.

2.4.6 Optimization procedures and their improvement

The development of pulse shapers, which allow to apply optimally shaped laser pulses in the amplitude and phase domain has opened new perspectives for driving molecular reaction dynamics in real time. An important aspect of the approach is the retrieval of the information coded in the optimized laser pulse shape which can lead to new perspectives regarding the investigation of molecular dynamics [46, 226]. This calls for systematic improvements of the method, which will briefly be presented here. One improvement of the approach examines the implementation of genetic pressure within the algorithm for performing control pulse cleaning [247]. The aim is to remove extraneous pulse features in order to expose the most relevant structures and thus reveal mechanistic insights. A second improvement on the method addresses parametric optimization [177,185,248,249] were the search space is narrowed down by introducing a few pulse parameter optimization. The suggested parameters in the time- and frequency domain are time distances, intensities, zero order spectral phases, chirps of different subpulses, and spectral peak patterns. In this manner, the relevance of certain structural features of optimal pulses can be investigated. The third approach involves the addition of the polarization as the third parameter besides phase and amplitude shaping in order to have full control over all degrees of the light field. This allows to attain new optimization paths which adds a significant degree of controllability.

2.4.6.1 Control pulse cleaning and conflicting objectives

The procedure of control pulse cleaning is targeted to remove extraneous control field features in a closed-loop quantum dynamics optimization experiment. This is accomplished by applying genetic pressure during the optimization run in order to simplify the optimized pulses and to reveal the most relevant features. Thereto, a new fitness function has to be formed where the target goal f is optimized and simultaneously genetic pressure is implemented on certain pulse components. This is solved by dividing the target f by the average spectral transmissions raised to a positive power γ, expressed as the fitness function

$$F = \frac{f}{(\frac{1}{N}\sum_{l=1}^{N} T_l)^\gamma} \tag{2.45}$$

with the transmissions T_l with $l = 1, 2, ...N$ for all $N = 128$ pixels. The weighting exponent γ can be freely chosen to set the desired degree of genetic pressure. The phase values were thereby allowed to be modulated freely without genetic pressure. This new fitness function was applied for the maximization of the ionization of NaK at a center wavelength of 770 nm. The influence of different levels of genetic pressures reveals the enhanced efficiency of the optimized pulse at strong control pulse cleaning. The comparison to a short pulse at equal energy demonstrates the successful removal of unimportant components and the enhancement of those that count [250]. Apparently,

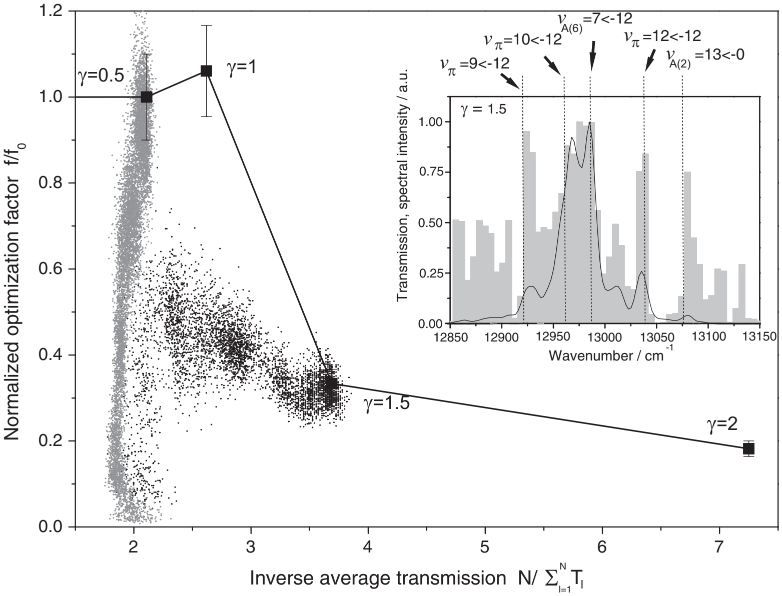

Fig. 2.48. Correlation plot of the normalized optimization factor f/f_0 versus the inverse average transmission. The solid line depicts the estimated Pareto-optimal front drawn through the optimal solutions for different γ. The optimization courses for $\gamma = 0.5$ (gray points) and γ =1.5 (black points) are shown by plotting the values of every individual. The inset shows the spectrum (solid line), and the pixel transmissions (gray bars) of the optimized pulse for γ =1.5. Vibronic transitions to the first and second excited states are denoted. The vibrational energy levels associated with these transitions were calculated by numerically solving the time-independent Schrödinger equation for the potential curves from [227]. [250]

this effect is due to the allocation of the available laser energy to the most relevant spectral features in the case of strong control pulse cleaning.

At increasing genetic pressure, features arise from the transmission spectra and become more distinct. These features can be assigned to transitions associated with vibrational levels of different electronic states of the ^{23}Na^{39}K isotopomer which underlines the multistep character of the selected ionization paths. The insert of Fig. 2.48 shows the spectrum (solid line) and the pixel transmissions (gray bars) of the optimized pulse with $\gamma = 1.5$ for the center wavelength of 770 nm. It exposes otherwise not visible vibronic transitions to the first and second excited states which come out best at this weighting factor. This demonstrates the feasibility of control pulse cleaning and shows that otherwise hidden information can be unraveled.

Fig. 2.48 depicts a correlation plot of the normalized optimization factor f/f_0 (with f$_0$ being the ion yield without genetic pressure) and the inverse average transmission $N/\Sigma_{l=1}^{N}T_l$. Both objectives are functions of the same 256 pixel settings in the modulator. Plotted is the so called Pareto-optimal front (solid line) drawn through the optimal solutions for different γ. This presentation reveals the correlation between both conflicting objectives and provides a tool to distinguish between optimal and inferior solutions. As examples, the optimization courses for γ =0.5 (gray points) and γ =1.5 (black points) are shown by plotting the corresponding objective values of every individual. Both optimizations evolve from the lower left to the upper right. While the ion yield increases at almost constant transmission for the optimization with γ =0.5, the optimization for γ=1.5 first tends to increase f/f_0 and then decreases by proceeding to lower average transition which indicates the enhanced efficiency of cleaning at the end of the optimization. This concept may be generalized to multi-criterion optimizations with several physical relevant objectives and new algorithms could be utilized where one receives the entire Pareto-optimal front within one run.

2.4.6.2 Parametric optimization

In the following, a different approach to receive further information will be applied by performing a few parameter optimization, where the search space is reduced to permit only simple pulse trains or spectral patterns. In this manner the relevance of certain structural features of the optimized pulses can be investigated. A further advantage of parametric optimization, besides search space reduction and application of physically relevant and intuitive parameters, is the possibility to define the framework of an experiment. One can for example choose a parameter set for an intended purpose and will receive the optimized result within this parameter set. Here, the question is raised what will be the result if different numbers of subpulses are allowed, which will tell the relevance of the additional subpulses. Thereto, the complex electrical field of a pulse train after passing the shaper was constructed by

$$\tilde{E}_{out}(t) = e^{i\omega_0 t}\sum_n \varepsilon_n(t-t_n)e^{i\varphi_0 t} = e^{i\omega_0 t}\sum_n \tilde{\varepsilon}_n(t-t_n) \tag{2.46}$$

with ε and $\tilde{\varepsilon}$ being the field envelope and complex field envelope of the subpulses, respectively, and t_n being the time distances between the subpulses. The resulting temporal field is then Fourier-transformed to receive an electrical field in the frequency description. The desired output for the electrical field is hence produced from the modulator by writing the filter function $\tilde{H}(\omega) = \tilde{E}_{out}(\omega)/\tilde{E}_{in}(\omega)$. The possible waveforms are limited by physical set-up issues [221] like pixel quantization, laser bandwidth, gap-to-stripe ratio, and phase resolution, leading to a maximum complexity of the pulse, to pulse replica and other side effects [251].

The experiments were performed by pure phase modulation such that $|\tilde{H}(\omega)| = 1$ in order to keep the total pulse energy constant. Due to this

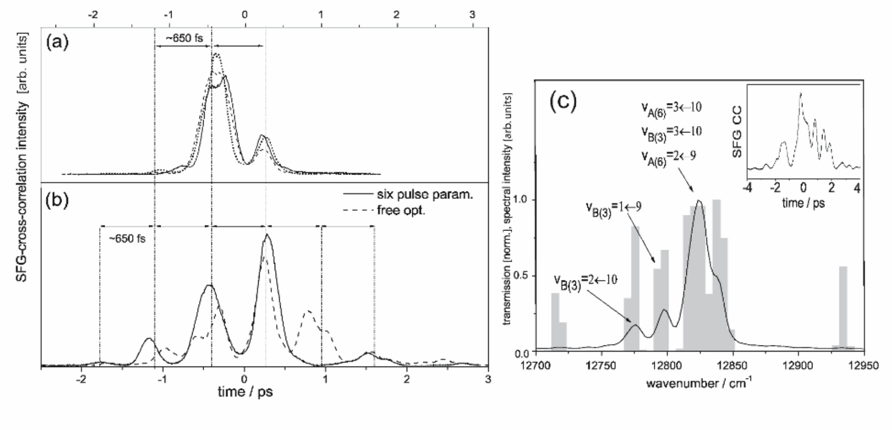

Fig. 2.49. The SFG cross-correlation results are shown for optimizing three (a) or six (b) subpulses (solid line). The results of three different runs are shown in (a). Subpulse distances of 650 fs corresponding to $1.5T_{osc}$ are visible in all cases. The optimized pulse for free optimization is shown in (b) as a dashed line. The spectrum of the optimized pulse for parameterization in the frequency domain employing 11 narrow Gaussian distributions is shown in (c) (the inset depicts the cross-correlation trace). The spectral peaks are assigned to vibronic transitions. [249]

constraint, no exact transfer function can be determined for those transformations which require a change of spectral amplitudes. A reliable algorithm is applied that approximates a desired temporal pulse shape by using a fast iterative routine [252] that implements the Gerchberg-Saxon-Algorithm [253]. The full search space was reduced to an 11 or 23 parameter space for three or six subpulses, respectively, where the subpulse distances, intensities, constant phase differences, and linear chirps between were subject to optimization. Fig. 2.49 shows the SFG cross-correlation results for optimizing three (a) or six (b) subpulses for the ionization of NaK at 780 nm center wavelength [249]. The acquired pulse forms of three different runs are presented in (a) in order to test the robustness of the optimized pulse shape. Particular subpulse distances corresponding to $1.5T_{osc}$ in the excited $A(2)^1\Sigma^+$ state can be observed for all runs. However, the optimization factor increased from approximately 1.2 for three subpulses to about 1.5 for six subpulses, which comes closer to the value of 1.6 for free optimization. This indicates that apparently more than three subpulses are required for an efficient transfer to the ionic state, which is in concordance to the above given explanation in cooperation with theory for a free phase-only optimization at 770 nm center wavelength [231]. Hence, a repeated, stepwise excitation is likely to yield better results. Allowing linear chirps to the subpulses may further enhance the ion yields. The unrestricted optimization produced a comparable waveform except for one more subpulse at around 0.8 ps. The remaining difference between the parametric and the free optimization may further originate from the search space restriction since some pulse components were still not modulated in the parametric case. Yet, this example shows the potential of the introduced method to gradually gain knowledge about the molecular system.

Another possibility is to perform spectral parameterization, where narrow Gaussian amplitude distributions are subject to modulation in order to find certain vibronic transitions. Parameters are the distances and intensities of these distributions. The phase can thereby be modulated freely to allow unrestricted temporal pulse modulation, as realized here. For the NaK model system some involved transitions could be identified as to the first and second excited state (see Fig. 2.49c). This so called transition finder can generally be applied to search for those transitions in molecular systems which are utilized by the optimized path.

2.4.6.3 Combined phase, amplitude, and polarization shaping

In the pulse shaping experiments so far only the scalar properties of the electric field were optimized and the vectorial character, namely the polarization has been neglected. Since wave functions of quantum mechanical systems are three-dimensional objects, including the polarization should increase the degree of control tremendously. At first, the group of G. Gerber created laser pulses formed in phase and polarization by simply removing the polarizer of a double array pulse shaper that is commercially available [254]. This setup allows to change the major axes ratio of the ellipse of the electric field, but for a given frequency it is restricted in the orientation of the major axes, which are fixed along the horizontal and vertical axes.

Example pulses have shown the advantages of this setup and experiments like the ionization of K_2 [255], and the ionization of aligned I_2 [256] has demonstrated the importance of the polarization in these molecular excitation processes. Recently, the limitation in the polarization modulation was overcome by passing a double array modulator and a single array consecutively [257]. This setup presented by Y. Silberberg et al., is capable to change the major axes ratio and the orientation of the major axis independently so that it features full control over phase and polarization [257].

Both setups do not yet include the amplitude as the last parameter to modulate all properties of the electric field. Recently, two setups were introduced, which allow to modulate all three parameters phase, amplitude, and polarization independently [258, 259]. In this Section, the serial setup that is shown in Fig. 2.50 is used. It presents the first implementation of all three parameters phase, amplitude, and polarization in a closed loop experiment. The main idea of the setup is the use of four liquid crystal arrays one by one, which is accomplished within a symmetrical 4f-setup that the laser pulse passes twice. Then the arrangement is combined with a feedback loop and applied on a dimer system which offers the advantage that the dipole moments are only parallel or perpendicular. The NaK system is well suited for

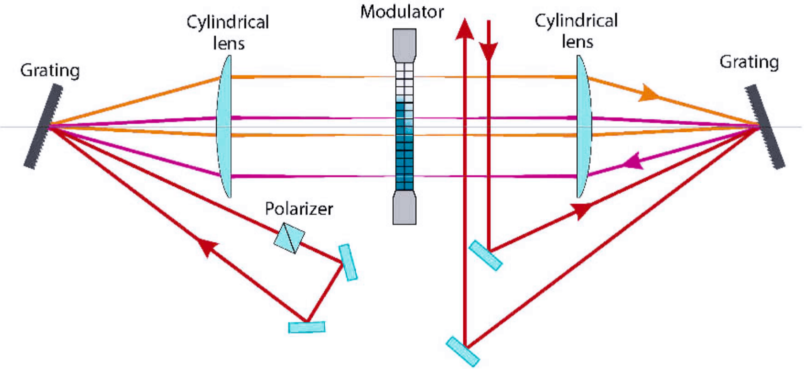

Fig. 2.50. The serial pulse shaper setup consists of a zero dispersion compressor which is passed two times. The incident laser pulse hits the first grating at a smaller incident angle, then the dispersed spectral components are focused by a cylindrical lens onto the lower half of the liquid crystal array by a combination of 800 grooves per mm of the grating and 250 mm as the focal length of the cylindrical lenses. After refocusing with the second cylindrical lens and recollimation by the second grating, this part of the modulator acts together with the polarizer as an amplitude filter. The laser pulse is redirected into the 4f setup under a larger incident angle, passes the grating and lenses and gets through the other part of the modulator. In this part of the double liquid crystal array, the phase and polarization are set and the outgoing pulse is modulated in phase, amplitude, and polarization.

this investigation since the energy potential curves are known and several optimizations were carried out, like the enhancement of multiphoton ionization [231] and isotope separation [260]. The optimizations were carried out with a central wavelength of 780 nm.

The employed pulse shaper is a zero dispersion compressor consisting of two gratings with 800 lines per mm and a pair of cylindric lenses of 250 mm focal length. The modulator has two layers of liquid crystal arrays with 640 pixels each. The setup is passed twice under different incident angles corresponding to different sectors of the modulator. In the first passage, the spectral amplitude is set by the cooperation of the polarizer and the retardances ϕ_a and ϕ_b of the first half of the double array. In the second pass, the phase and the polarization are modulated by the interplay of the retardances ϕ_c and ϕ_d of the other half of the modulator. The resulting electrical field can be written as:

$$E_{out}(\omega) = E_{in}(\omega) e^{\frac{i}{2}(\phi_a+\phi_b+\phi_c+\phi_d)} \cos\left(\frac{1}{2}(\phi_a-\phi_b)\right) \begin{pmatrix} \cos\left(\frac{1}{2}(\phi_c-\phi_d)\right) \\ i\sin\left(\frac{1}{2}(\phi_c-\phi_d)\right) \end{pmatrix} \tag{2.47}$$

As one can see, the control of the four retardances leads to a simultaneous and independent manipulation of the phase, the amplitude, and the polarization. For a difference retardance $\phi_c - \phi_d$ equal to zero the polarization stays linear in horizontal orientation, for $\pi/2$ it changes to circular polarization and for a difference of π, it is linear again but with vertical polarization. For intermediate values the electric field is elliptically polarized, whereas the helicity is determined by the sign of the difference retardances. The outcoming electrical field of one wavelength can generally be described as an ellipse with the major axes fixed in horizontal and vertical orientation.

In order to characterize the obtained pulses, they are measured with a modified SFG cross-correlation: A pivoted half wave plate turns the desired polarization component of the shaped pulse into the direction of the following horizontal polarizer and, thereby, the polarization component of interest is cut out. This takes the favored direction of the BBO-crystal into account and enables to measure every polarization direction equitable. By measuring the two orthogonal cross-correlations the temporal structure of the pulse can be measured. The corresponding spectral intensities are recorded behind a horizontal and vertical polarizer.

An evolutionary algorithm controls the parameter phase, amplitude, and polarization by setting the retardances for every pixel of the modulator during the optimizations. In this setup, the parameters are not coupled, so each component can be optimized independently. After having proven the functional capability of the serial setup within the closed loop experiment, optimizations on the $^{23}\mathrm{Na}^{39}\mathrm{K}^+$ ion yield were performed by measuring the current of the emerging ions. A phase and amplitude optimization as well as a phase, amplitude, and polarization optimization were performed. This allowed to compare the ionization efficiency and to reveal the effect of the additional polarization modulation. The learning curves of both optimizations are shown in Fig. 2.51a and depict a large enhancement compared with the ionization, in which an unshaped short pulse is used. Here one can observe the influence of the reduced search space in the higher convergence speed of the phase and amplitude optimization. The ratio obtained by the phase and amplitude optimization is 1.2 related to a short pulse. The optimization of phase, amplitude, and polarization are more efficient with a ratio of 1.8. Therefore, the additional change of the polarization within one pulse structure enhanced the ratio by another 50%.

The cross-correlation traces of the phase, amplitude, and polarization shaped pulse in Fig. 2.51b clearly shows the appearance of different polarization states within one pulse structure. The cross-correlation shows a subpulse structure with changing polarization states. As described in more detail before (see Sec. 2) the induced three-photon ionization process starts at the $A(2)^1\Sigma^+$ ground state. The population is then transferred to the first exited state which is also a $A(2)^1\Sigma^+$ state. Here the wave packet propagates until it is ionized by a resonant two photon process across the intermediate state $B(3)^1\Pi$ state. Since the dipole moment of the transition between two Σ states is orthogonal to the one of a Σ-Π transition, alternating polarization directions occur.

This demonstrates the vectorial properties of the scalar product $\boldsymbol{\mu}\cdot\boldsymbol{E}$ in the transition dipole moment operator and, thus, the orientation of the electric

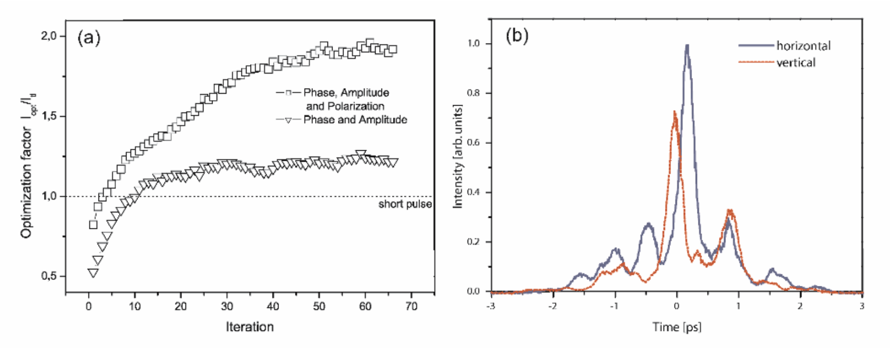

Fig. 2.51. (a) Evolution of the NaK^+ yield of each generation during the optimization, normalized to the one obtained with a transform limited short pulse (dashed line). The triangles represent the optimization of phase and amplitude, which reaches a optimization factor of 1.2. The boxes exhibits the optimization of all three parameters phase, amplitude, and polarization, ending up with a factor of 1.8. (b) Cross correlation traces of the optimized pulse shapes in horizontal and vertical orientation. The structure shows clear sub-pulses with alternating polarization states.

field respective to the dipole moment is very important. The conventional phase and amplitude shaped pulses neglect this vectorial character and only consider the Franck-Condon factors for the transition probability.

Further information arising from the cross-correlations is the distance of 660 fs between the first sub pulses. The value is consistent with the well-known oscillation time of the $A(2)^1\Sigma^+$ state achieved from pump-probe spectra [261] and the data obtained by optimizations in phase and amplitude [231]. So the algorithm enhances the ion yield by turning the polarization of each sub-pulse to the orientation parallel to the dipole moment of the transition. The distance remains constant and, therefore, the ionization process is accomplished by taking a similar path.

In conclusion, the addition of the third parameter, the polarization, improves the efficiency of the ionization compared to the phase and amplitude optimization. The analysis of the cross-correlations and the obtained spectra of the phase, amplitude, and polarization shaped pulse explains the higher optimization factors.

2.4.7 Controlling photodissociation processes

The first successful feedback control experiment of G. Gerber et al. [158] reported the optimization of distinct fragmentation channels vs. the yield of the mother ion signal of the unimolecular decay of $CpFe(CO)_2Cl$. The experimental conditions did not yet allow to decipher the underlying molecular dynamics process from the obtained optimum pulse shapes. To obtain this, experiments on simple systems were needed, which operated at significantly lower laser powers in the weak field regime, so undesired multiphotonic transitions and deformations of the potential energy surfaces could be avoided. Pump-probe experiments on Na_2K indicated this system as a suitable candidate for an optimum control experiment. As shown in Fig. 2.10 the pump-probe spectrum exhibits - superimposed on an exponential decay with a time constant of 3.28 ps - an oscillatory behavior with a period of roughly 500 fs. The exponential rise time of 3.25 ps of the fragment NaK indicates its origin from the equally fast decaying Na_2K. In the control experiment the one color pump-probe scheme is replaced by tailor-made pulse shapes optimized in suitable feedback loops. Very important in this regard is the information content, which can be acquired from this optimization process. In the case of optimizing the mother ion Na_2K^+, a double-pulse sequence is retrieved from the analysis of the autocorrelation trace [27]. The time difference between the first and second pulse is approximately 1240 fs which corresponds to 2.5 oscillation periods of the electronically excited trimer. It is known from pump-probe spectroscopy, that the photoionization of the electronically excited Na_2K molecule occurs most efficiently at this time, when the wave packet is at the outer turning point.

The channel for optimizing the NaK^+ fragment of Na_2K reaches an optimization factor of $I_{opt}/I_{tl} = 1.8$. In Fig. 2.52a and b the optimized pulse is shown in its cross correlation and SFG-XFROG representation, respectively. The pulse structure is a pulse train consisting of three main pulses with a most intense middle pulse. The time delays between the first and second pulse and between the second and third pulse are $\Delta t_{1,2} \approx 660$ fs and $\Delta t_{2,3} \approx 440$ fs,

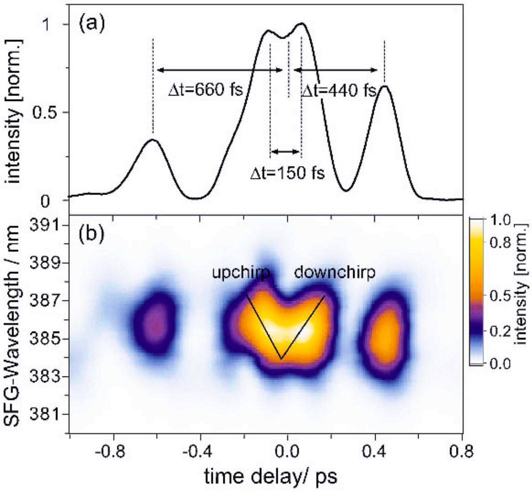

Fig. 2.52. Phase optimized control pulse optimizing the NaK^+ production in the presence of alkali trimers. (a): Cross correlation trace. The pulse train consists of three main pulses with time distances of $\Delta t_{1,2} \approx 660$ fs and $\Delta t_{2,3} \approx 440$ fs. (b) The SFG-XFROG trace reveals a substructure of the central pulse. [226]

respectively. The intensity of the central pulse is almost three times as high as that of the first pulse and twice as high as the third one leading to a sub pulse intensity ratio of 1:2.9:1.8.

With the SFG-XFROG trace in Fig. 2.52b the time evolution of the frequency components of the pulses is displayed. The central pulse reveals a pronounced positive and negative chirped twin substructure. On the red side of the spectrum the pulse is divided into two sub pulses ($\Delta t_{2a,2b} = 150$ fs) whose intensity maxima converge in a V-type shape toward shorter wavelengths. Thus, a positive chirp is followed by a negative one. The main intensity on the short wavelength side of the middle pulse marks the center of the pulse. The above mentioned pulse distances refer to this maximum. The structure of the optimized pulse form (Fig. 2.52) exhibits features of the NaK dynamics which are similar to the already discussed control pulse (Fig. 2.35) for the maximization of the NaK ionization. This is evident, because the supersonic molecular beam contains both: NaK dimers and Na_2K trimers, which cannot be distinguished mass-spectroscopically, when the trimer fragmentizes to NaK+Na. Therefore both types of NaK particles contribute to the signal: Photoionized NaK and photodissociated Na_2K. The central, most intense pulse reveals therefore a substructure which does not only correspond to the NaK dynamics, it also indicates a contribution of the fragmentation of Na_2K. This substructure can be explained by a process that circumvents the predissociative curve crossing and therefore finds a direct exit channel (see Fig. 2.53b and c): The leading red shifted part stimulates the population of the trimer down to a vibrationally excited state of the electronic ground state where due to conservation of momentum the wave packet moves in the same direction (Fig. 2.53c). The red shifted trailing part of the central pulse then excites the ground state wave packet, when it is just located beyond the curve crossing onto the repulsive potential curve of the trimer. Afterwards the third pulse ionizes the NaK fragments produced from the photodissociated Na_2K. Since this last pulse arrives after another full round trip, it can also effectively ionize the still remaining wave packet in the non-fragmented NaK, which were not yet ionized - as shown in Fig. 2.53b - by the central part of the second subpulse. Thus, also in this case the third pulse improves the ionization efficiency.

The rise in the NaK^+ yield of about 20% compared to the optimization of the pure ionization of NaK corresponds to the gain in NaK^+ determined in the pump-probe spectrum. The process delivers a convincing example for - sometimes - counterintuitive, but more efficient dynamical pathways, which can be identified by analyzing optimized pulse shapes.

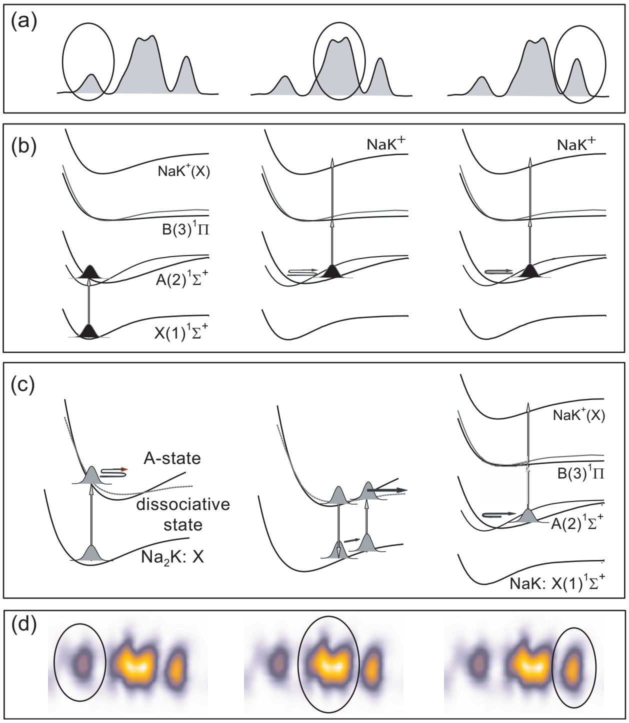

Fig. 2.53. Optimized multiphoton induced ionization and fragmentation pathways into NaK. (a): Temporal profile of the control pulse. The active subpulses are indicated. (b): Three step multi photon ionization scheme of NaK. (c): Schematic of the multi photon fragmentation of the Na_2K trimer into NaK fragments by circumventing the predissociative curve crossing. (d): SFG-XFROG traces. The active subpulses are indicated. [226]

2.5 Optimal control on ultracold molecules

C. P. Koch, A. Lindinger, V. Bonačić-Koutecký, R. Mitrić, and L. Wöste

The field of cold molecules has emerged over the last few years with many research groups working at the production of dense samples of cold and ultracold molecules [262]. Translational temperatures in these gases are below 1 Kelvin or 1 micro-Kelvin, respectively. This intense activity is motivated by many possible applications of (ultra)cold molecules which range from high precision measurements, allowing for example for the determination of a possible dipole moment of the electron as a check of the standard model of elementary particles, to the realization of a molecule laser by Bose-Einstein condensed molecular gases, or to the emergence of a new ultracold chemistry [262]. The lowest temperatures to date have not been achieved by direct cooling of the translational degrees of freedom of the molecules [263], but by first cooling atoms and then assembling these atoms into molecules [264,265]. To this end, an external field, either magnetic or optical, is applied.

Photoassociation offers the advantage of relying on optical transitions which are generally abundant. It is defined as the absorption of a photon red-detuned from the atomic line by a pair of colliding ground state atoms, creating a weakly-bound molecule in an electronically excited state, cf. Fig. 2.54 [266,267]. Series of resonances have been observed in experiments using continuous-wave (cw) lasers [266,267] which occur when the laser detuning matches the binding energy of an excited state vibrational level. In particular, excited state potentials of homonuclear dimers provide for long range molecular levels due to their scaling as $1/R^3$ at large internuclear distances R. These highly excited levels can be efficiently populated in free-bound transitions.

In order to obtain molecules in the singlet ground or lowest triplet state, the photoassociation step must be followed by a stabilization step, i.e. by a bound-bound transition. In cw photoassociation, the excited state molecules are short-lived and decay via spontaneous emission, most often through a vertical transition at large distances R, giving back a pair of atoms. However, specific mechanisms have been identified which favor radiative decay at shorter distances and allow for the creation of ground state molecules [267,268]. Stable molecules formed by spontaneous emission have been detected in a magneto-optical trap (MOT) for a number of species (e.g. [264,269,270]). These molecules are translationally ultracold, but internally highly excited.

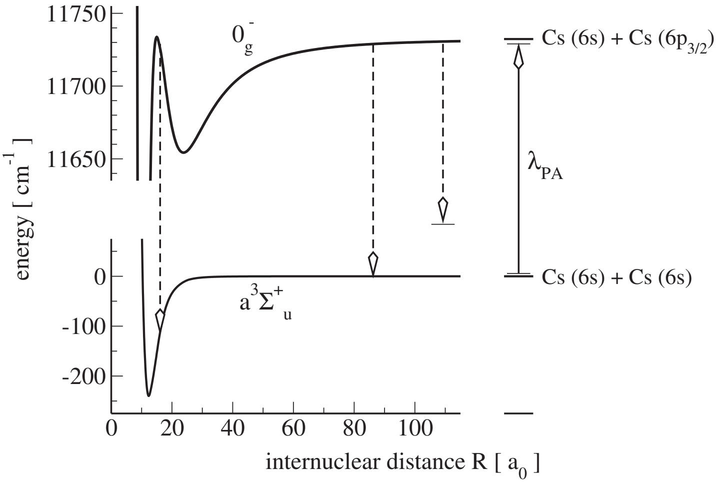

Fig. 2.54. Photoassociation: Example of two Cs atoms colliding over the lowest triplet state excited to the 0_g^- state by a cw laser λ_{PA} and ground state molecule formation via spontaneous emission (the two dashed arrows at short distances).

At this point, two possible routes for control are conceivable: (i) optimization of a *coherent* formation scheme of ground state molecules avoiding spontaneous emission, and (ii) stabilization or cooling of the internal degrees of freedom after ground state molecule formation. Both routes have been explored theoretically (cf. [271, 272] and [273]), and experimental effort toward optimal photoassociation is under way [274, 275].

2.5.1 Experimental realization of optimized molecular depletion in a magneto-optical trap (MOT)

Here, first experiments on the optimal control of excitation processes of translationally ultracold but vibrationally still very hot rubidium dimers inside a magneto-optical are presented. In order to optimize the photoexcitation of the Rb_2 molecules the employed shaped femtosecond laser pulses were optimized in feedback loops by genetic algorithms based on evolutionary strategies. As a result the irradiated molecules undergo ionization or fragmentation. The approach represents a first experimental steps toward pulsed photoassociation.

The experimental setup is shown in Fig. 2.55. About 10^7 ^{85}Rb atoms are captured in the MOT at a density of 10^{10} atoms/cm^3 and temperatures of 100 μK. In this environment diatomic rubidium molecules continuously form due to either three body collisions or light assisted two-body

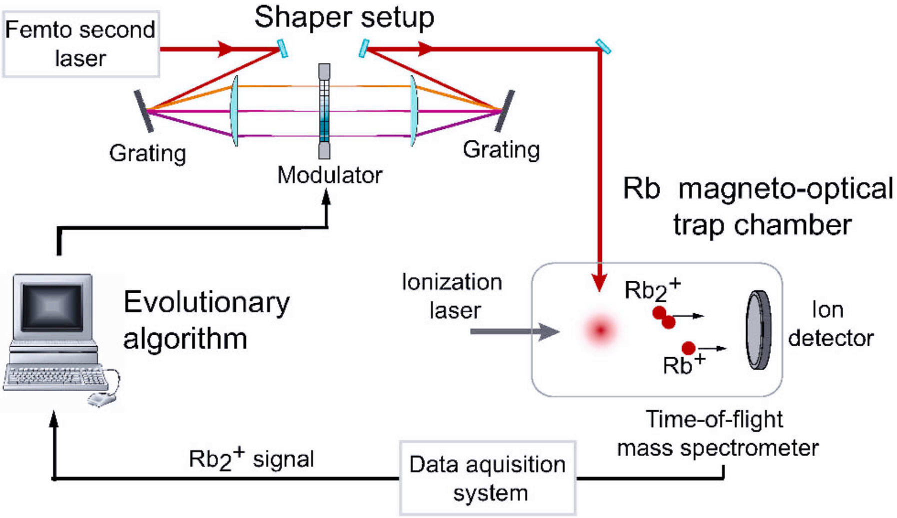

Fig. 2.55. Experimental setup for iterative closed-loop maximization of ultracold Rb_2 excitation from the ground electronic singlet or triplet states by shaped femtosecond laser pulses. The ultracold molecules are formed in a magneto-optically trapped gas of rubidium atoms. Their abundance is evaluated by monitoring the RTPI-signal of Rb_2^+.

collisions of trapped Rb atoms. They populate predominantly the highest vibrational states below the dissociation limit in the triplet electronic ground state [276, 277]. These Rb_2 molecules, which are no longer trapped by the MOT, are then detected via resonant two photon ionization (RTPI) and time-of-flight mass analysis. The RTPI laser operates at 15 Hz between 600 and 610 nm and at a pulse energy of 20 mJ. In the steady state of molecule formation and loss a maximum count rate of 0.5 Rb_2^+ molecular ions per laser pulse is observed.

For the experiments the fs-laser is tuned in the range between 780 and 820 nm. To study the laser pulse interaction with rubidium molecules, the atomic resonance components were removed from the pulse spectrum by a notch filter, realized by a physical block in the shaper's Fourier plane. In this way atomic losses from the MOT could be reduced below the detection threshold.

The rubidium dimers interact with the fs-laser pulses over the entire accessible range of central wavelengths from 780 nm to 820 nm. As shown in Fig. 2.56, the molecular signal decreases rapidly at small pulse energies and levels off to 25% at a pulse energy of 0.6 nJ. As only molecules in the electronic ground state are detected, the signal reduction can be attributed to excitation by the fs-pulses. The process can be modeled by a simple rate equation for the number of ground state molecules:

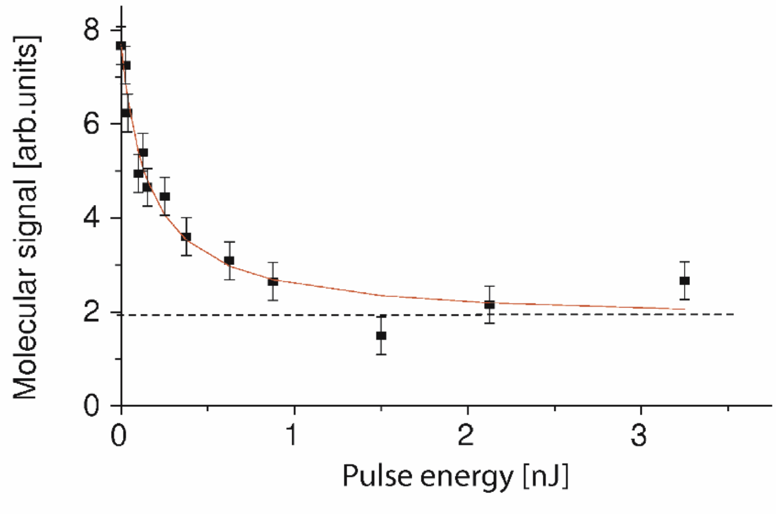

Fig. 2.56. Reduction of the Rb_2^+ molecular ion signal as function of transform limited femtosecond pulse energy. The pulses have a central wavelength of 800 nm and 10 nm FWHM. The D_1 atomic resonance at 795 nm is filtered out of the pulse. The RTPI laser is set to 602.6 nm. [274]

$$\frac{dN_{Mol}}{dt} = -R_{fs}N_{Mol} - R_{loss}N_{Mol} + R_{PA}N_{At}^2 \qquad (2.48)$$

where R_{fs} is the excitation rate by the fs-laser, R_{loss} the molecular loss rate from the detection volume and R_{PA} the production rate of molecules from trapped atoms. In the steady state where $\frac{dN_{Mol}}{dt} = 0$ and assuming that R_{fs} is proportional to the fs-laser intensity the dependence of N_{Mol} on this intensity is of anti-proportional character:

$$N_{Mol} \sim \frac{R_{PA}N_{At}^2}{R_{loss} + \alpha I_{fs}} \qquad (2.49)$$

where α is a proportionality constant. The curve in Fig. 2.56 represents a fit to the data based on this model. A model assuming a quadratic or higher order dependence of the excitation rate on intensity could not fit the data. This indicates that, in this regime of pulse energies, the interaction with the molecules has the character of an effective one-photon excitation [278].

According to [276], the molecules in the MOT initially populate the highest levels in the $\mathrm{a}^3\Sigma_u^+$ state. Due to selection rules and Franck-Condon factors, they are preferably excited to the 0_g^- and 1_g $5\mathrm{s}5\mathrm{p}_{1/2}$ states (see Fig. 2.57). Emission back to the electronic ground state could only lead to signal reduction if the vibrational level population moves out of the excitation window of the ionization laser. However, scans of the detection laser with and without fs-beam show reduced but qualitatively similar spectra which should not

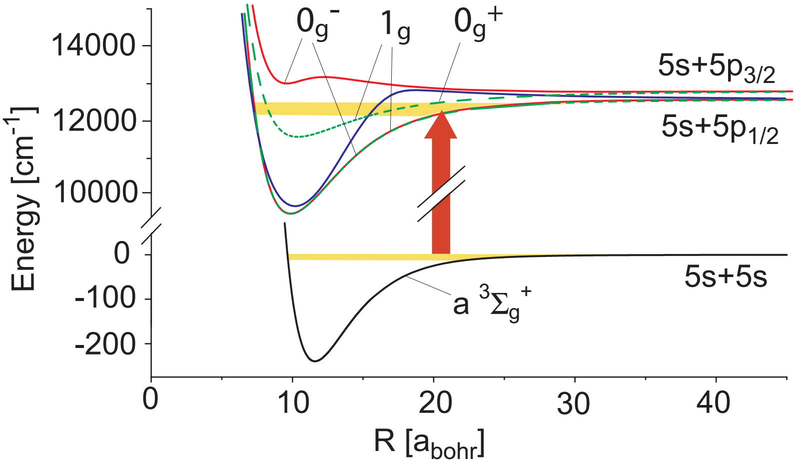

Fig. 2.57. Potential curves of the rubidium dimer including spin-orbit interaction. Initially, the molecules are expected to populate the highest levels in the $\mathrm{a}^3\Sigma_u^+$ state [276, 277]. The molecular excitation by the femtosecond pulses is indicated by the arrow. The shaded areas show the initial and final distribution of molecular vibrational states. [274]

be the case for a vibrational redistribution. Instead it can be expected that excited molecules absorb further photons, so the whole process of molecular loss can be regarded as a resonance enhanced multiphoton excitation, followed by dissociation, predissociation or ionization. This happens either within one pulse, or, as the laser repetition rate is comparable to the lifetime of the first excited state, it occurs in the subsequent pulse. At high energies all molecules in the laser focus are excited or dissociated and the residual signal in Fig. 2.56 is due to molecules which did not interact with the femtosecond laser, indicated by the dashed line. This shows that most of the molecules are produced within a small volume inside the MOT which is consistent with the picture that they form at the MOT center where the atom number density is at its maximum [279].

In order to demonstrate the practical applicability of coherent control concepts to ultracold molecules, the Rb_2^+ signal acts as an input for the self-learning optimization algorithm which autonomously programs the pulse shaper in a closed loop experiment. The algorithm is based on evolutionary strategies, it is described in detail in [280]. Due to the small molecular ion count rate the signal is averaged over 128 RTPI laser pulses for each individual of the algorithm. In order to reduce the search space for the learning algorithm a mixed scheme of parametric amplitude and free phase optimization was chosen. So the algorithm tries to find the optimal pulse shape under the restriction that only a few sharp spectral peaks contribute to the pulse shape. During an optimization the parameters of these peaks, their spectral positions and amplitudes, are altered to find the best fitting excitation pulse. Moreover, the phase was optimized freely in order to allow a temporal modulation of the pulse.

The goal of the adaptive algorithm was to minimize the molecular RTPI signal. For each iteration the ion signals corresponding to the best and worst individuals are recorded together with the mean fitness of the whole generation. As depicted in Fig. 2.58a, all three signals decrease during the particulate optimization to about 70% of the initial value after 20 iterations. The spectra of the final best individuals of two successive runs shown in Fig. 2.58b display several peaks which coincide in some but not all spectral positions. The frequency span of the fs-pulse supports an assignment of the excitation to the 0_g^- and 1_g $5\mathrm{s}5\mathrm{p}_{1/2}$ states (see Fig. 2.57). By comparing the excitation yield of the best individuals with transform-limited pulses of the same energy it is observed that the optimized pulse excites the molecules on average 25% more efficiently, which demonstrates the feasibility and potential of adaptive control.

The observed excitation enhancement can be attributed to an increased spectral intensity at particular molecular resonances found by the evolutionary algorithm. Starting from a narrow band in the $\mathrm{a}^3\Sigma_u^+$ state [276,277], molecules are excited into bound states below the D_1 resonance. By shifting the peak positions, the algorithm finds transition frequencies from this band to certain vibrational states, thereby sharing the pulse energy more efficiently than a

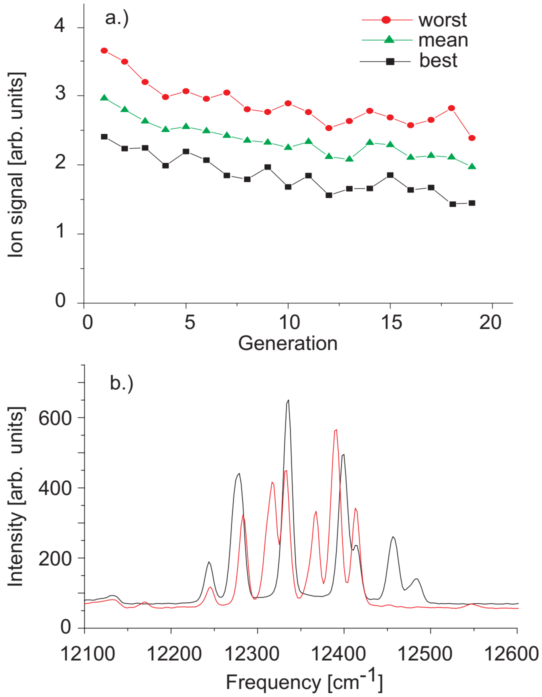

Fig. 2.58. (a) Molecular ion signal resulting from the best, the worst and the mean individual of the population for each generation during a closed loop experiment. (b) Femtosecond laser pulse spectrum of the final best individuals of two successive optimization runs under equal conditions with similar final optimization result. [274]

broad Gaussian pulse. The algorithm therefore has a large number of possible solutions to choose from and so the final pulse shapes after the optimization are not identical. In the spectral region between 12000 and 12500 cm^{-1}, the vibrational level separation is about 10 cm^{-1} in the 0_g^- and 1_g 5s5p$_{1/2}$ states, respectively. The high density of states also explains the limited potential of the optimization because the optimization factor depends on the chosen peak-width which is limited by the shaper resolution. The Franck-Condon factors may also be relevant for the excitation process since they differ for different vibronic transitions and favor particular frequencies which are enhanced in the experimentally acquired spectra. Yet, as the initial ground state population distribution in the vibrational states is not accurately known, no quantitative treatment or assignment can be made yet.

2.5.2 Theoretical proposals for ground state molecule formation via short-pulse photoassociation

Photoassociation with short laser pulses has first been discussed by Machholm et al. [281] for Na_2. Considering the timescales of the ultracold collisions, the excited state vibrational dynamics and spontaneous emission, the use of pulses of picosecond duration was suggested. Such pulses allow for small detunings, i.e. for excitation at long range where the free-bound transition matrix elements become large. Due to the high density of excited state vibrational levels at small detuning, the spectral width of a picosecond pulse comprises several vibrational levels, such that a spatially localized wave packet at large R is formed. Subsequentely, Korolkov et al. [282, 283] and Backhaus et al. [284] investigated photoassociation of OH and HCl, respectively.

Vala et al. considered photoassociation of ultracold atoms with *chirped* picosecond pulses in order to achieve adiabatic transfer, and hence complete population inversion, for a range of internuclear distances R [285]. This has led to the notion of the photoassociation window [286]: The resonance condition for the carrier frequency determines the Condon point R_C, and the finite spectral width of the pulse is transferred into a finite spatial range around R_C. Within the photoassociation window, adiabatic population transfer is possible. Luc-Koenig et al. realized that in addition to improving the excitation rate, chirping a pulse offers the possibility of wave packet shaping since the sign of the chirp controls the wave packet dispersion [286, 287]. For a positive chirp, small frequencies precede larger ones. Therefore vibrational levels with larger binding energy and smaller vibrational period are excited before those with small binding energy and long vibrational period, i.e. the wave packet dispersion is increased as compared to a transform-limited pulse. For a negative chirp, the opposite is the case, and the wave packet dispersion can be minimized. In particular, the strength of the chirp can be chosen such that the wave packet becomes spatially focused at the inner turning point of its vibrational motion. The optimal chirp is easily obtained in terms of the vibrational energies of the levels which are resonantly excited within the bandwidth of the pulse [287].

The spatially focused excited state wave packet which is obtained by a negative chirp represents an ideal intermediate in a coherent two-color pump-dump process to form ground state molecules [271]. The scheme is depicted for photoassociating two cesium atoms colliding via the lowest triplet potential to the $0_g^-(P_{3/2})$ excited state in Fig. 2.59. In this example, the central frequency is detuned by $2.7\,\mathrm{cm}^{-1}$ from the atomic resonance leading to a Condon point of $R_C \sim 90\,a_0$. The spectral bandwidth of this pulse is about one wavenumber corresponding to a transform-limited full-width at half-maximum (FWHM) of 15 ps. The photoassociation pulse, depicted in blue, depletes the ground state population within the photoassociation window, cf. the initial scattering wave function (red solid line) and the ground state wave function after the pulse (blue dashed line). It creates a time-dependent wave packet in the excited

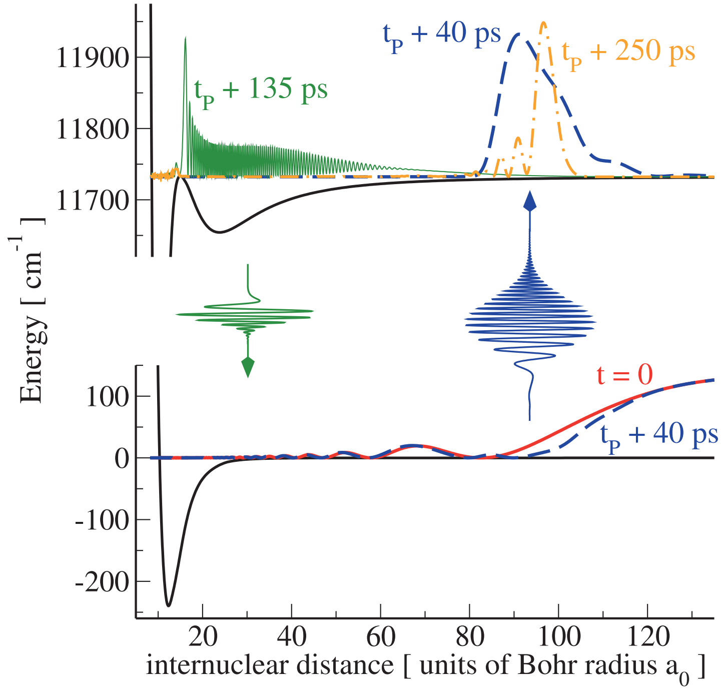

Fig. 2.59. Ground state molecule formation in a coherent pump-dump scheme for the example of photoassociation to the Cs$_2$ $0_g^-(P_{3/2})$ state, t_P denotes the time at which the photoassociation pulse has maximum amplitude (reprinted from [271]).

state which consists of about 15 vibrational levels and which moves under the influence of the excited state potential. For optimally chosen negative chirp, a spatially focused wave packet at the inner turning point (thin green line) is obtained after half a vibrational period. After a full vibrational period, the wave packet is found at its outer turning point, the position where it was created (yellow dot-dashed line). The dynamics of the excited state wave packet can be employed to optimize ground state molecule formation by a dump pulse, which is applied delayed in time after the photoassociation pulse (green pulse in Fig. 2.59): The transition matrix elements $\langle\varphi_v^g|\mu|\Psi(t)\rangle$ between the excited state wave packet $|\Psi(t)\rangle$ and all bound ground state levels $|\varphi_v^g\rangle$ show a pronounced maximum for a pump-dump delay of half a vibrational period, i.e. when the wave packet is focused at its inner turning point [271].

The $0_g^-(P_{3/2})$ state chosen for this example is particularly favorable. It results from a mixing of the ${}^3\Pi_g$ and ${}^3\Sigma_g^+$ states due to spin-orbit coupling. At long range, the ${}^3\Pi_g$ (${}^3\Sigma_g^+$) potential goes as $+C_3/R^3$ ($-2C_3/R^3$). Due to the combination of different signs and different weights, a purely long-range well appears in the $0_g^-(P_{3/2})$ potential. For Cs$_2$ this leads to a double-well structure, while for the other homonuclear alkali dimers the inner well occurs at energies far above the dissociation limit and only the long-range outer well is bound. The inner part of this long-range well is softly repulsive ($-1/R^3$) as compared to the hard repulsive walls of all other potentials. Therefore the wave packet motion is slowed down such that the wave packet spends a considerable amount of time at the inner turning point (about 5 ps in the example of Cs_2). This time window determines the resolution of the pump-dump delay which is required in order to hit the wave packet at the optimal moment, when it is focused at the inner turning point.

The specific case of cesium offers an additional advantage: The inner part of the $0_g^-\,(P_{3/2})$ long-range well is located at fairly short distances ($R \sim 15\,a_0$). The dump pulse therefore induces a vertical transition into levels with considerable binding energies ($\sim 100\,\mathrm{cm}^{-1}$, see also Fig. 2.54) [271]. In the case of $\mathrm{Rb}_2\ 0_g^-\,(P_{3/2})$, much smaller binding energies of about $5\,\mathrm{cm}^{-1}$ can be expected.

An alternative route toward formation of ground state molecules is provided by the mechanism of resonant spin-orbit coupling [268, 288] which occurs for example in the $0_u^+(P_{1/2})$ state of rubidium and cesium but also in heteronuclear alkali dimers [270]. The $0_u^+(P_{1/2})$ state results from the mixing of the $A^1\Sigma_u^+$ and $b^3\Pi_u$ states and shows an avoided crossing with the $0_u^+(P_{3/2})$ state at short internuclear distance ($R \sim 10\,a_0$ in the case of Rb_2), i.e. the spin-orbit coupling modifies the potentials, and hence the vibrational spectrum over a large range of energies and not only close to the dissociation limit. Consequently, resonantly perturbed vibrational wave functions are observed which exhibit large amplitude at the outer turning points of both diabatic potentials. They are compared to almost regular vibrational wave functions which also occur in the spectrum shown in Fig. 2.60. The outer peak of the resonantly perturbed wave functions allows for large free-bound transition matrix elements and hence an efficient photoassociation step while the inner peak facilitates stabilization to bound levels of the ground state. It is therefore expected to provide a suitable route for a pump-dump scheme [272]. In such a scenario, the photoassociation (pump) pulse should be red-detuned with respect to the D_1 line, i.e. the $nS + nP_{1/2}$ dissociation limit. The detuning should be as small as possible to take advantage of the large free-bound transition dipole matrix elements close to the atomic resonance. On the other hand, the pulse should not contain frequencies exciting the atomic resonance. For photoassociation of Rb_2 and transform-limited pulses with FWHM of a few picoseconds, the optimum detuning was identified to be 4-10 cm^{-1}. The dump pulse will then yield *singlet* ground state molecules with binding energies on the order of $10\,\mathrm{cm}^{-1}$ [272] providing an excellent starting point for a further stabilization to obtain molecules in their absolute rovibronic ground state.

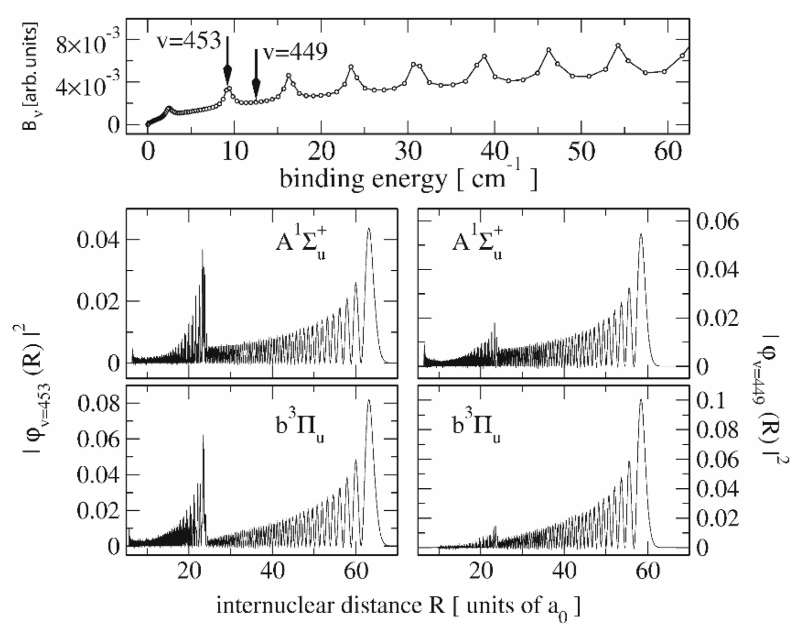

Fig. 2.60. Vibrational wave functions of the 0_u^+ states: resonantly coupled (left) and regular (right).

2.5.2.1 Molecular wave packet localization by pump-probe experiments in a MOT

A further step toward the synthesis of translationally and vibrationally ultracold molecules was achieved by pump-probe experiments in which pump wavelengths of transform-limited fs-pulses around 800 nm were used, while the system was probed with corresponding pulses around 500 nm. The results show clear indications of wave packet oscillations probably in the first excited state of rubidium dimers, with oscillation periods depending on the red detuning from the atomic D_1-line, as it will be published soon. These wave packet oscillations occur in particular excited state potential energy curves and are associated with certain nuclear distances where the initial excitation takes place. This first evidence for wave packet localization in a MOT raises hopes for the control of these wave packets with shaped laser pulses, namely to cool the system down. By using linear chirps for the pump pulse a modified response of the system was observed. The next evident step will be the application of optimally shaped laser pulse sequences aiming toward the maximum production of Rb_2 molecules by photoassociation. Afterwards the same pulse sequence will cause internal vibrational cooling cycles by photoinduced population transfer via an intermediate state. This requires high atom densities, which can be achieved by a DarkSPOT. Further relatively long laser pulse sequences in the ps range combined with a high spectral resolution will be required to allow the efficient excitation of long range potentials.

2.5.3 Theoretical aspects of vibrational stabilization and internal cooling

Vibrational cooling starts from an ensemble of molecules in different vibrational states. It requires a dissipation mechanism to dispose of energy *and* entropy. If the molecules have been formed via a magnetic Feshbach resonance or by photoassociation pulses with narrow bandwidth, a single vibrational level is populated. In this case, it is not necessary to *cool* the internal degree of freedom, but a coherent state-to-state transfer to the vibrational ground state is sufficient to stabilize the molecules. The energy of the molecule is carried away by the light, while the entropy remains unchanged. This is not just a technical point: Coherent stabilization is much easier to achieve than true cooling, since there are only a few dissipation mechanisms available in a dilute gas, and the overall cooling rate is usually limited by the time scale of dissipation [289–291].

The same consideration holds if the molecules are produced by photoassociation pulses with broad bandwidth, provided the formation is followed quickly by the stabilization step. In this case, the molecule can still be described by a coherent wave packet which serves as initial condition for the stabilization.

Vibrational stabilization of ultracold molecules using optimal control theory was first investigated for the sodium dimer, cf. Fig. 2.61 [273]. The starting point was one of the last bound levels of the Na_2 singlet ground state, and

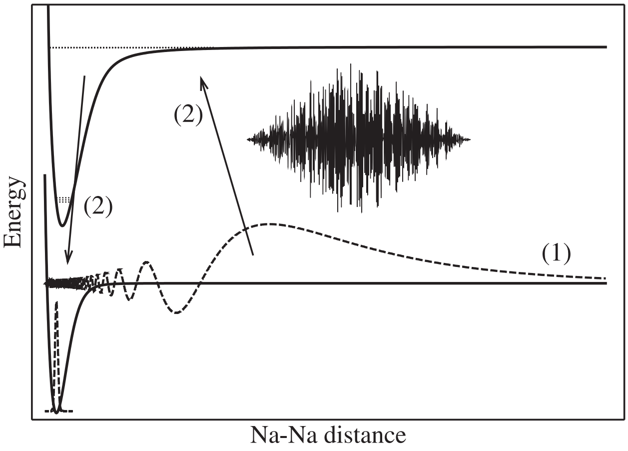

Fig. 2.61. Vibrational stabilization to transfer translationally cold, but internally highly excited molecules to their vibronic ground state using short, shaped laser pulses (reprinted from [273]).

the vibrational ground state was reached by many Raman-type transitions through the $A^1\Sigma_u^+$ first excited state. No direct Franck-Condon route exists since the overlap matrix elements of the initial and the target state with the vibrational levels of the first excited state occur in clearly disjoint spectral regions (the position of these excited state levels is indicated by lines in Fig. 2.61). It is therefore not possible to 'guess' pulses yielding a satisfactory transfer efficiency, and optimal control theory becomes imperative.

The Krotov method with the constraint to minimize the pulse energy was utilized [273]. Solutions with transfer efficiency close to one were found for the whole range of the vibrational spectrum. However, for very highly excited vibrational levels fairly intense pulses were required, and the spectrum of the optimal pulses turned out to be extremely broad. A restriction of the spectral bandwidth could not be found within the currently available algorithms. Both a constraint in time-domain to restrict the bandwidth to that of a reference field as well as filtering in frequency domain similar in spirit to [292] failed to efficiently confine the spectrum [273]. It was concluded that a new, joint time-frequency approach is necessary to impose constraints on the spectrum.

2.5.3.1 Photostabilization of ultracold Rb_2 molecule by optimal control theory

The aim of this Section is to establish conditions under which the efficient population of the ground state vibrational level $v = 0$ can be achieved and conditions under which this can be experimentally realized. So the application of full quantum optimal control to the photostabilization of the Rb_2 molecule is presented, which includes the ground electronic state ($1\ 0_g^+(I)(^1\Sigma_g^+)$ state) and two excited states ($1\ 0_u^+(I)(^1\Sigma_u^+)$ and $0_u^+(II)$ $(1\ ^3\Pi_u)$) based on accurate potential energy curves and accounting for the spin–orbit coupling.

Since primarily the stabilization and not the photoassociation process itself is addressed, a highly vibrationally excited bound state slightly below the dissociation limit in the ground electronic $1\ 0_g^+(I)(1\ ^1\Sigma_g^+)$ state is chosen as a starting point. The photoassociation starting from the unbound scattering states at large distances has already been studied theoretically [272].

It is demonstrated that the fully optimized laser pulse drives the system into the ground vibrational state of Rb_2 with nearly 100 percent efficiency. However, the spectral range of the optimized pulse is rather large. Therefore, different constraints are introduced and their efficiency in the context of possible experimental realization is examined.

Potential energy curves for Rb_2 have been previously reported on different levels of theory [293–295]. Both all-electron relativistic studies [295] as well as effective core potential calculations in the framework of the multireference configuration interaction (MRCI) methods [293, 294] were able to produce accurate potential energy curves and spectroscopic constants which are in good agreement with the experimental values.

Since the aim is to carry out quantum dynamical simulations and optimal control of photostablization, in addition to potential energy curves, also the transition dipole matrix elements between involved electronic states are needed. Therefore, a new set of data was produced employing the multireference configuration interaction method (MRCI) with two active valence electrons. This approach is computationally less demanding than those reported in [293–295] and provides sufficiently accurate results. The lowest electronic states of the Rb_2 molecule were considered which dissociate into the 5^2S+5^2S or 5^2S+5^2P atomic states. Due to considerably large spin–orbit splitting between the $5^2P_{1/2}$ and $5^2P_{3/2}$ states of the Rb atom ($\Delta E_{SO} = 237$ cm^{-1}) it is mandatory to include spin–orbit effects in the calculations. Therefore, a [9s9p6d1f] uncontracted atomic basis set [293] was employed together with a nine electron relativistic effective core potential including the spin–orbit operator ($9e^-$–RECP–SO) [296] and the Stuttgart group core polarization potential (CPP). The eigenfunctions of the total electronic Hamiltonian including spin–orbit coupling were obtained by diagonalizing the matrix representation of the $\hat{H}_{el} + \hat{H}_{SO}$ operator. For this purpose, all singlet and triplet electronic states which dissociate into the 5s + 5s and 5s + 5p atomic states are taken into account. These eigenfunctions have been subsequently used to calculate the transition dipole moment matrix elements between the involved states.

The wave packet propagation has been carried out by numerical solution of the time-dependent Schrödinger equation using the Chebychev expansion of the time evolution operator [297]. Optimal control of photostabilization has been performed in the framework of the Kosloff–Rice–Tannor optimal control scheme [17]. Both have been outlined previously.

The aim of the optimal control is to maximize the population of the vibrational ground state ν=0 and therefore to define the target functional at a specified final time t_f as the projector operator for the desired vibrational state.

Quantum dynamical simulations were performed in the manifold of three electronic states which are eigenstates of the spin–orbit Hamiltonian. The are labeled by $0_g^+(I)$, $0_u^+(I)$ and $0_u^+(II)$ and are shown in Fig. 2.62. Transition dipole moments between the ground state ($0_g^+(I)$) and two excited states ($0_u^+(I)$ and $0_u^+(II)$) are shown in the insert of Fig. 2.62. For large distances transition dipole moments converge to the values for the isolated Rb atom. However, at the distance of about ~ 5 Å abrupt change of the transition dipole moments occurs due to the change of the spin character of involved states at the avoided crossing. For smaller distances the $0_u^+(I)$ and $0_u^+(II)$ states have dominantly triplet and singlet character, respectively. At the avoided crossing, the character of the states is reversed which is then reflected in the reversal of transition dipole moments values.

The optimal control of photostabilization has been performed starting from a bound vibrational state (ν=130) which is about 5 cm^{-1} below the dissociation limit of the ground state ($0_g^+(I)$). This state has been selected since it has an outer maximum at 20 Å which lies already in a flat part of the

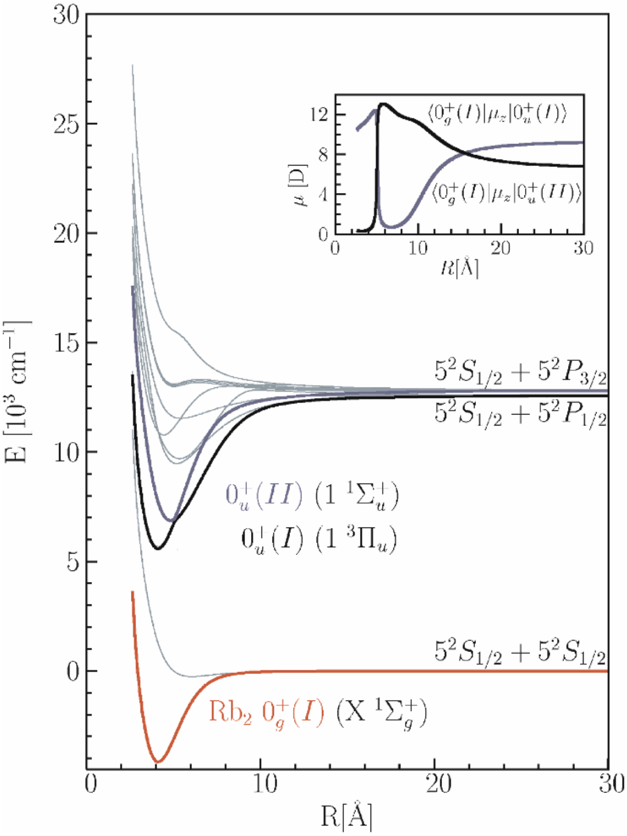

Fig. 2.62. Calculated potential energy curves for electronic Ω states of Rb$_2$. The states which are included in the quantum dynamics simulation are shown in red, blue and black lines. The insert shows the variation of the transition dipole moment between the ground state $0_g^+(I)$ and the $(0_u^+(I)$ and $0_u^+(II))$ states. The region around the avoided crossing between the $(0_u^+(I)$ and $0_u^+(II))$ at which the spin character of the states changes is marked by a lens.

potential and thus mimics the state created by the photoassociation process. Since the aim is to populate the (ν=0) state, the target operator is defined as the projection operator on the vibrational ground state. The time interval for the optimization is 15 ps since further reduction of the optimization time leads to significantly lower populations of the target state. Therefore it can be expected that the experimental realization will also require shaped pulses in a similar temporal range.

It should be pointed out that for successful optimal control, using electric fields of moderate intensity as it is the case in the experimental setups, the initial state and the target state must have non-vanishing Franck-Condon factors with the same group of vibrational states in the electronically excited states. If this is fulfilled the "simple" single cycle pump-dump control of photostabilization can be sufficient. This problem of the connectivity between the initial and the target state will be generally addressed for the pump–dump control in complex systems where the concept of the intermediate target [298] was introduced. The basic idea of this approach is to find an optimal excited state ensemble which insures the connectivity with both the initial and the target state and use it for the pulse optimization. Since here one starts from a highly excited vibrational state, the Franck–Condon overlap with the (ν=0) is unfavorable and does not allow the direct pulse optimization using $\nu = 0$ state as a target. Therefore, sequential stepwise optimization was carried out, in which first an optimal set of intermediate excited state vibrational levels is populated. The pulse obtained in this way is subsequently used as an initial guess for maximizing further the population of the (ν=0) level in the ground state.

The optimal pulse for the photostabilization is presented in Fig. 2.63. The insert serves to illustrate subpulse richness. The spectral analysis of the pulse (cf. Fig. 2.63b) shows two main broad features centered around 10200 cm^{-1} and 13000 cm^{-1}. The higher energy part of the pulse is responsible for the sequence of pump-dump processes involving highly excited vibrational states of all three involved electronic states. These processes populate sequentially lower and lower vibrational states, thus increasing Franck-Condon overlap with target state ν=0. The second lower energy part of the pulse at 10200 cm^{-1} is mainly responsible for subsequent optimal cooling in the $0_g^+(I)$ electronic state and leads to a cascade of transitions steering the population into the ν=0 state. However, it should be pointed out that both parts of the pulse are spectrally very broad and that their tails are also responsible for stepping down the vibrational ladder. This is due to the fact that efficient transitions can take place only between the states with large Franck-Condon factors. The latter occurs either at the inner or at the outer turning point of the ground state potential and involve both low lying (inner) and high lying (outer) vibrational states of the electronically excited states which is the main reason for the spectral broadness of the optimal pulse.

The time dependent populations of the electronic states are presented in Fig. 2.63c. They reflect the mechanism of the photostabilization process which can be followed from the snapshots of the wave packet dynamics shown in Fig. 2.64. The initial excitation populates the $0_u^+(II)$ state and creates a wave packet which is propagating toward the inner turning point (cf. Fig. 2.64). This motion of the wave packet is accompanied by mutual exchange of excited states populations but involving also the ground state, as can be seen from snapshots corresponding to 3.75 and 7.55 ps. At 9.9 ps the excited state wave packet is located in the bound region of the excited state potentials. This is achieved by successive inward propagation in the ground state and subsequent excitation to the $0_u^+(II)$ on the left side of the avoided crossing. Within the

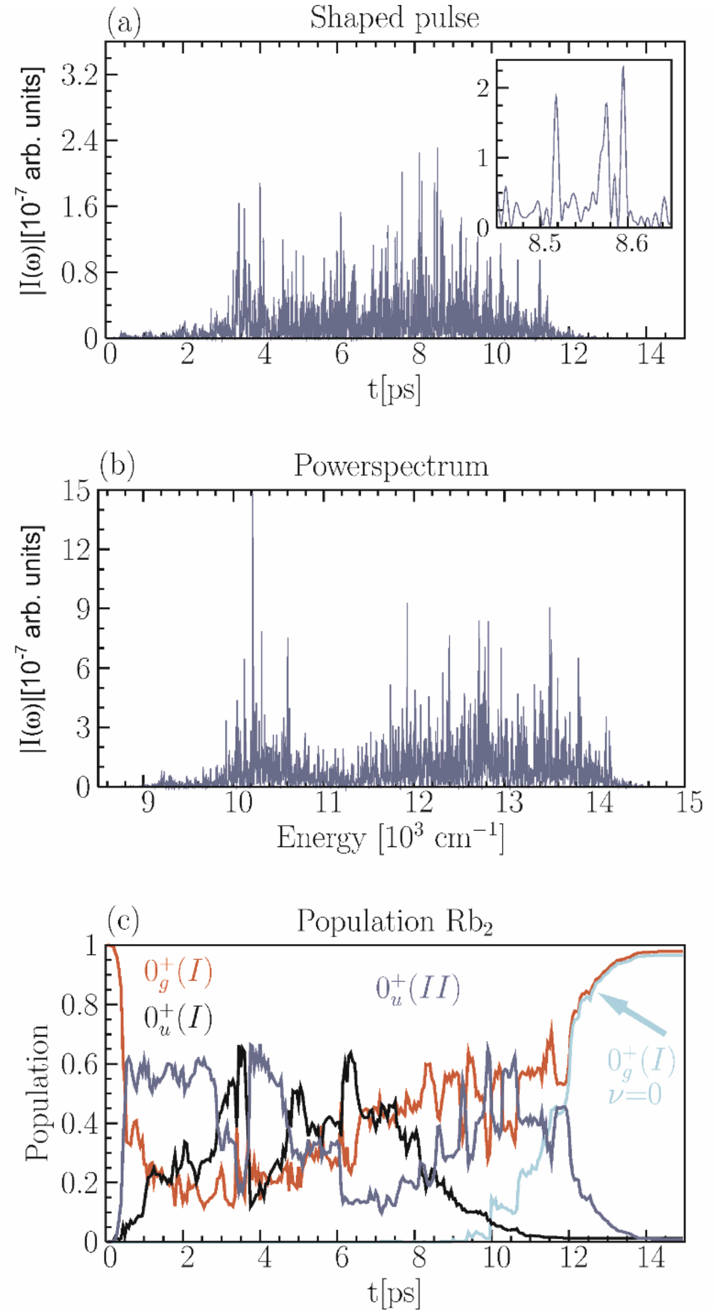

Fig. 2.63. (a) Intensity $|I(t)|$ of the optimal laser field $\epsilon(t)$ driving the photostabilization of Rb_2. The insert marked by a lens shows a details of the pulse between 8.45 and 8.65 ps. (b) Power spectrum of the optimal pulse. (c) Time-dependent populations of the electronic states. Population of the target level ν=0 is shown in turquoise color.

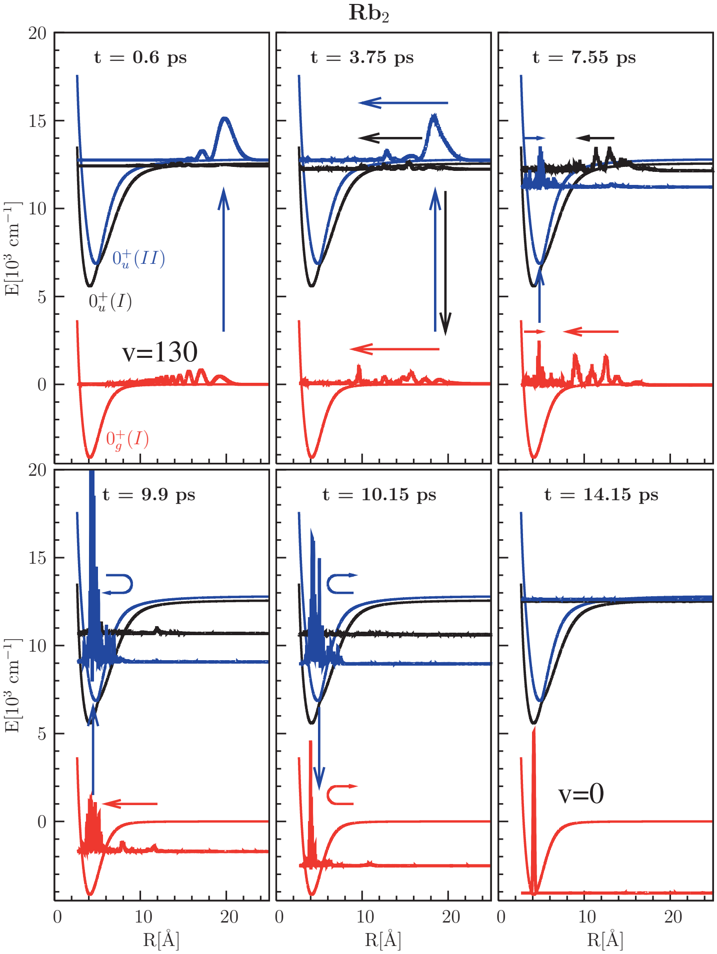

Fig. 2.64. Snapshots of the wave packet dynamics under the influence of the optimal pulse shown in Fig. 2.63, achieving 100 percent population of the vibrational ground state of Rb$_2$.

next 5 ps the stepping down the vibrational ladder is completed leading to almost 100 percent population of the $\nu = 0$ vibrational state at 14.15 ps.

The simulations show that efficient cooling and photostabilization can be achieved if the high lying but bound vibrational states are initially populated. The pulses obtained from the optimal control algorithm are spectrally very broad and present a challenge for the experimental realization due to various constraints imposed by the experimental setup. In order to investigate how the restrictions on the pulse shape influences the efficiency of the optimization, additional simulations were carried out in which (i) the total optimization time was restricted to 9 ps instead of 15 ps and (ii) the spectral range of the pulse is restricted to the experimentally accessible range from 11770 cm^{-1} to 13000 cm^{-1}. The results are shown in Fig. 2.65.

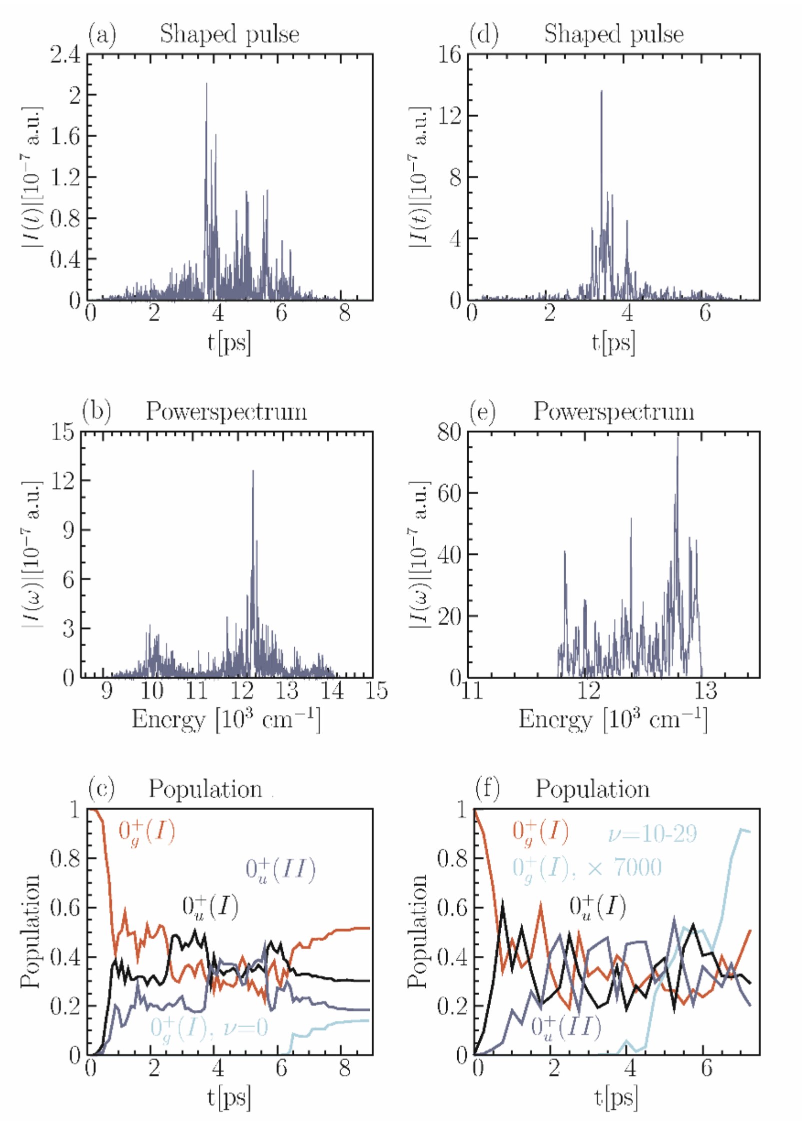

Fig. 2.65. Optimal pulse, powerspectrum and time-dependent state populations for the constrained pulse optimization: (left hand side) The pulse temporal range has been restricted to 9 ps and (right hand side) the pulse spectral range has been restricted to the range from 11770 cm^{-1} to 13000 cm^{-1}.

Restricting the time interval for the optimization leads to a pulse shape (cf. left side of Fig. 2.65) which still has two spectral components centered around 10000 cm^{-1} and 12000 cm^{-1} as in the case of 15 ps optimization (cf. Fig. 2.63). As can be seen from the time dependent state populations this leads to only 20% population of the ground state vibrational level. In contrast to the restriction of the temporal range, constraining the spectral range of the optimal pulse leads also the formation of bound ground state Rb_2 molecule but results in the maximal occupation of higher vibrational levels (ν=20-30) while the occupation of the ν=0 state becomes very low (cf. right hand side of Fig. 2.65). This means that although the stable molecule is formed under these conditions it is vibrationally relatively hot.

For the experimental realization, the two color scheme in which both pulses are shaped might provide an alternative route to the vibrational ground state.

It was demonstrated that photostabilization of ultracold Rb_2 molecule in the lowest ground state vibrational level can be achieved using tailored laser pulse obtained from the full quantum mechanical optimal control theory. This allowed to determine: (i) the mechanism leading to efficient vibrational cooling involving the ground and excited electronic states and (ii) the temporal and spectral range which are necessary in order to realize the photostabilization experimentally. Moreover, the results show that limiting the temporal and spectral range of the optimal pulse can lead to significant decrease in the yield of ultracold molecules.

In summary, it was shown that optimal control with tailored laser fields represents a promising approach for the photostabilization of ultracold molecules. The presented theoretical simulations provide a new insight into the mechanism of the cooling process itself, and may lead to the proposal of new strategies for formation of cold molecules taking into account constraints imposed by the experiment. One such possible strategy could involve a separate two–color pump–dump experiment in which first, the photoassociation is induced by a shaped pump pulse and subsequently a second shaped dump pulse is used to steer the molecule into the lowest ground state vibrational level. The second possibility involves the modeling of potential curves which allow to obtain the optimal pulse with a suitable temporal and spectral range and to find the adequate molecular system with related electronic properties on which experimental realization is more convenient.

2.6 Future perspectives

Up to now, most optimization experiments on molecular systems were performed for one polarization direction and free phase and/or amplitude modulation of the laser pulse. For future applications it is now intriguing to investigate the influence of the polarization. This new dimension will open different optimization paths and may be utilized for finding more efficient excitation paths, for molecular rearrangement into particular isomers, or change of the chirality [299] of biologically relevant units. Moreover, electric ring currents in molecules associated with magnetic fields may be induced by circularly polarized ultrashort laser pulses [300,301]. These studies may also be performed by parametrically shaped pulses in phase, amplitude, and polarization, where the subpulse features like subpulse spacings, intensities, chirps, and polarization are subject to modulation. Here, the experimenter can choose the limitations under which the algorithm has to solve the problem and receives, moreover, a solution of physically relevant parameters which aids the interpretation. The results can be compared with full quantum mechanical optimization simulations and allow moreover a fast online interaction between theoretical modeling and measurement. All these investigations will be extended to a broader spectral range, shorter pulses, and higher shaping resolution in order to have more flexibility in investigating molecular processes and to achieve control of electron dynamics. White light filaments offer an exciting perspective in this regard (see Chap. 8).

To date the formation of ultracold ground state molecules by short laser pulses has been limited by the small excitation rates for the photoassociation step. On the other hand, the stabilization step to the electronic ground state is expected to be fairly efficient [272]. The photoassociation efficiency could be improved in two different ways: (i) statically, by changing the initial probability distribution, or (ii) dynamically, by accelerating the atoms toward each other.

Once the obstacle of the low photoassociation rate is overcome, the formation of ultracold molecules in their vibronic ground state can be tackled. Experimentally, an incoherent 4-photon process was shown to produce $v = 0$ RbCs molecules [302] in a MOT. Due to stabilization via spontaneous emission, the transfer efficiency was extremely small. Employing a coherent process using short, shaped laser pulses is expected to improve the efficiency of the process. This will pave the way to many applications of ultracold molecules, in particular to reaching a stable molecular Bose-Einstein condensate (BEC).

The combination of ultracold and ultrafast holds the promise of achieving *absolute* molecular quantum state control: Ultracold matter can be prepared in a single quantum state, and shaped ultrafast laser pulses are predicted to reach close to one hundred percent efficiency for state-to-state transfer processes. This paves the way to a novel ultrafast-ultracold chemistry which is based on complete control over the reactants. There the shaped laser pulses play the role of engineering the required potential energy surfaces.

Applying pulse shaping techniques to ultracold matter offers furthermore the possibility to study the interplay of control and many-body quantum correlations as present for example in a BEC. In that case, a direct comparison between control of the many-body and the two-body quantum system could be facilitated by switching from a BEC to a Mott insulator state in an optical lattice and vice versa.

References

1. T.S. Rose, M.J. Rosker, A.H. Zewail, J. Chem. Phys. **88**, 6672 (1988)
2. T.S. Rose, M.J. Rosker, A.H. Zewail, J. Chem. Phys. **91**, 7415 (1989)
3. A.H. Zewail, Faraday Discuss. Chem. Soc. **91**, 207 (1991)
4. A. Mokhtari, P. Cong, J.L. Herek, A.H. Zewail, Nature **348**, 225 (1990)
5. M. Dantus, R.M. Bowman, M. Gruebele, A.H. Zewail, J. Chem. Phys. **91**, 7489 (1989)
6. T. Baumert, B. Buhler, M. Grosser, V. Weiss, G. Gerber, J. Phys. Chem. **95**, 8103 (1991)
7. V. Engel, H. Metiu, J. Chem. Phys. **93**, 5693 (1990)
8. S. Wolf, G. Sommerer, S. Rutz, E. Schreiber, T. Leisner, L. Wöste, R.S. Berry, Phys. Rev. Lett. **74**, 4177 (1995)
9. R.S. Berry, V. Bonačić-Koutecký, J. Gaus, T. Leisner, J. Manz, B. Reischl-Lenz, H. Ruppe, S. Rutz, E. Schreiber, Š. Vajda, R. de Vivie-Riedle, S. Wolf, L. Wöste, Adv. Chem. Phys. **101**, 101 (1997)
10. G.K. Paramonov, V.A. Savva, Phys. Lett. **97A**, 340 (1983)
11. D.J. Tannor, S.A. Rice, J. Chem. Phys. **83**, 5013 (1985)
12. A.P. Peirce, M.A. Dahleh, H. Rabitz, Phys. Rev. A **37**, 4950 (1988)
13. P. Brumer, M. Shapiro, Faraday Discuss. Chem. Soc. **82**, 177 (1986)
14. M. Shapiro, P. Brumer, J. Chem. Phys. **84**, 4103 (1986)
15. T. Joseph, J. Manz, Molec. Phys. **58**, 1149 (1986)
16. S.H. Tersigni, P. Gaspard, S.A. Rice, J. Chem. Phys. **93**, 1670 (1990)
17. R. Kosloff, S.A. Rice, P. Gaspard, S. Tersigni, D.J. Tannor, Chem. Phys. **139**, 201 (1989)
18. W. Jakubetz, J. Manz, H.J. Schreier, Chem. Phys. Lett. **165**, 100 (1990)
19. J.E. Combariza, B. Just, J. Manz, G.K. Paramonov, J. Phys. Chem. **95**, 10351 (1991)
20. H. Rabitz, S. Shi, Adv. Mol. Vibr. Collision Dyn. **1A**, 187 (1991)
21. W.S. Warren, H. Rabitz, M. Dahleh, Science **259**, 1581 (1993)
22. R.S. Judson, H. Rabitz, Phys. Rev. Lett. **68**, 1500 (1992)
23. S.A. Rice, M. Zhao, *Optical control of molecular dynamics* (John Wiley & Sons, Inc., New York, 2000)
24. M. Shapiro, P. Brumer, *Principles of the quantum control of molecular processes* (Wiley-Interscience, New York, 2003)
25. S. Rutz, R. de Vivie-Riedle, E. Schreiber, Phys. Rev. A **54**, 306 (1996)
26. G. Delacrétaz, E. Grant, R. Whetten, L. Wöste, J. Zwanziger, Phys. Rev. Lett. **56**, 1598 (1986)
27. A. Lindinger, C. Lupulescu, A. Bartelt, Š. Vajda, L. Wöste, Spectrochimica Acta Part B **58**, 1109 (2003)
28. H. Kühling, K. Kobe, S. Rutz, E. Schreiber, L. Wöste, J. Phys. Chem. **98**, 6679 (1994)
29. E. Schreiber, K. Kobe, A. Ruff, S. Rutz, G. Sommerer, L. Wöste, Chem. Phys. Lett. **37**, 175 (1995)
30. H. Ruppe, S. Rutz, E. Schreiber, L. Wöste, Chem. Phys. Lett. **257**, 356 (1996)
31. M. Hartmann, J. Pittner, V. Bonačić-Koutecký, A. Heidenreich, J. Jortner, J. Chem. Phys. **108**, 3096 (1998)
32. A. Donoso, C. Martens, J. Phys. Chem. **102**, 4291 (1998)
33. A. Donoso, Y. Zheng, C. Martens, J. Chem. Phys. **119**, 5010 (2003)

34. A. Donoso, C. Martens, Phys. Rev. Let. **87**, 223202 (2001)
35. S. Hammes-Schiffer, J. Phys. Chem. A **102**, 10443 (1998)
36. E. Wigner, Phys. Rev. **40**, 749 (1932)
37. M. Hillary, R.F. O'Connel, M.O. Scully, E.P. Wigner, Phys. Rep. **106**, 1984 (1984)
38. J.E. Moyal, Camb. Phil. Soc. **45**, 99 (1949)
39. Z. Li, J.Y. Fang, C.C. Martens, J. Chem. Phys. **104**, 6919 (1996)
40. M. Hartmann, J. Pittner, V. Bonačić-Koutecký, A. Heidenreich, J. Jortner, J. Phys. Chem. **102**, 4069 (1998)
41. M. Hartmann, J. Pittner, V. Bonačić-Koutecký, J. Chem. Phys. **114**, 2106 (2001)
42. M. Hartmann, J. Pittner, V. Bonačić-Koutecký, J. Chem. Phys. **114**, 2123 (2001)
43. S. Mukamel, *Principles of nonlinear optical spectroscopy* (Oxford University Press, Oxford, 1995)
44. V. Bonačić-Koutecký, R. Mitrić, Chem. Rev. **105**, 11 (2005)
45. J.C. Tully, J. Chem. Phys. **93**, 1061 (1990)
46. Š. Vajda, A. Bartelt, E.C. Kaposta, T. Leisner, C. Lupulescu, S. Minemoto, P. Rosendo-Francisco, L. Wöste, Chem. Phys. **267**, 231 (2001)
47. V. Bonačić-Koutecký, J. Pittner, J. Koutecký, Chem. Phys. **210**, 313 (1996)
48. V. Bonačić-Koutecký, J. Pittner, J. Koutecký, Z. Phys. D **40**, 441 (1997)
49. Š. Vajda, C. Lupulescu, A. Merli, F. Budzyn, L. Wöste, M. Hartmann, J. Pittner, V. Bonačić-Koutecký, Phys. Rev. Lett. **89**, 213404 (2002)
50. M.C. Heitz, G. Durand, F. Spiegelman, C. Meier, J. Chem. Phys. **118**, 1282 (2003)
51. A. Stolow, A.E. Bragg, D.M. Neumark, Chem. Rev. **104**, 1719 (2004)
52. A. Weaver, R.B. Metz, S.E. Bradforth, D.M. Neumark, J. Chem. Phys. **93**, 5352 (1990)
53. R.B. Metz, D.M. Neumark, J. Chem. Phys. **97**, 962 (1992)
54. D.M. Neumark, Acc. Chem. Res. **26**, 33 (1993)
55. B.J. Greenblatt, M.T. Zanni, D.M. Neumark, J. Chem. Phys. **111**, 10566 (1999)
56. M.T. Zanni, B.J. Greenblatt, A.V. Davis, D.M. Neumark, J. Chem. Phys. **111**, 2991 (1999)
57. D.M. Neumark, Annu. Rev. Phys. Chem. **52**, 255 (2001)
58. B.J. Greenblatt, M.T. Zanni, D.M. Neumark, J. Chem. Phys. **112**, 601 (2000)
59. R. Wester, A.V. Davis, A.E. Bragg, D.M. Neumark, Phys. Rev. A **65**, 051201 (2002)
60. C. Frischkorn, A.E. Bragg, A.V. Davis, R. Wester, D.M. Neumark, J. Chem. Phys. **115**, 11185 (2001)
61. S.M. Burnett, A.E. Stevens, C.S. Feigerle, W.C. Lineberger, Chem. Phys. Lett. **100**, 124 (1983)
62. K.M. Ervin, J. Ho, W.C. Lineberger, J. Chem. Phys. **91**, 5974 (1989)
63. P.G. Wenthold, D. Hrovat, W.T. Borden, W.C. Lineberger, Science **272**, 1456 (1996)
64. D.W. Boo, Y. Ozaki, L.H. Andersen, W.C. Lineberger, J. Phys. Chem. A **101**, 6688 (1997)
65. I. Andrianov, V. Bonačić-Koutecký, M. Hartmann, J. Manz, J. Pittner, K. Sundermann, Chem. Phys. Lett. **318**, 256 (2000)

66. M. Hartmann, R. Mitrić, B. Stanca, V. Bonačić-Koutecký, Eur. Phys. J. D **16**, 151 (2001)
67. R. Mitrić, M. Hartmann, B. Stanca, V. Bonačić-Koutecký, P. Fantucci, J. Phys. Chem. A **105**, 8892 (2001)
68. T.M. Bernhardt, J. Hagen, L.D. Socaciu, J. Le Roux, D. Popolan, M. Vaida, L. Wöste, R. Mitrić, V. Bonačić-Koutecký, A. Heidenreich, J. Jortner, ChemPhysChem **6**, 243 (2005)
69. V. Bonačić-Koutecký, P. Fantucci, J. Koutecký, Chem. Rev. **91**, 1035 (1991)
70. D.J. Wales, *Energy landscapes* (Cambridge University Press, Cambridge, 2003)
71. C. Leforestier, J. Chem. Phys. **68**, 4406 (1978)
72. R.N. Barnett, U. Landman, Phys. Rev. B **48**, 2081 (1993)
73. O. Rubner, C. Meier, V. Engel, J. Chem. Phys. **107**, 1066 (1997)
74. V. Bonačić-Koutecký, L. Češpiva, P. Fantucci, J. Koutecký, J. Chem. Phys. **98**, 7981 (1993)
75. V. Bonačić-Koutecký, L. Češpiva, P. Fantucci, J. Koutecký, J. Chem. Phys. **100**, 490 (1994)
76. V. Bonačić-Koutecký, J. Pittner, M. Boiron, P. Fantucci, J. Chem. Phys. **110**, 3876 (1999)
77. V. Bonačić-Koutecký, V. Veyret, R. Mitrić, J. Chem. Phys. **115**, 10450 (2001)
78. H. Hakkinen, M. Moseler, U. Landman, Phys. Rev. Lett. **89**, 033401 (2002)
79. V. Bonačić-Koutecký, J. Burda, M. Ge, R. Mitrić, G. Zampella, R. Fantucci, J. Chem. Phys. **117**, 3120 (2002)
80. R. Mitrić, M. Hartmann, J. Pittner, V. Bonačić-Koutecký, Eur. Phys. J. **24**, 45 (2003)
81. W.T. Wallace, R.B. Wyrwas, R.L. Whetten, R. Mitrić, V. Bonačić-Koutecký, J. Am. Chem. Soc. **125**, 8408 (2003)
82. M.L. Kimble, A.W.J. Castleman, R. Mitrić, C. Bürgel, V. Bonačić-Koutecký, J. Am. Chem. Soc. **126**, 2526 (2004)
83. J. Hagen, L.D. Socaciu, J. Le Roux, D. Popolan, T.M. Bernhardt, L. Wöste, R. Mitrić, V. Bonačić-Koutecký, J. Am. Chem. Soc. **126**, 3442 (2004)
84. C. Sieber, J. Buttet, W. Harbich, C. Félix, R. Mitrić, V. Bonačić-Koutecký, Phys. Rev. A **70** (2004)
85. P. Ballone, W. Andreoni, *Metal clusters* (Wiley Inc., Chichester, 1999), p. 71
86. F. Furche, R. Ahlrichs, P. Weis, C. Jacob, S. Gilb, T. Bierweiler, M.M. Kappes, J. Chem. Phys **117**, 6982 (2002)
87. P. Weis, T. Bierweiler, S. Gilb, M.M. Kappes, Chem. Phys. Lett. **355**, 355 (2002)
88. L. König, I. Rabin, W. Schulze, G. Ertl, Science **274**, 1353 (1996)
89. C. Felix, C. Sieber, W. Harbich, J. Buttet, I. Rabin, W. Schulze, G. Ertl, Chem. Phys. Lett. **313**, 105 (1998)
90. I. Rabin, W. Schulze, G. Ertl, C. Felix, C. Sieber, W. Harbich, J. Buttet, Chem. Phys. Lett. **320**, 59 (2000)
91. C. Felix, S. Sieber, W. Harbich, J. Buttet, I. Rabin, W. Schulze, G. Ertl, Phys. Rev. Lett. **86**, 2992 (2001)
92. W. Harbich, C. Felix, C. R. Physique **3**, 289 (2002)
93. M. Haruta, Catal. Today **36**, 153 (1997)
94. T.H. Lee, K.M. Ervin, J. Phys. Chem. **98**, 10023 (1994)
95. B.E. Salisbury, W.T. Wallace, R.L. Whetten, Chem. Phys. **262**, 131 (2000)
96. K.J. Taylor, C.L. Pettiette-Hall, O. Cheshnovsky, R.E. Smalley, J. Chem. Phys. **96**, 3319 (1992)

97. J. Ho, K.M. Ervin, W.C. Lineberger, J. Chem. Phys. **93**, 6987 (1990)
98. H. Handschuh, G. Ganteför, P.S. Bechtold, W. Eberhardt, J. Chem. Phys. **100**, 7093 (1994)
99. G. Lüttgens, N. Pontius, P.S. Bechtold, M. Neeb, W. Eberhardt, Phys. Rev. Lett. **88**, 076102 (2002)
100. Y. Negishi, Y. Nakajima, K. Kaya, J. Chem. Phys. **115**, 3657 (2001)
101. A. Sanchez, S. Abbet, U. Heiz, W.D. Schneider, H. Hakkinen, R.N. Barnett, U. Landman, J. Phys. Chem. A **103**, 9573 (1999)
102. L.D. Socaciu, J. Hagen, T.M. Bernhardt, L. Wöste, U. Heiz, H. Hakkinen, U. Landman, J. Am. Chem. Soc. **125**, 10437 (2003)
103. S.A. Varganov, R.M. Olson, M.S. Gordon, H. Metiu, J. Chem. Phys. **119**, 2531 (2003)
104. G. Mills, M.S. Gordon, H. Metiu, J. Chem. Phys. **118**, 4198 (2003)
105. A.D. Becke, Phys. Rev. A **98**, 3098 (1988)
106. C. Lee, W. Yang, R.G. Parr, Phys. Rev. B **37**, 785 (1985)
107. T. Leisner, Š. Vajda, S. Wolf, L. Wöste, R.S. Berry, J. Chem. Phys. **111**, 1017 (1999)
108. H. Hess, K.R. Asmis, T. Leisner, L. Wöste, Eur. Phys. J. D **16**, 145 (2001)
109. R. Keller, F. Nöhmeier, P. Spädtke, H. Schönenberg, Vacuum **34**, 31 (1984)
110. T.M. Bernhardt, Int. J. Mass. Spectrom. **243**, 1 (2005)
111. L. Lian, P.A. Hackett, D.M. Rayner, J. Chem. Phys. **99**, 2583 (1993)
112. L.D. Socaciu, J. Hagen, U. Heiz, T.M. Bernhardt, T. Leisner, L. Wöste, Chem. Phys. Lett. **340**, 282 (2001)
113. M. Schmidt, P. Cahuzac, C. Brechignac, H.P. Cheng, J. Chem. Phys. **118** (2003)
114. M. Schmidt, A. Masson, C. Brechignac, Phys. Rev. Lett. **91**, 243401 (2003)
115. L.D. Socaciu, J. Hagen, J. Le Roux, D. Popolan, T.M. Bernhardt, L. Wöste, Š. Vajda, Chem. Phys. **120**, 2078 (2004)
116. Y.D. Kim, G. Ganteför, Chem. Phys. Lett. **383**, 80 (2004)
117. L.D. Socaciu-Siebert, J. Hagen, J. Le Roux, D. Popolan, Š. Vajda, T.M. Bernhardt, L. Wöste, Phys. Chem. Chem. Phys. **7**, 2706 (2005)
118. D.J. Tannor, S.A. Rice, Adv. Chem. Phys. **70**, 441 (1988)
119. M. Shapiro, P. Brumer, Int. Rev. Phys. Chem. **13**, 187 (1994)
120. T. Joseph, J. Manz, Mol. Phys. **58**, 1149 (1986)
121. W. Jakubetz, B. Just, J. Manz, H.J. Schreier, J. Phys. Chem. **94**, 2294 (1990)
122. J. Somlói, V.A. Kazakov, D.J. Tannor, Chem. Phys. **172**, 85 (1993)
123. B. Amstrup, J.D. Doll, R.A. Sauerbrey, Szabó, A. Lörincz, Phys. Rev. A **48**, 3830 (1993)
124. R.G. Gordon, S.A. Rice, Annu. Rev. Phys. Chem. **48**, 601 (1997)
125. L.C. Zhu, V. Kleiman, X.N. Li, S.P. Lu, K. Trentelman, R.J. Gordon, Science **270**, 77 (1995)
126. C. Chen, D.S. Elliott, Phys. Rev. Lett. **65**, 1737 (1990)
127. S.M. Park, R.J. Lu, R.J. Gordon, J. Chem. Phys. **94**, 8622 (1991)
128. G.Q. Xing, X.B. Wang, X. Huang, R. Bersohn, J. Chem. Phys. **104**, 826 (1996)
129. A. Shnitman, I. Sofer, I. Golub, A. Yogev, M. Shapiro, Z. Chen, P. Brumer, Phys. Rev. Lett. **76**, 2886 (1996)
130. T. Baumert, B. Buhler, M. Grosser, R. Thalweiser, V. Weiss, E. Wiedenmann, G. Gerber, J. Phys. Chem. **95**, 8103 (1991)
131. T. Baumert, G. Gerber, Isr. J. Chem. **34**, 103 (1994)

132. E.D. Potter, J.L. Herek, S. Pedersen, Q. Liu, A.H. Zewail, Nature **355**, 66 (1992)
133. J.L. Herek, A. Materny, A.H. Zewail, Chem. Phys. Lett. **228**, 15 (1994)
134. A. Assion, T. Baumert, V. Seyfried, V. Weiss, E. Wiedenmann, G. Gerber, Z. Phys. D **36**, 265 (1996)
135. T. Baumert, J. Helbing, G. Gerber, Adv. Chem. Phys. **101**, 47 (1997)
136. D.J. Tannor, S.A. Rice, J. Chem. Phys. **85**, 5805 (1986)
137. S. Shi, H. Rabitz, Chem. Phys. **139**, 185 (1989)
138. R. Kosloff, A.D. Hammerich, D.J. Tannor, Phys. Rev. Lett. **69**, 2172 (1992)
139. A. Bartana, R. Kosloff, D.J. Tannor, J. Chem. Phys. **99**, 196 (1993)
140. V. Malinovsky, C. Meier, D.J. Tannor, Chem. Phys. **221**, 67 (1997)
141. V. Malinovsky, D.J. Tannor, Phys. Rev. A **56**, 4929 (1997)
142. J. Vala, R. Kosloff, Opt. Express **8**, 238 (2001)
143. P. Marquetand, C. Meier, V. Engel, J. Chem. Phys. **123**, 204320 (2005)
144. C. Meier, M.C. Heitz, J. Chem. Phys. **123**, 044504 (2005)
145. S. Gräfe, C. Meier, V. Engel, J. Chem. Phys. **122**, 184103 (2005)
146. S. Sklarz, D.J. Tannor, Chem. Phys. **322**, 87 (2006)
147. Y. Chen, P. Gross, V. Ramakrishna, H. Rabitz, K. Mease, J. Chem. Phys. **102**, 8001 (1995)
148. D.J. Tannor, *Molecules in laser fields* (M. Dekker Inc., 1999), p. 403
149. D.J. Tannor, R. Kosloff, A. Bartana, Faraday Discuss. **113**, 365 (1999)
150. T. Baumert, T. Brixner, V. Seyfried, M. Strehle, G. Gerber, Appl. Phys. B **65**, 779 (1997)
151. D. Yelin, D. Meshulach, Y. Silberberg, Opt. Lett. **22**, 1793 (1997)
152. A. Efimov, M.D. Moores, N.M. Beach, J.L. Krause, D.H. Reitze, Opt. Lett. **23**, 1915 (1998)
153. E. Zeek, K. Maginnis, S. Backus, U. Russek, M.M. Murnane, G. Mourou, H.C. Kapteyn, G. Vdovin, Opt. Lett. **24**, 493 (1999)
154. E. Zeek, R. Bartels, M.M. Murnane, H.C. Kapteyn, S. Backus, G. Vdovin, Opt. Lett. **25**, 587 (2000)
155. D.E. Goldberg, *Genetic algorithms in search, optimization, and machine learning* (Addison-Wesley, Reading, 1993)
156. H.P. Schwefel, *Evolution and optimum seeking* (Wiley, New York, 1995)
157. A. Assion, T. Baumert, M. Bergt, T. Brixner, B. Kiefer, V. Seyfried, M. Strehle, G. Gerber, *Springer Series in Chemical Physics, vol. 63* (Springer, Berlin, 1998), p. 471
158. A. Assion, T. Baumert, M. Bergt, T. Brixner, B. Kiefer, V. Seyfried, M. Strehle, G. Gerber, Science **282**, 919 (1998)
159. T.C. Weinacht, J.L. White, P.H. Bucksbaum, J. Phys. Chem. A **103**, 10166 (1999)
160. T. Hornung, R. Meier, M. Motzkus, Chem. Phys. Lett. **326**, 445 (2000)
161. Š. Vajda, P. Rosendo-Francisco, C. Kaposta, M. Krenz, L. Lupulescu, L. Wöste, Eur. Phys. J. D **16**, 161 (2001)
162. A. Bartelt, S. Minemoto, C. Lupulescu, Š. Vajda, L. Wöste, Eur. Phys. J. D **16**, 127 (2001)
163. Š. Vajda, C. Lupulescu, A. Bartelt, F. Budzyn, P. Rosendo-Francisco, L. Wöste, *Femtochemistry and Femtobiology* (World Scientific Publishing: Singapore, 2002), p. 472
164. A. Bartelt, A. Lindinger, C. Lupulescu, Š. Vajda, L. Wöste, Phys. Chem. Chem. Phys. **5**, 3610 (2003)

165. C. Lupulescu, A. Lindinger, M. Plewicky, A. Merli, S.M. Weber, L. Wöste, Chem. Phys. **296**, 63 (2004)
166. A. Bartelt, Steuerung der Wellenpaketdynamik in kleinen Alkaliclustern mit optimierten Femtosekundenpulsen. Ph.D. thesis, Freie Universität Berlin (2002)
167. R.J. Levis, G.M. Menkir, H. Rabitz, Science **292**, 709 (2001)
168. T. Brixner, M. Strehle, G. Gerber, Appl. Phys. B **68**, 281 (1999)
169. A. Efimov, M.D. Moores, B. Mei, J.L. Krause, C.W. Siders, D.H. Reitze, Appl. Phys. B **70**, 133 (2000)
170. D. Zeidler, T. Hornung, D. Proch, M. Motzkus, Appl. Phys. B **70**, 125 (2000)
171. D. Meshulach, Y. Silberberg, Nature **396**, 239 (1998)
172. T. Hornung, R. Meier, D. Zeidler, K.L. Kompa, D. Proch, M. Motzkus, Appl. Phys. B **71**, 277 (2000)
173. T.C. Weinacht, J. Ahn, P.H. Bucksbaum, Nature **397**, 233 (1999)
174. R. Bartels, S. Backus, E. Zeek, L. Misoguti, G. Vdovin, I.P. Christov, M.M. Murnane, H.C. Kapteyn, Nature **164** (2000)
175. J. Kunde, B. Baumann, S. Arlt, F. Morier-Genoud, U. Siegner, U. Keller, Appl. Phys. Lett. **77**, 924 (2000)
176. H. Rabitz, R. de Vivie-Riedle, M. Motzkus, K. Kompa, Science **288**, 824 (2000)
177. T. Hornung, M. Motzkus, R. de Vivie-Riedle, Phys. Rev. A **65**, 021403 (2002)
178. M. Braun, V. Engel, Z. Phys. D **39**, 301 (1997)
179. H. Schwoerer, R. Pausch, M. Heid, V. Engel, W. Kiefer, J. Chem. Phys. **107**, 9749 (1997)
180. Z.W. Shen, T. Chen, M. Heid, W. Kiefer, V. Engel, Eur. Phys. J. D **14**, 167 (2001)
181. R. de Vivie-Riedle, K. Kobe, J. Manz, W. Meyer, B. Reischl, S. Rutz, E. Schreiber, L. Wöste, J. Phys. Chem. **100**, 7789 (1996)
182. C. Nicole, M.A. Bouchene, C. Meier, S. Magnier, E. Schreiber, B. Girard, J. Chem. Phys. **111**, 7857 (1999)
183. L. Pesce, Z. Amitay, R. Uberna, S.R. Leone, M. Ratner, R. Kosloff, J. Chem. Phys. **114**, 1259 (2001)
184. K. Sundermann, R. de Vivie-Riedle, J. Chem. Phys. **110**, 1896 (1999)
185. T. Hornung, M. Motzkus, de Vivie-Riedle, J. Chem. Phys. **115**, 3105 (2001)
186. G. Grégoir, M. Mons, I. Dimicoli, C. Dedonder-Lardeux, S. Jouvet, S. Martrenchard, D. Solgadi, J. Chem. Phys. **112**, 8794 (2000)
187. Z. Shen, V. Engel, R. Xu, J. Cheng, Y. Yan, J. Chem. Phys. **117**, 6142 (2002)
188. G. Rodriguez, J.G. Eden, Chem. Phys. Lett. **205**, 371 (1993)
189. G. Rodriguez, P.C. John, J.G. Eden, J. Chem. Phys. **103**, 10473 (1995)
190. R. Pausch, M. Heid, T. Chen, W. Kiefer, H. Schwoerer, J. Chem. Phys. **110**, 9560 (1999)
191. R. Pausch, M. Heid, T. Chen, W. Kiefer, H. Schwoerer, J. Raman Spectrosc. **31**, 7 (2000)
192. R. Uberna, Z. Amitay, R.A. Loomis, S.R. Leone, Faraday Discuss. **113**, 385 (1999)
193. J.B. Ballard, H.U. Stauffer, Z. Amitay, S.R. Leone, J. Chem. Phys. **116**, 1350 (2002)
194. J.J. Sakurai, Modern Quantum Mechanics, Benjamin Cummings Publishing, Menlo Park (1985)
195. S. Chelkowski, A.D. Bandrauk, P.B. Corkum, Phys. Rev. Lett. **65**, 2355 (1990)

196. T. Witte, T. Hornung, L. Windhorn, D. Proch, R. de Vivie-Riedle, M. Motzkus, K.L. Kompa, J. Chem. Phys. **118**, 2021 (2003)
197. P.A.M. Dirac, *The Principles of quantum mechanics*, vol. 4th Edition (Oxford Science Publications, Oxford, 1958)
198. J.V. Josè, E.J. Saletan, *Classical dynamics* (Cambridge University Press, Cambridge, 1998)
199. C.D. Schwieters, H. Rabitz, Phys. Rev. A **44**, 5224 (1991)
200. C.D. Schwieters, H. Rabitz, Phys. Rev. A **48**, 2549 (1993)
201. Y. Chen, P. Gross, V. Ramakrishna, H. Rabitz, K. Mease, H. Singh, Automatica **33**, 1617 (1997)
202. J.L. Herek, A. Materny, A.H. Zewail, Chem. Phys. Lett. **228**, 15 (1994)
203. T. Taneichi, T. Kobayashi, Y. Ohtsuki, Y. Fujimura, Chem. Phys. Lett. **231**, 50 (1994)
204. C.J. Bardeen, J. Che, K.R. Wilson, V.V. Yakovlevi, P. Cong, B. Kohler, J.L. Krause, M. Messina, J. Phys. Chem. A **101**, 3815 (1997)
205. E. Charron, A. Giusti-Suzor, J. Chem. Phys. **108**, 3922 (1998)
206. M. Grønager, N.E. Henriksen, J. Chem. Phys. **109**, 4335 (1998)
207. B.H. Hosseini, H.R. Sadeghpour, N. Balakrishnan, Phys. Rev. A **71**, 023402 (2005)
208. S. Gräfe, P. Marquetand, N.E. Henriksen, K.B. Møller, V. Engel, Chem. Phys. Lett. **398**, 180 (2004)
209. P. Marquetand, V. Engel, Chem. Phys. Lett. **407**, 471 (2005)
210. G.H. Peslherbe, R. Bianco, J.T. Hynes, B.M. Ladanyi, J. Chem. Soc., Faraday Trans. **93**, 977 (1997)
211. C. Cohen-Tannoudji, B. Diu, R. Laloe, *Quantum Mechanics*, Vol. I, Wiley, New York (1977)
212. Y. Zhao, O. Kühn, J. Phys. Chem. A **104**, 4882 (2000)
213. T. Baumert, M. Grosser, R. Thalweiser, G. Gerber, Phys. Rev. Lett. **67**, 3753 (1991)
214. V. Engel, T. Baumert, C. Meier, G. Gerber, Z. Phys. D-Atoms, Molecules and Clusters **28**, 37 (1993)
215. T. Baumert, G. Gerber, Adv. At. Molec. Opt. Phys. **35**, 163 (1995)
216. S. Gräfe, M. Erdmann, V. Engel, Phys. Rev. A **72**, 013404 (2005)
217. H. Metiu, V. Engel, J. Opt. Soc. Am. **7**, 1709 (1990)
218. N.F. Scherer, R.J. Carlson, A. Matro, M. Du, A.J. Ruggiero, V. Romero-Rochin, J.A. Cina, G.R. Fleming, S.A. Rice, J. Chem. Phys. **95**, 1487 (1991)
219. V. Blanchet, C. Nicole, M. Bouchene, B. Girard, Phys. Rev. Lett. **78**, 2716 (1997)
220. C.W. Hillegas, J.X. Tull, D. Goswami, D. Strickland, W.S. Warren, Opt. Lett. **19**, 737 (1994)
221. A.M. Weiner, D.E. Leaird, J.S. Patel, J.R. Wullert, IEEE J. Quant. Elect. **28**, 908 (1992)
222. O.E. Martinez, IEEE J. Quant. Elect. **23**, 59 (1987)
223. M. Wefers, K.J. Nelson, J. Opt. Soc. Am B **12**, 1343 (1995)
224. T. Brixner, G. Gerber, ChemPhysChem **4**, 418 (2003)
225. J. Heufelder, H. Ruppe, S. Rutz, E. Schreiber, L. Wöste, Chem. Phys. Lett. **269**, 1 (1997)
226. A. Bartelt, A. Lindinger, Š. Vajda, C. Lupulescu, L. Wöste, Phys. Chem. Chem. Phys. **6**, 1679 (2004)

227. S. Magnier, M. Aubert-Frécon, P.J. Millié, J. Mol. Spetrosc. **200**, 96 (2000)
228. H. Tal Ezer, R. Kosloff, J. Chem. Phys. **81**, 3967 (1984)
229. M. Demiralp, H. Rabitz, Phys. Rev. A **57**, 2420 (1998)
230. V.F. Krotov, Control and Cybernetics **17**, 115 (1988)
231. B. Schäfer-Bung, R. Mitrić, V. Bonačić-Koutecký, A. Bartelt, C. Lupulescu, A. Lindinger, Š. Vajda, S.M. Weber, L. Wöste, J. Phys. Chem. A **108**, 4175 (2004)
232. P.T. Greenland, Contemp. Phys. **30**, 405 (1990)
233. W.H. King, *Isotope shifts in atomic spectra* (Plenum, New York, 1984)
234. J. Heufelder, H. Ruppe, S. Rutz, E. Schreiber, L. Wöste, Chem. Phys. Lett. **269**, 1 (1997)
235. I.S. Averbukh, M.J.J. Vrakking, D.M. Villeneuve, A. Stolow, Phys. Rev. Lett. **77**, 3518 (1996)
236. S. Rutz, E. Schreiber, Eur. Phys. J. D **4**, 151 (1998)
237. G. Jong, L. Li, T. J. Whang, W. C. Stwalley, J. A Coxon, M. Li, A. M. Lyyra, J. Mol. Spect. **155**, 115 (1992)
238. R. de Vivie-Riedle, B. Reischl, S. Rutz, E. Schreiber, J. Phys. Chem. **99**, 16829 (1995)
239. A.J. Ross, P. Crozet, C. Effantin, J. d'Incan, R.F. Barrow, J. Phys. B **20**, 6225 (1987)
240. A. Lindinger, C. Lupulescu, M. Plewicki, F. Vetter, A. Merli, S.M. Weber, L. Wöste, Phys. Rev. Lett. **93**, 033001 (2004)
241. M. Leibscher, I.S. Averbukh, Phys. Rev. A **2001**, 043407 (2001)
242. A. Lindinger, C. Lupulescu, F. Vetter, M. Plewicki, S.M. Weber, A. Merli, L. Wöste, J Chem. Phys. **122**, 024312 (2005)
243. A. Lindinger, C. Lupulescu, M. Plewicki, F. Vetter, A. Merli, S.M. Weber, L. Wöste, Phys. Rev. Lett. **93**, 033001 (2004)
244. B. Schäfer-Bung, V. Bonačić-Koutecký, F. Sauer, S.M. Weber, L. Wöste, A. Lindinger, J. Chem. Phys., in press (2006)
245. J.W. Nicolson, J. Jaspara, W. Rudolph, Opt. Lett. **24**, 1774 (1999)
246. F. Vetter, M. Plewicki, A. Lindinger, A. Merli, S.M. Weber, L. Wöste, Phys. Chem. Chem. Phys. **7**, 1151 (2005)
247. J.M. Geremia, W. Zhu, H. Rabitz, J. Chem. Phys. **113**, 10841 (2000)
248. T. Hornung, R. Meier, M. Motzkus, Chem. Phys. Lett. **326**, 445 (2000)
249. S.M. Weber, A. Lindinger, F. Vetter, M. Plewicki, A. Merli, L. Wöste, Eur. Phys. J. D **33**, 39 (2005)
250. A. Lindinger, S.M. Weber, C. Lupulescu, F. Vetter, M. Plewicki, A. Merli, L. Wöste, A.F. Bartelt, H. Rabitz, Phys. Rev. A **71**, 013419 (2005)
251. A.M. Weiner, Prog. Quant. Electr. **19**, 161 (1995)
252. M. Hacker, G. Stobrawa, T. Feurer, Opt. Expr. **9**, 191 (2001)
253. R. Gerchberg, W. Saxon, Optik **35**, 237 (1971)
254. T. Brixner, G. Gerber, Optics Letters **26**, 557 (2001)
255. T. Brixner, G. Krampert, T. Pfeifer, R. Selle, G.G.M. Wollenhaupt, O. Graefe, C. Horn, D. Liese, T. Baumert, Phys. Rev. Lett. **92**, 208301 (2004)
256. T. Suzuki, S. Minemoto, T. Kanai, H. Sakai, Phys. Rev. Lett. **92**, 13 (2004)
257. L. Polachek, D. Oron, Y. Silberberg, Optics Letters **31**, 631 (2006)
258. M. Plewicki, F. Weise, S.M. Weber, A. Lindinger, Appl. Opt., Appl. Opt. **45**, 8354 (2006)
259. M. Plewicki, S.M. Weber, F. Weise, A. Lindinger, Appl. Phys. B, in press (2006)

260. F. Vetter, M. Plewicki, A. Lindinger, A. Merli, S.M. Weber, L. Wöste, Phys. Chem. Chem. Phys. **7**, 1151 (2005)
261. L.E. Berg, M. Beutter, T. Hansson, Chem. Phys. Chem **253**, 327 (1996)
262. J. Doyle, B. Friedrich, R.V. Krems, F. Masnou-Seeuws, Eur. Phys. J D **31**, 149 (2004)
263. G. Meijer, ChemPhysChem **3**, 495 (2002)
264. A. Fioretti, D. Comparat, A. Crubellier, O. Dulieu, F. Masnou-Seeuws, P. Pillet, Phys. Rev. Lett. **80**, 4402 (1998)
265. E.A. Donley, N.R. Claussen, S.T. Thompson, C.E. Wieman, Nature **417**, 529 (2002)
266. J. Weiner, V.S. Bagnato, S. Zilio, P.S. Julienne, Rev. Mod. Phys. **71**, 1 (1998)
267. F. Masnou-Seeuws, P. Pillet, Adv. in At., Mol. and Opt. Phys. **47**, 53 (2001)
268. O. Dulieu, F. Masnou-Seeuws, J. Opt. Soc. Am. B **20**, 1083 (2003)
269. C. Gabbanini, A. Fioretti, A. Lucchesini, S. Gozzini, M. Mazzoni, Phys. Rev. Lett. **84**, 2814 (2000)
270. A.J. Kerman, J.M. Sage, S. Sainis, T. Bergeman, D. DeMille, Phys. Rev. Lett. **92**, 153001 (2004)
271. C.P. Koch, E. Luc-Koenig, F. Masnou-Seeuws, Phys. Rev. A **73**, 033408 (2006)
272. C.P. Koch, R. Kosloff, F. Masnou-Seeuws, Phys. Rev. A **73**, 043409 (2006)
273. C.P. Koch, J.P. Palao, R. Kosloff, F. Masnou-Seeuws, Phys. Rev. A **70**, 013402 (2004)
274. W. Salzmann, U. Poschinger, R. Wester, M. Weidemüller, A. Merli, S.M. Weber, F. Sauer, M. Plewicki, F. Weise, A.M. Esparza, L. Wöste, A. Lindinger, Phys. Rev. A **73**, 023414 (2006)
275. B.L. Brown, A.J. Dicks, I.A. Walmsley, Phys. Rev. Lett. **96**, 173002 (2006)
276. C. Gabbanini, A. Fioretti, A. Luchesini, S. Gozzini, M. Mazzoni, Phys. Rev. Lett. **84**, 2814 (2000)
277. M. Kemmann, I. Mistric, S. Nussmann, H. Helm, Phys. Rev. A **69**, 022715 (2004)
278. T. Ban, D. Aumiler, G. Pichler, Phys. Rev. A **71**, 022711 (2005)
279. C.G. Townsend, N.H. Edwards, C.J. Cooper, K.P. Zetie, C.J. Foot, Phys. Rev. A **52**, 1423 (1995)
280. A. Bartelt, S. Minemoto, C. Lupulescu, Š. Vajda, L. Wöste, Eur. Phys. J. D **16**, 127 (2001)
281. M. Machholm, A. Giusti-Suzor, F.H. Mies, Phys. Rev. A **50**, 5025 (1994)
282. M.V. Korolkov, J. Manz, G.K. Paramonov, B. Schmidt, Chem. Phys. Lett. **260**, 604 (1996)
283. M.V. Korolkov, J. Manz, G.K. Paramonov, Chem. Phys. **217**, 341 (1997)
284. P. Backhaus, J. Manz, B. Schmidt, Phys. Chem. A **102**, 4118 (1998)
285. J. Vala, O. Dulieu, F. Masnou-Seeuws, P. Pillet, R. Kosloff, Phys. Rev. A **63**, 013412 (2000)
286. E. Luc-Koenig, R. Kosloff, F. Masnou-Seeuws, M. Vatasescu, Phys. Rev. A **70**, 033414 (2004)
287. E. Luc-Koenig, F. Masnou-Seeuws, M. Vatasescu, Eur. Phys. J D **31**, 239 (2004)
288. C.M. Dion, C. Drag, O. Dulieu, B. Laburthe Tolra, F. Masnou-Seeuws, P. Pillet, Phys. Rev. Lett. **86**, 2253 (2001)
289. A. Bartana, R. Kosloff, D.J. Tannor, J. Chem. Phys. **99**, 196 (1993)
290. A. Bartana, R. Kosloff, D.J. Tannor, J. Chem. Phys. **106**, 1435 (1997)

291. A. Bartana, R. Kosloff, D.J. Tannor, Chem. Phys. **267**, 195 (2001)
292. J. Werschnik, E. Gross, Journal of Optics B **7**, S300 (2005)
293. S.J. Park, Y.J. Choi, Y.S. Lee, G. Jeung, Chem. Phys. **257**, 135 (2000)
294. S.J. Park, S.W. Suh, Y.S. Lee, G. Jeung, J. Mol. Spec. **207**, 129 (2001)
295. D. Edvardsson, S. Lunell, C.M. Marian, Mol. Phys. **101**, 2381 (2003)
296. L.A. LaJohn, P.A. Christiansen, R.B. Ross, T. Atashroo, W.C. Ermler, J. Chem. Phys. **87**, 2812 (1987)
297. R. Kosloff, Ann. Rev. Phys. Chem. **45**, 145 (1994)
298. R. Mitrić, M. Hartmann, J. Pittner, V. Bonačić-Koutecký, J. Phys. Chem. A **106**, 10477 (2002)
299. K. Hoki, D. Kröner, J. Manz, Chem. Phys. **267**, 59 (2001)
300. I. Barth, J. Manz, Angew. Chem. Intern. Ed. **45**, 2962 (2006)
301. A.B. Alekseyev, M.V. Korolkov, O. Kühn, J. Manz, M. Schröder, J. Photochem. & Photobiol. A **180**, 262 (2006)
302. J.M. Sage, S. Sainis, T. Bergeman, D. DeMille, Phys. Rev. Lett. **94**, 203001 (2005)